Mechanical microcontacts of powder particles studied with the quartz crystal microbalance

Dissertation

zur Erlangung des Grades

„Doktor der Naturwissenschaften“

Am Fachbereich Chemie, Pharmazie und Geowissenschaften

der Johannes Gutenberg-Universität Mainz

Ewa Maria Vittorias

geboren in Poznan, Polen

Mainz, November 2010

Dekan:

Erstgutachter:

Zweitgutachter:

Tag der mündlichen Prüfung: 26. Januar 2011

Die vorliegende Arbeit wurde am Institut für Physikalische Chemie der Johannes-Gutenberg Universität Mainz
und am Max-Planck-Institut für Polymerforschung in Mainz unter der Betreuung von

in der Zeit von Mai 2006 bis Juli 2009 angefertigt.

Things are in motion part of the time and again they are at rest;
They are in motion when Love tends to make one out of many,
Or Strife tends to make many out of one,
And in the intervening time they are at rest.

Empedokles

Abstract

Within this work, a particle-polymer surface system is studied with respect to the particle-surface interactions. The latter are governed by micromechanics and are an important aspect for a wide range of industrial applications. Here, a new methodology is developed for understanding the adhesion process and measure the relevant forces, based on the quartz crystal microbalance, QCM.

The potential of the QCM technique for studying particle-surface interactions and reflect the adhesion process is evaluated by carrying out experiments with a custom-made setup, consisting of the QCM with a 160 nm thick film of polystyrene (PS) spin-coated onto the quartz and of glass particles, of different diameters (5-20μm), deposited onto the polymer surface. Shifts in the QCM resonance frequency are monitored as a function of the oscillation amplitude. The induced frequency shifts of the 3^{rd} overtone are found to decrease or increase, depending on the particle-surface coupling type and the applied oscillation (frequency and amplitude). For strong coupling the 3^{rd} harmonic decreased, corresponding to an "added mass" on the quartz surface. However, positive frequency shifts are observed in some cases and are attributed to weak-coupling between particle and surface. Higher overtones, i.e. the 5^{th} and 7^{th}, were utilized in order to derive additional information about the interactions taking place. For small particles, the shift for specific overtones can increase after annealing, while for large particle diameters annealing causes a negative frequency shift. The lower overtones correspond to a generally strong-coupling regime with mainly negative frequency shifts observed, while the 7^{th} appears to be sensitive to the contact break-down and the recorded shifts are positive.

During oscillation, the motion of the particles and the induced frequency shift of the QCM are governed by a balance between inertial forces and contact forces. The adherence of the particles can be increased by annealing the PS film at 150°C, which led to the formation of a PS meniscus. For the interpretation, the Hertz, Johnson-Kendall-Roberts, Derjaguin-Müller-Toporov and the Mindlin theory of partial slip are considered. The Mindlin approach is utilized to describe partial slip. When partial slip takes place induced by an oscillating load, a part of the contact ruptures. This results in a decrease of the effective contact stiffness. Additionally, there are long-term memory effects due to the consolidation which along with the QCM vibrations induce a coupling increase. However, the latter can also break the contact, lead to detachment and even surface damage and deformation due to inertia. For strong coupling the particles appear to move with the vibrations and simply act as added

effective mass leading to a decrease of the resonance frequency, in agreement with the Sauerbrey equation that is commonly used to calculate the added mass on a QCM). When the system enters the weak-coupling regime the particles are not able to follow the fast movement of the QCM surface. Hence, they effectively act as adding a “spring” with an additional coupling constant and increase the resonance frequency. The frequency shift, however, is not a unique function of the coupling constant. Furthermore, the critical oscillation amplitude is determined, above which particle detach. No movement is detected at much lower amplitudes, while for intermediate values, lateral particle displacement is observed.

In order to validate the QCM results and study the particle effects on the surface, atomic force microscopy, AFM, is additionally utilized, to image surfaces and measure surface forces. By studying the surface of the polymer film after excitation and particle removal, AFM imaging helped in detecting three different meniscus types for the contact area: the “full contact”, the “asymmetrical” and a third one including a “homocentric smaller meniscus”. The different meniscus forms result in varying bond intensity between particles and polymer film, which could explain the deviation between number of particles per surface area measured by imaging and the values provided by the QCM - frequency shift analysis. The asymmetric and the homocentric contact types are suggested to be responsible for the positive frequency shifts observed for all three measured overtones, i.e. for the weak-coupling regime, while the “full contact” type resulted in a negative frequency shift, by effectively contributing to the mass increase of the quartz..

The interplay between inertia and contact forces for the particle-surface system leads to strong- or weak-coupling, with the particle affecting in three mentioned ways the polymer surface. This is manifested in the frequency shifts of the QCM system harmonics which are used to differentiate between the two interaction types and reflect the overall state of adhesion for particles of different size.

Contents

1. Introduction

The ancient Greek found that they needed only two fundamental forces to account for all natural phenomena. One was Love, the other was Hate. The first brought things together while the second caused them to part. The idea was first proposed by Empedocles around 450 B.C. and after it was "improved" by Aristotle, it formed the basis of chemical theory for nearly 2000 years [1].

The fundamental forces of nature are nowadays accepted to be separated in 4 types. Two of these are strong and weak interactions that act between neutrons, protons, electrons and other elementary particles. These two forces have a very short range of action, typically less than 10^{-5} nm, and are relevant for the fields of nuclear and high-energy physics. The other two fundamental forces arise from the electromagnetic and gravitational interactions. These act between atoms and molecules, as well as between elementary particles. The gravitational and electromagnetic forces, such as the Coulomb interactions, are effective over a much larger range of distances, from subatomic to practically infinite distances, e.g. gravitational attraction between planetary objects. The above types are consequently the forces that govern the behaviour of everyday things. Thus, their accurate detection, measurement, modelling and possibly control is a main goal of modern physics (as well as classical physics in the past centuries). One manifestation of attractive forces is in the adhesion between two materials. Adhesion can be understood as an attraction between two solid bodies with a common contact surface that has been produced by the existence of intermolecular attractive forces that are active at short distances [2].

Adhesion between powders and surfaces plays an important role in several technological areas and processes, such as paste drying operations, fluidization of fine particles, microencapsulation, xerography and imprinting. Furthermore, it is a crucial process in the food and pharmaceutical industry with limitless and important applications. In this important technological field control of adhesion can enhance operation efficiency and reduce the production cost in the industrial processes [3].

Due to the above mentioned importance the adhesion force holds in several processes, it has become necessary to carry out more detailed studies aiming at determining the magnitude of adhesion forces between a plane surface and particles. This study and understanding is extended to different formats, sizes and chemical structure of particles and surfaces. For this research field, a methodology was already developed as early as the 17th century. This early

interest on these phenomena demonstrates their importance and explains their later industrial relevance. The first experimental technique was based on the centrifugal technique described initially by Polke [4,5] and later by Booth and Newton [6] and Lam and Newton [7-9], which was used to investigate particle size influence on the particle-surface adhesion force.

Within this work the surface – particle interactions are studied with a different approach. More specifically the interactions are described and quantified using micromechanical theories. Micromechanical contacts are important from the fundamental point of view and in many applications. As mentioned above, the mechanical interaction between fine particles determines the flow of granular materials. It is relevant for the cleaning of surfaces, for example in the semiconductor industry and the dispersion of powders to aerosols, which is crucial e.g. in asthma treatment. Another application is in lubrication of microcontacts which make commercial application of microelectromechanical systems (MEMS) devices with sliding surfaces very challenging [10]. As a further example, "acousto-lubrication" is being investigated as a potential mechanism to promote dry lubrication of MEMS devices by manipulating the micromechanical contacts [11-13].

In a general manner, understanding of friction and adhesion between solid bodies has to be based on the knowledge of the exact shape of their mechanical contact, which usually consists of microcontacts. Therefore, the quantification and modelling of microcontacts have been studied extensively [14,15]. Although the importance is easily acknowledged and despite the extensive investigation performed in the past, a fundamental understanding is lacking, due to at least two reasons.

Firstly, experiments in which the adhesion force is determined, as a microcontact property, show wide distributions rather than a single value. Adhesion forces vary by typically a factor of two to ten even within relatively monodisperse powders [16-20]. Even when measuring the adhesion force between smooth silicon oxide particles taken from one batch, adhesion forces may differ by a factor two from one pair of particles to the next [21]. As a cause of this variation surface roughness and surface heterogeneity had to be taken into account[22-27]. Roughness can change significantly in the contact area between two particles, depending on the precise location of the contact. Heterogeneity in chemical composition or molecular structure at different length scales can cause a different energy of adhesion. Thus, it can cause a variation in the effective adhesion force depending on the precise location of contact.

Second, direct measurements of adhesion forces, or rolling and sliding friction of particles are technically demanding, expensive, and of limited applicability. This includes experiments with the centrifuge technique [28] and the atomic force microscope (AFM) [29], the

two most widely used techniques. Though both techniques have provided us with valuable insights, they also have their limits. With the centrifuge contact times are in the order of hours and after detachment no further experiments can be carried out with the same particle. In the case of AFM experiments, each individual particle has to be attached to the end of a microcantilever. The contact direction is predetermined and not free to adjust. Both techniques are not applicable for routine applications and are experimentally demanding. Therefore, a simple alternative technique is desired, that can have a potential application in the industry, where fast, robust and accurate force testing is required.

A promising method for this application could be the quartz crystal microbalance, QCM. Usually the QCM is applied to measure the mass per unit area of homogeneous thin films. The measurement principle is based in the fact that the resonance frequency of the quartz decreases if the added mass is increased. However, for contacts between a QCM and particles with a size in the micron range, the frequency is found to increase [30]. The frequency increase is closely related to the stiffness of the contact and may therefore be used to probe this stiffness. Furthermore QCM testing is relatively fast, less challenging experimentally as the above mentioned methods. Finally, the method has unique applications due to the fact that one is able to probe mechanical material behaviour at high frequency excitations, as high as MHz range.

Within this work, experiments with glass particles of variable size on a QCM system are described. The aim is to evaluate the potential of QCM as a method for determining the nature and measuring the strength of microcontacts between surfaces and particles. Therefore, the influence of surface adhesion and inertia of the particles on the response of a QCM is analysed. Surface effects are found to be more important for small particles, while for the large particles inertia should dominate their movement and interaction. For this reason experiments are carried out with particles of different diameters, small and large (but all in the μm range). When the particles are attached to the QCM-film surface, the resonance frequency of the quartz crystal is changed. The latter is monitored for different excitation amplitudes. Several phenomena are observed, such as the so-called partial slip, which leads to a decrease of the resonance frequency with increasing amplitude in some (but not all) cases. The resonance frequency is correlated to particle adhesion force, vibration and generally interaction of the particles with the polymer film.

Any macroscopic movement of the particles was imaged with video microscopy which was coupled to the QCM setup in order to provide with a direct monitoring of the process

taking place during the excitation of the system. The particles were deposited onto thin films of polystyrene (PS) which had been spin-coated onto the QCM surface. After analysing the physisorbed particles, the sample was annealed at temperatures above the glass-transition temperature, T_g, of the polymer. The changes on the film surface caused by the particle movement and excitation, e.g. meniscus formation, are observed, analysed and interpreted.

The thesis is divided into seven main parts:

In the second chapter, the quartz crystal microbalance is introduced and the main properties of this tool are described. The main focus is in the application of QCM for adhesion force measurements and the suggested technique is demonstrated.

In chapter three, the theory of surface forces with the focus on adhesion force is presented. It includes also a description of the main methods that have been used for adhesion investigation. These were mainly the atomic force microscopy method, AFM, and the centrifuge technique. The non-modified, or classical, AFM set-up is described in more detail.

In the fourth chapter, the used materials, as well as the experimental set-up design are exhibited. Furthermore the sample preparation is described in detail.

Chapter five presents the results obtained by QCM in detail and interpretations are put in relations with the introduced models and with the theory.

In chapter six, the study of the surface before and after the excitation is described. The changes caused by particles during the quartz oscillation were depicted by surface imaging with AFM. Furthermore, the adhesion force is alternatively measured by colloidal probe technique and the results are presented.

In chapter seven, the main results of the thesis, using the experimental technique and setup as presented, are summarized. The work ends with the provided conclusions on the applicability of QCM for studying micromechanical contacts.

2. The Quartz Crystal Microbalance

Quartz is one of several forms of silicone dioxide (SiO_2) that is found as a crystalline form in nature. High purity natural quartz is costly to mine. Consequently, most of the quartz used for crystal fabrication today is of the 'cultured' or synthetic variety. Cultured quartz is produced by placing small seeds of quartz mixed with an alkaline solution in an autoclave. This mixture is subjected to high heat, typically above 400^0 C and high pressure, approximately 30,000 psi. This causes the quartz to dissolve and reform as thin slices. This process takes approximately 30-45 days [31,32]. Quartz crystal has a density of 2649 kg/m^3 and a melting temperature of 1750^{o}C. It is ideal for use as a frequency determining device, due to its predictable thermal, mechanical, and electrical characteristics. The quartz crystal resonator is one of the few devices that can provide a high quality factor, *Q*, i.e. a high ratio of stored to dissipated energy, that is needed for precise frequency control tools [32].

2.1 Quartz crystal resonator

The quartz crystal resonator consists of a thin plate of a piezoelectric material that can be electrically excited to oscillate in a thickness shear mode. The piezoelectric effect was found by the Curies in 1880. The word piezoelectricity literally means "pressure electricity". The prefix piezo- is derived from the Greek word πιεζό = to press. Generally speaking, a material is called piezoelectric if mechanical deformation leads to an electrical polarization (piezoeffect). The piezoelectric effect of quartz describes the appearance of electric charge on the surface of a crystal due to mechanical periodic deformation. Inversely, application of an electric voltage provokes a mechanical deformation. Thus, an alternating voltage leads to a periodic alternating deformation, i.e. an oscillation of the piezoelectric crystal [32].

The quartz crystal resonator operates due to the inverse piezoelectric effect, which is only found in crystals without any center of inversion. Crystals with an inversion center do not show piezo-electricity but are also mechanically deformable by application of an electrical field. This effect is called electro-striction and is several orders of magnitude weaker than piezoelectricity [32].

2.1.1 Vibrational modes and orientation angle

The QCM crystal surface undergoes a tangential shear motion. There are many different vibrational shear modes for crystals as shown in Fig. 2.1.

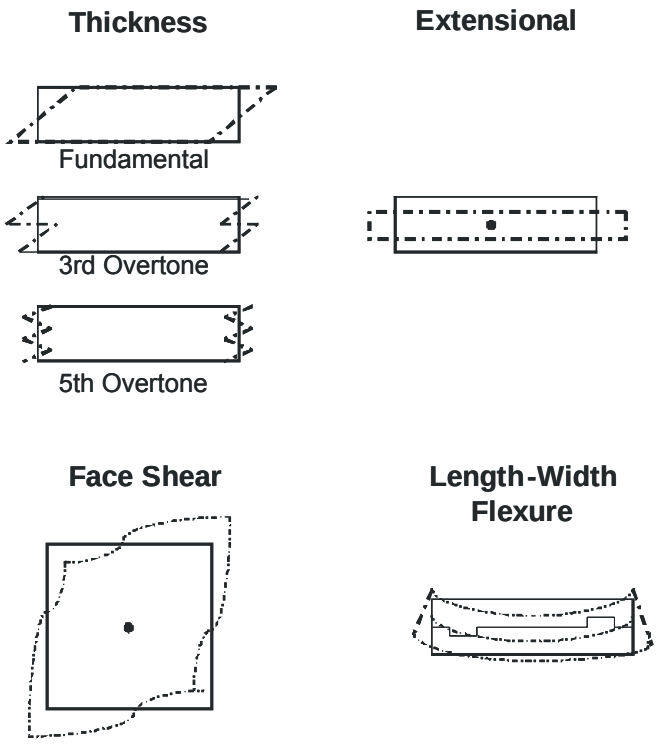

Fig. 2.1: Vibrational modes for quartz crystal.

One characteristic factor of the quartz crystal is the resonance frequency as a function of temperature. This property is primarily determined by the orientation angle at which the quartz wafers are cut from a given bar of quartz. These properties are dependent on the reference directions within the crystal. These directions are referred to as 'axes'. There are three axes in quartz, the *X*, the *Y*, and the *Z*. An ideal crystal would consist of a hexagonal prism with six facets at each end. A cross section taken from that prism would look like the depiction in Fig. 2.2. The *Z*-axis is known as the *optical axis* and the crystal repeats its physical properties every 120^0 as it is rotated about the *Z*-axis. The *X*-axis is parallel to a line bisecting the angles between adjacent prism faces. This axis is called the *electrical axis*. Electrical polarization occurs in this direction when mechanical pressure is applied. An XT-cut crystal is produced from a slab of quartz cut from that portion of the quartz bar that is perpendicular to the *X*-axis. The *Y*-axis, which is also known as the *mechanical axis*, runs at

right angles though the face of the prism and at right angles to the *X*-axis. Most *Y*-axis crystals vibrate in their 'sheer modes'; face shear for low frequency CT- and DT-cut crystal, and the thickness shear for higher frequency AT- and BT-cut crystals.

The AT-cut is the most popular of the *Y*-axis group because of its excellent frequency vs. temperature characteristics, i.e. its properties-stability under a broad temperature range (zero-temperature coefficient). The AT-cut is produced by cutting the quartz bar at an angle of approximately $35^{o}15'$ from the *Z*-axis. Ideally, an AT-cut quartz oscillates exhibiting a pure shear motion of the surface. The surface move parallel with respect to each other and the thickness of the plate does not change, i.e. there is no normal component of motion.

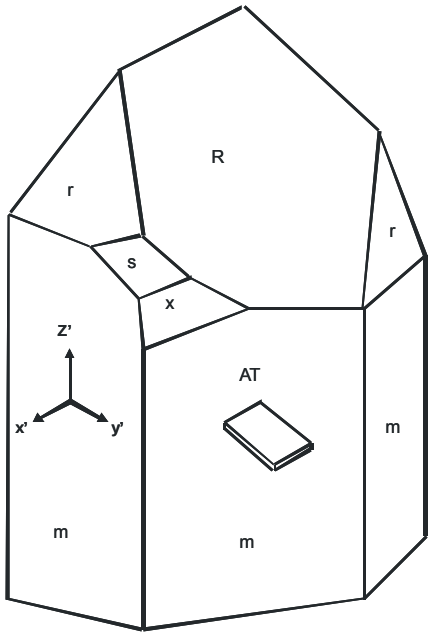

Fig. 2.2: An idealized left-handed quartz crystal showing the 35.15^{0}-inclined AT-cut plane (adapted from Bottom [32]). *R*-faces are called major, *r* the minor rhomb faces. The *s* and *x* are very rare, but when occurring enable one to distinguish between right and left quartz.

2.1.2 Effective properties of the quartz crystal resonator

The QCM crystal resonator is usually a circular disc. The thickness, h_q of the disc of the shear resonator is related to the fundamental mode frequency, f_0 by the following equation:

$$f_o = \frac{c_t}{\lambda} = \frac{\sqrt{G_q / \rho_q}}{2h_q} = \frac{N_{AT}}{h_q} \qquad \text{Eq. 1}$$

where λ is the wave length of the oscillation and c_t is the transversal velocity of sound. An explanation of the variables and respective values is given in the Table 2.1. Knowing the thickness h_q of the quartz plate the resonance frequency can easily be calculated using the frequency constant, N_{AT}. The even harmonics usually cannot be excited because the shear induced polarisation averages to zero. The excitation is however possible for the odd multiples of the excitation frequency:

$$f_n \approx n \times f_0 \qquad \text{Eq. 2}$$

where n = 1, 3, 5, …

density (ρ_q)	2649 kg/m^3
eff. shear modulus (G_q)	$2.957 \cdot 10^{10}$ N/m^3
eff. piezoelectric constant (e'_{26})	$9.65 \cdot 10^{-2}$ C/m^2
eff. dielectric constant (ε_q)	$40.3 \cdot 10^{-12}$ F/m
piezoelectric coefficient $(d'_{26} = e'_{26}/G_q)$	$3.21 \cdot 10^{-12}$ m/V
piezoelectrical coupling constant (κ^2)	0.0080
frequency constant (N_{AT})	1660 kHz mm
acoustic impedance (Z_q)	$8.77 \cdot 10^6$ kg/m^{2}s

Table 2.1: Effective physical properties of AT-cut crystalline quartz. Adapted from Bottom [32].

Because the frequency of the crystal is related to its thickness, there is a limitation in the manufacturing of high frequency fundamental crystals. The higher the frequency that is applied, the thinner the crystal blank should be.

The so-called *Q*-factor of a crystal is the quality factor of the motional parameters at resonance. The maximum frequency stability of a crystal is directly related to its *Q*-factor. The higher the *Q* factor is, the smaller the bandwidth appears and the steeper the reactance curve is. In order to provide stability of the resonance frequency, a high quality-factor and a minimized electromechanical coupling are needed. The quality-factor, *Q* is defined as:

$$Q = 2\pi \frac{energy\_stored\_per\_cycle}{energy\_dissipated\_per\_cycle} \qquad \text{Eq. 3}$$

The quality-factor of the shear mode oscillation in atmospheric air and room temperature of an AT-cut quartz is approximately $Q = 10^5$. The electromechanical coupling-factor *K* is determined by the resulting piezo-coefficient $e_q = 9.65 \cdot 10^{-2}$ C/m^2, the actual dielectric constant $\in_q = 4.54 \cdot \in_0$, where $\in_0 = 8.854 \cdot 10^{-12}$ C/(Vm) is the dielectric constant, and the shear modulus $\mu_q = 2.93 \cdot 10^{10}$ N/m^2

$$K = \sqrt{\frac{stored\_elastic\_energy}{stored\_electrical\_energy}} = \sqrt{\frac{e_q}{\mu_q \varepsilon_q}} \approx 0.091 \qquad \text{Eq. 4}$$

2.1.3 Impedance analysis

The measurements performed within this work, to study particle-surface contacts by quartz crystal resonator are based on impedance analysis. This is the methodology of using the conductance curve of the crystal. The conductance as a function of frequency is measured, therefore providing a means to electrically determine the acoustic resonance. The central parameters of measurements are the resonance frequency f, and the half-maximum-half-width, Γ. In resonance, both the amplitude of motion and the electrical conductance show a maximum. When the frequency of excitation matches the acoustic resonance frequency, the amplitude of oscillation becomes large. Simultaneously, the current through the electrodes, as well as the conductance, increases. Because the current is large on resonance, the resonance can be easily found with purely electrical instrumentation. Measuring the conductance around the resonance frequency, one obtains a resonance curve. The experimental results are fitted to a theoretical resonance curve, the *Lorentz curve*. The resonance frequency and the bandwidth are extracted from the fit [33,34]. A typical curve obtained by single measurement is presented in the Fig 2.3. The frequency shift is proportional to the area-averaged stress-speed ratio at the crystal surface, however complex the sample may be.

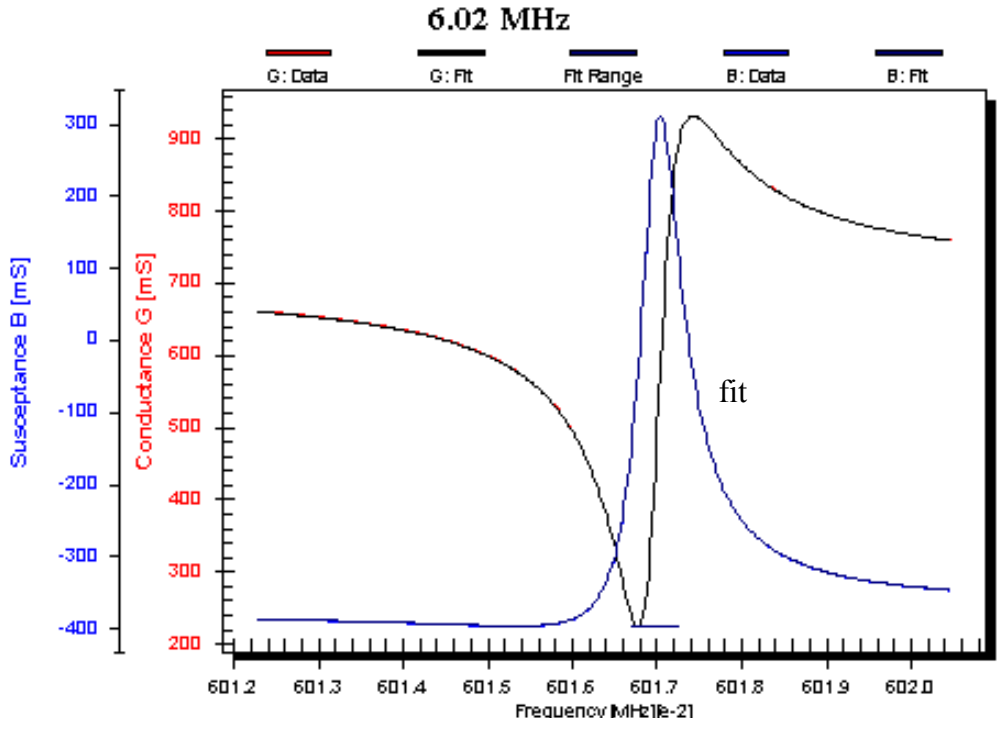

Fig. 2.3: Typical curve obtained by impedance analysis, fitted to a theoretical resonance curve – Lorentz curve (blue).

The impedance analysis, as described above, has significant advantages in the analysis of QCM experiments. Both the frequency and the bandwidth are obtained by a single measurement simultaneously. The additional parameters, such as the amplitude of the resonance, which is related to the effective area of the plate, and the offset of the susceptance, which is the imaginary part of admittance (inverse of impedance) with conductance being the real part. Both amplitude and susceptance, which is related to the dielectric environment of the resonator, are measured as well. However, the accuracy for the determination of the last two parameters is lower than the one obtained for the frequency measurement. Finally, impedance analysis offers the ability to measure a large number of higher harmonics, as high as e.g. 25 in air atmosphere or as high as 10 in liquid medium. Thereby the wavelength of shear sound can be varied.

2.1.4 Lateral amplitude distribution and energy trapping

In most cases, the oscillation of the quartz crystal resonator is confined to the centre of the quartz plate in order to minimize the effect of the holder onto the resonance. The shear amplitude of oscillation has a maximum in the middle of the electrode and decreases exponentially towards the rim. The quartz is only oscillating in the electrically excited area (electrode). The mechanism is based on the fact that the crystal is thicker in the centre than at the rim, due to the additional thickness of the electrodes. The edges of the quartz are not oscillating, thus, the holder for electrical contacting does not disturb the resonance properties at all. This phenomenon is called *energy trapping*. Sauerbrey investigated the dependence of the amplitude distribution on the geometrical quartz parameters such as the thickness of the quartz plate h_q, thickness of the electrodes h_e, diameter of the electrodes and the overtone order [35]. Figure 2.4.A shows the distribution of the amplitude across the area of the quartz plate for an 0.4 mm-thick (4 MHz) quartz plate with facets and an 0.17 mm thick (10 MHz) without. Sauerbrey concluded, that energy trapping becomes more effective with a) decreasing quartz plate thickness b) overtone order, due to the decreasing wavelength of sound, and c) thicker electrodes. What matters for energy trapping is the ratio of the thickness of the back electrode to the wavelength of sound. Figure 2.4.B shows the amplitude distribution of a 0.4 mm-thick (4MHz) quartz plate without facets. Here the amplitude distribution oscillates along the area of the electrode.

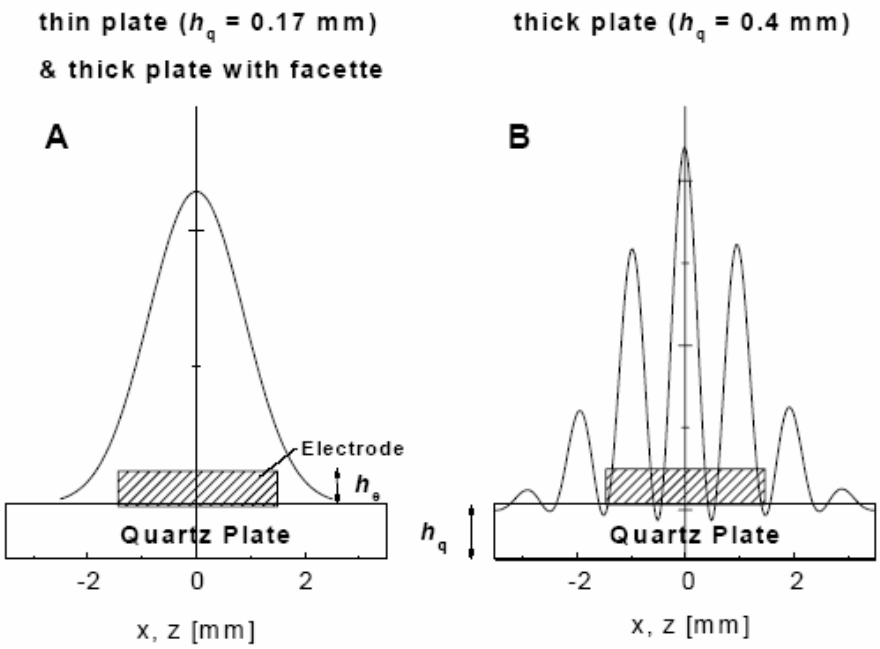

Fig. 2.4: Amplitude distribution along quartz plates (adapted from Sauerbrey [35]).

2.1.5 Equation predicting the amplitude of motion of quartz crystal resonators

The amplitude of motion is of substantial interest for experiments probing interfacial mechanical behaviour. Using the transmission line model published in 1948 by Mason, Johannsmann and Heim [36] have provided the simple equation, which predicts the amplitude of motion of quartz crystal resonators, u_o. They calculate the amplitude, u_0, from the speed as:

$$u_0 = \frac{1}{\omega}\dot{u}_0 = \frac{1}{2\pi n f_f}\frac{4}{n\pi Z_q}\frac{e_{26}}{d_q}QU_{el,o} = \frac{4}{\pi^2}\frac{1}{n^2}\frac{e_{26}}{Z_q c_q}QU_{el,0} = \frac{4}{\pi^2}\frac{1}{n^2}d_{26}QU_{el,0} \qquad \text{Eq. 5}$$

where f_f is the frequency of the fundamental, n is the overtone order, Q is the quality factor, $\dot{u}$ is the lateral speed of motion. The parameter $d_{26} = 3.1\times10^{-12}$ V/m is the piezoelectric strain coefficient. The driving voltage $U_{el,0}$ is often quoted in terms of the electrical power in units of decibel, where 0 dBm corresponds to a power of 1mW (see Chapter 4.1).

When the dBm values are used, the equation is simplified to the form of:

$$\frac{a}{QU_{el}} = \frac{4}{\pi^2}\frac{1}{n^2}d_{26} = 1.25\frac{1}{n^2}\frac{pm}{V} \qquad \text{Eq. 6}$$

During this work the applied amplitude of the quartz oscillation was calculated using the above equation.

Concerning the energy trapping and amplitude distribution it can be assumed the mass-sensitive area is situated in the central part of the resonator, covering about the area where the two electrodes overlap. Distribution of the mass sensitivity closely follows the vibration amplitude distribution. Both the mass sensitivity and amplitude distribution curves follow a Gaussian function [37].

Following Johannsmann [36], the effective area, A, of the quartz crystal resonator can be calculated from the Q- factor and the motional resistance R_1

$$A = \frac{G_{\max}}{Q}\frac{n\pi}{32Z_q d_{26}^2 f_f^2} \qquad \text{Eq. 7}$$

where $G_{\max} = \frac{I_{el,0}}{U_{el,0}}$ is the peak conductance ($I_{el,0}$ – electric current, $U_{el,0}$ – voltage), and is one of the fit parameters in impedance analysis, it is the inverse of the motional resistance R_1. The factor $Z_q = 8.8\frac{kg}{m^2 s}$ is the acoustic impedance of AT-cut quartz, and f_f is the fundamental resonance frequency. The larger the effective area is the more current is drawn at the peak of the resonance. The back electrode confines the amplitude to the centre of the crystal via energy trapping.

2.1.6 The Butterworth-van-Dyke (BvD) electrical equivalent circuit

The quartz resonators with their piezoelectric properties can be described or modelled as an electro-acoustic body. The electrically measured parameters correspond to the acoustic (equivalently mechanic) properties. Thus, an exact electrical equivalent circuit can describe the acoustic correlations and operating conditions of the quartz.

In a first step, the electromechanical analogy has to be introduced, in order to model the studied QCM system and help with the results interpretation. One can formulate electric analogies of all acoustic phenomena and vice versa. The electromechanical analogy maps forces onto voltages and speed onto currents [38], the ratio of force and speed is termed "mechanical impedance". However, for electroacoustic analogy stresses are mapped onto voltages and the stress-speed ratio is called "load impedance or "acoustic load".

The mechanical model of the oscillating crystal [39] consists of a dashpot *r*, a mass *m* and a spring, which possesses a spring constant *k*. Moving the mass *m* by an external force $\tilde{F}$ provokes an oscillation. The equivalence is outlined in detail in the Table 2.2.

This circuit contains a resistance, a capacity and an inductance connected in series and an additional capacity connected parallel to the series circuit. The oscillating mass *m* is equivalent to the inductance L_q, the dashpot *r* is represented by the resistance R_q, the spring constant *k* corresponds to the capacity C_q and the external force $\tilde{F}$ is equivalent to the alternating voltage, $\tilde{U}$. For frequencies much larger than the resonance frequency of the quartz crystal, it behaves like a capacitor with a capacity determined by the dielectric property of the resonator, C_0, the individual parameters can be calculated.

Mechanical	**Electrical**
Force = Area · Stress $F = A \cdot \sigma$	Voltage U
Speed $\dot{u}$	Current I
Mechanical Impedance $Z_m = \frac{F}{\dot{u}} = A\frac{\sigma}{\dot{u}}$	Electrical Impedance $Z_{el} = \frac{U}{I}$
Mass m_p $Z_m = \frac{F}{\dot{u}} = i\omega m_p$	Inductance L $Z_{el} = i\omega L$
Dash pot with Drag coefficient ξ $Z_m = \xi$	Resistance R $Z_{el} = R$
Spring with Spring constant κ $Z_m = \frac{F}{\dot{u}} = \frac{F}{i\omega u} = \frac{\kappa}{i\omega}$	Capacitance C $Z_{el} = \frac{1}{i\omega C}$

Table 2.2: Electromechanical equivalence.

The quartz crystal can be represented electrically by the circuit shown in Fig. 2.5. The motional inductance (L_m), motional capacitance (C_m), motional resistance R_1 and a parallel capacitance C_0 and series resistance in all there motional parameters can be measured using a crystal impedance (CI) meter [40].

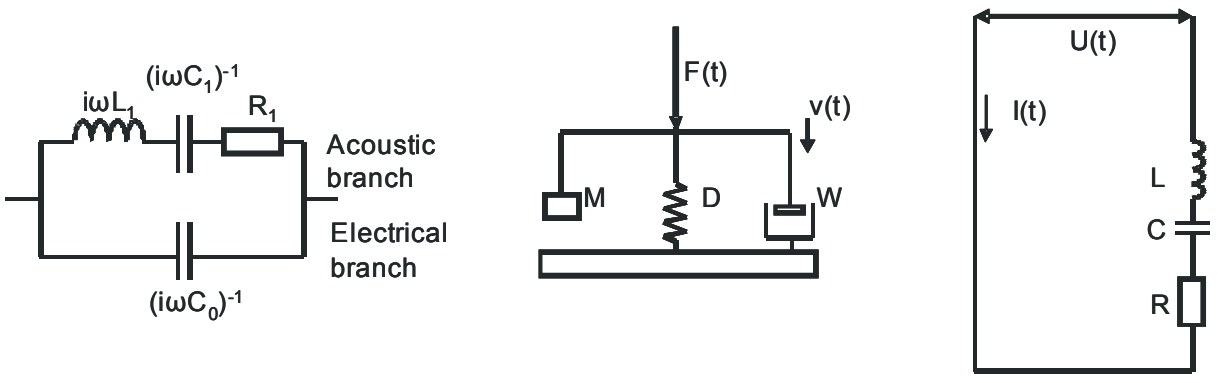

Fig. 2.5: Butterworth-van Dyke equivalent circuit for a quartz crystal resonator and electro-mechanical analogy (adopted from Berg [41]). Acoustic is the part of the system which resonates in the specific frequency range and electric is the branch where the mechanical is transformed to electrical energy.

Below shown are the fundamental equations used to describe the circuit.

motional inductance: $$L_m = \frac{\rho_q h_q^3}{8Ae_{26}^2}$$ Eq. 8

motional resistance: $$R_m = \frac{d_q^2}{8Ae_{26}^2} Z_q n\pi \tan\delta$$ Eq. 9

motional capacitance: $$C_m = \frac{8Ae_{26}^2}{d_q (n\pi)^2 AG_q}$$ Eq. 10

parallel capacitance: $$C_0 = \frac{A\varepsilon\varepsilon_0}{h_q}$$ Eq. 11

with ρ_q the density, h_q the thickness of the plate, A the effective area, $e_{26} = 9.65 \times 10^{-2}$ C/m^2 a piezoelectric coefficient, Z_q the acoustic impedance, tan(δ) = G_q"/G_q' the loss tangent, n the overtone order, G_q the storage modulus, ε the dielectric constant of quartz, and ε_0 the dielectric permittivity of vacuum. The meaning of the parallel capacitance can be readily explained and consists of the electrical capacitance across the electrodes. The parameters L_m, R_m, and C_m are not strictly electrical quantities, but rather describe the mechanical response of the system.

With regard to the graphical representation of mechanical elements there is a subtlety: when two mechanical elements are placed in series, their elongations add up, while the force transmitted through the elements is constant. On the contrary, when two electrical elements are placed in series, the voltages are additive and the current is constant.

The piezo-effect is graphically represented as a transformer in Fig. 2.5. The transformer turns mechanical quantities into electrical ones according to a parameter termed 2ϕ, which can be calculated by:

$$\phi = \frac{Ae_{26}}{h_q}$$ Eq. 12

Using the above given parameter, the lateral speed at the crystal surface can be calculated as:

$$\dot{u} = \frac{1}{2\phi} I_m$$ Eq. 13

The resulting stress is equivalently:

$$\sigma = 2\phi U_m \qquad \text{Eq. 14}$$

and the mechanical impedance is given by the following relation:

$$Z_{mech} = 4\phi^2 Z_m \qquad \text{Eq. 15}$$

here, $\dot{u}$ is the lateral speed at the crystal surface, σ is the stress, $Z_{mech} = A\sigma / \dot{u}$ is the mechanical impedance, A is the active area (which is similar but not identical to the area of the back electrode and may vary with overtone order), $e_{26} = 9.65 \times 10^{-2}\,\mathrm{C/m^2}$ the piezoelectric stress coefficient, and h_q the thickness of quartz plate.

The BvD equivalent circuit possesses two resonance frequencies due to the parallel configuration, the antiresonance f_A, corresponding to the whole circuit, and the series resonance f_s, corresponding to the upper serial branch and the quartz resonance frequency (noted as acoustic branch in Fig. 2.5) [42]. The two resonance frequencies can be calculated by Kirchoff's laws:

$$f_A = \frac{1}{2\pi}\sqrt{\frac{1}{L_q}\left(\frac{1}{C_q}+\frac{1}{C_0}\right)} \qquad \text{Eq. 16}$$

$$f_s = \frac{1}{2\pi}\sqrt{\frac{1}{L_q C_q}} \qquad \text{Eq. 17}$$

2.2 Quartz crystal microbalance

Quartz crystal is used for a wide range of applications and responds to many other experimental parameters and conditions, such as temperature, applied stress, and viscosity of the surrounding medium. The capability of microweighing gave the quartz crystal microbalance its name. The quartz crystal microbalance technique has been used to measure mass of the deposited thin films for over 50 years. This method for mass measurements was introduced in 1959 by Sauerbrey [43] and became a largely used instrument for small mass measurements in vacuum, gas and liquid phase [38,41,44]. The use of QCM as a mass change detector is the most widely known. The new challenge is to combine the quartz crystal resonator with other techniques such as surface plasmon resonance spectroscopy (SPR), surface forces apparatus [45], atomic force microscopy (AFM), and others [34].

Usually the quartz crystal microbalance, QCM, is applied to measure the mass per unit area of homogeneous, rigidly attached thin films, and the analysis of microweight experiments is based on the Sauerbrey equation. During this study quartz crystal microbalance was used as a tool for contact mechanics experiments, based on the Sauerbrey model.

Furthermore, the QCM method can be used as a tool to determine viscoelastic properties of the films adjacent to the quartz surface from the combined evaluation of resonance frequency and bandwidth. However, this is outside of the scope of the present work and for further details one can refer to appropriate literature [46-52].

2.2.1 Sauerbrey equation – deposited mass calculation

Sauerbrey used the change in the frequency of a quartz resonator to measure the mass of a film adherently deposited on the quartz resonator surface [37]. He demonstrated that mass can be measured using vibrations and that frequency change is related to the mass change. Thus, it was possible to detect even 10^{-16} kg, while the commercial analytical microbalances can detect about 10^{-10} kg. This corresponds to a minimum detectable film thickness of 1Å. As such, this method would even deserve the name 'Quartz Crystal Nanobalance' [37]. This technique is based on the changes of the resonance frequency of an oscillating quartz crystal, when small masses are deposited homogeneously on its surface. Sauerbrey showed, that deposition of a rigid mass under vacuum or in air provokes a change of the resonance frequency Δf. This proportionality is given by the well-known Sauerbrey equation [43]:

$$\frac{\Delta f}{f_0} = -\frac{m_f}{h_q \cdot \rho_q} \qquad \text{Eq. 18}$$

where Δf is the frequency shift, f_0 is the resonance frequency in the unperturbed state, m_f represents the deposited mass, h_q is the quartz thickness and ρ_q = 2650 kg/m^3 denotes the quartz density. The frequency shift is negative when the mass of the composite resonator increases.

The Sauerbrey equation can also be applied for particle – surface contact mechanics if the spheres are tightly coupled to the crystal and they behave in essentially the same way as a solid film. When small, monodisperse particles are placed on top of the QCM and are tightly attached, one expects a frequency shift of:

$$\frac{\Delta f}{f_0} = -\frac{Nm}{A_q \rho_q h_q} \qquad \text{Eq. 19}$$

here, N is the number of particles on the active area of crystal A_q and m is the mass of each particle. If the particles are evenly spread across the surface of the crystal, the size of the active area does not matter. It is the areal number density of spheres N/A_q, which determines Δf.

2.2.2 Adsorption on the quartz crystal resonators

The impedance analysis, as described in 2.1.3. provides the resonance frequency f, and the half-maximum-half-width, Γ. In resonance, both the amplitude of motion and the electrical conductance show a maximum. Following the argumentation of Sauerbrey [43] the added mass would induce a frequency decrease and a peak broadening as demonstrated schematically in Fig. 2.6, where the resonance curves (Lorentzians) of an unloaded and loaded quartz resonator are presented.

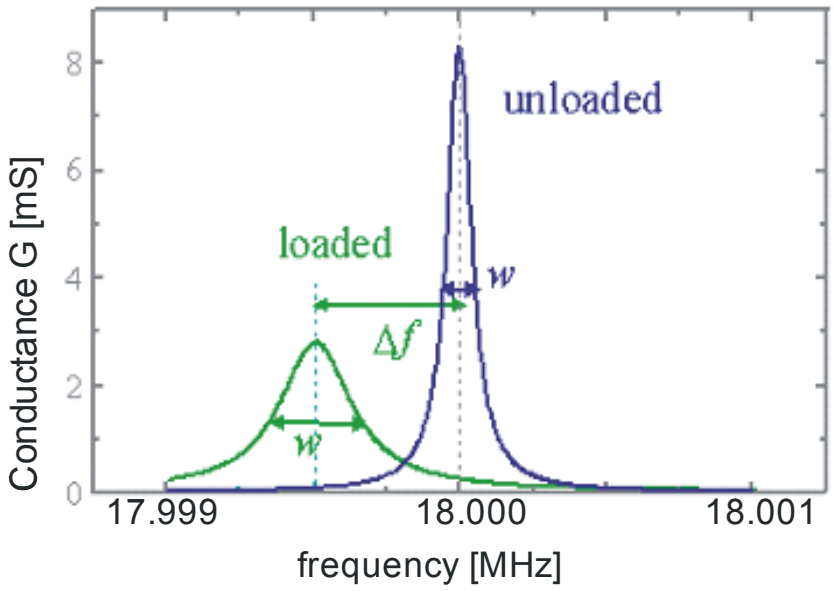

Fig. 2.6: Typical resonance curves (Lorentzians) for an unloaded and loaded quartz crystal resonator. After Johannsmann [38]

The complex frequency is derived from the measured resonance frequency and is defined as:

$$f^* = f + i\Gamma \qquad \text{Eq. 20}$$

with f being the resonance frequency and 2Γ the bandwidth of the resonance at half maximum. The resonance frequency is a measure of the elastic properties of the quartz and the matter on its surface. Any dissipative phenomena taking place at the quartz surface are

manifested in the bandwidth change. Therefore, for contact mechanics experiments with particles on a quartz surface, a decrease of resonance frequency would be expected.

However, there are cases were a frequency increase was observed, such as for the systems studied below in paragraphs 5.3. and 5.4. This apparent contradiction can be explained by means of coupling character between particles and surfaces. The simple analogy of a spring (with spring constant k) – mass (m) system illustrates this principle: its resonance frequency is written as: $\omega = \sqrt{k/m}$. Since no mass is being withdrawn from the resonator, it is believed that the increase of the frequency is due to the increased stiffness of the quartz-sphere system, a phenomenon that will be discussed in more detail in Chapter 3.4 and Chapter 5. For all other applications the frequency shift is usually negative as a result of added mass to a resonator.

2.2.3 Physical interpretation of the Sauerbrey thickness

The calculation of the film thickness after the Sauerbrey equation (Eq. 18) results in a number for the areal mass (mass per unit area) – the 'Sauerbrey mass'- and the corresponding thickness, the so-called Sauerbrey thickness [38]. Since the equation is linear in the mass per unit area, it also holds an average sense. If the sample has a non-uniform thickness, the QCM determines an average mass per unit area, and a statistical weight has to be included in the analysis. The sensitivity of the method is further influenced by the distribution of the vibrational amplitude and the effective area. The latter is undefined and has the maximum in the center of the crystal while it smoothly decays towards the rim, due to energy trapping [53]. Therefore, deviations between the actual geometrical thickness of the film, and the one predicted by the Sauerbrey model are expected.

Vig [53] and later Johannsmann [38] evidenced many aspects for these deviations. The most common is the one based on non-uniform distributed mass. For example, a small mass deposited outside the electrode of a QCM changes the normalized fundamental mode frequency of the QCM more than it changes the normalized third overtone frequency. Outside the electrodes, the amplitude of vibration of the third overtone falls off faster with distance from the electrode edges. If a mass is deposited onto a node of the third overtone mode of vibration, then the third overtone frequency is not changed by the mass, however the fundamental mode frequency is. Significant deviation from the Sauerbrey equation will also

occur when the mass is not rigidly coupled to the QCM surface [53]. Johannsmann pointed out the conversion from areal mass density to thickness which usually requires the physical density as an independent input [38]. It must be also considered that the complex samples are laterally heterogeneous and have often fuzzy interfaces. That will often lead to corrections due to viscoelasticity and consequently to a non-zero change in the bandwidth of the resonance at half-maximum $\Delta\Gamma$ as well as an overtone-dependent Sauerbrey mass. A further case would be deviations due to the solvent contained in the film, that in fact contributes to the 'Sauerbrey thickness'. This is because the solvent takes part in the movement. The mass of the solvent influences the frequency response and increases the value of the Sauerbrey film thickness. However, it does not contribute to the optic thickness, because the electronic polarizability of a solvent molecule does not change when it is located inside a film. The optical thickness can be determined by, for example, surface plasmon resonance (SPR) spectroscopy or ellipsometry.

3. Mechanical contact between bodies

The main focus of this work lies on the experimental study of mechanical contacts on the micro- and nanoscale. Adhesion at the nanoscale is a consequence of electrostatic interactions between surface dipoles and charges, van der Waals interactions, as well as capillary phenomena [10]. In order to understand the interaction between contacting bodies, the fundamentals of effective forces and mechanical properties have to be introduced. In this chapter, an overview of corresponding theories for surface forces, adhesion laws and elastic deformation are described. First a review of van der Waals forces related to adhesion force between curved surfaces is given. Secondly, models describing the deformation of the contact area between two macroscopic bodies are introduced. Finally, within this chapter, the theoretical models related to particle-surface coupling during oscillation are presented.

3.1 Surface forces

Surface forces determine the interaction type and intensity between the surfaces of all solids. They control e.g. aggregation and adhesion and are therefore responsible for even macroscopic properties. When two bodies are brought into mechanical contact, attractive surface forces will lead to adhesion [54]. The adhesion force is defined as the maximum force necessary to separate the two bodies, will depend on the strength of the attractive interaction, the contact area between bodies, and the interaction energy per unit area, $V^A(X)$, between the materials. This means that the adhesion force between two objects can arise from a combination of different contributions such as the van der Waals force, electrostatic force, chemical bonding, and hydrogen bonding forces, capillary forces, and others (e.g., bridging or steric forces on polymer-coated surfaces). The adhesion force between two materials may therefore depend not only on the materials in contact and their intrinsic properties, but also on the ambient conditions. For micro- and nanocontacts, capillary condensation and thus the relative humidity may have a strong influence on the adhesion force. Furthermore, the assumption of rigid bodies is in most cases an oversimplification when it comes to correctly describe adhesion between solids. Bodies in contact will deform due to either external or surface forces. This means that, for understanding the phenomenon of adhesion, not only the adhesion energy of the materials but also the information about the deformations is required.

Adhesion forces between macroscopic bodies such as particles and surfaces are a result of electrostatic forces (Coulomb), capillary forces and the Van der Waals interactions. The Van der Waals forces between atoms and molecules is the sum of three different forces, all proportional to $1/r^6$, where r is the distance between the atoms or molecules. These forces are: i) the orientation or Keesom force, ii) the induction or Debye force, and iii) the dispersion or London force [55]. In the question which of the above mentioned forces will dominate the adhesion process, the answer depends on environmental conditions during the experiments and the physicochemical properties of the material that are in contact [56]. Moreover at a smaller scale, for surface separations below a few nanometers or 4 – 10 molecular-diameter characteristic lengths, the forces based on the structural form of contacting bodies have to be additionally considered [1], i.e. solvatation forces which are important for structured medium between solid bodies. The most common types of surface forces and their main characteristics are listed, as taken from Bhushan [57], in the Table 3.1.

The total adhesion is assumed to be the sum of the acting surface forces [3], as eq. 21 illustrates:

$$F_{ad} = F_{vdw} + F_c + F_{es} + F_{chb} \qquad \text{Eq. 21}$$

where, F_{ad} is the total adhesion force; F_{vdw} is the Van der Waals force; F_c is the capillary force; F_{es} is the electrostatic and F_{chb} denotes the chemical bonding forces. However, it is known that for dry and chemically inert powders, without chemical bonds and in the absence of an external electric field, the adhesion is usually due to only Van der Waals interactions [3].

The detailed analysis of all the forces described above is not the purpose of this work. For the investigated systems within this study, van der Waals forces certainly the dominating force to keep the particles at the surface for the specific experimental setup.

The Van der Waals forces are a result of interactions between dipole moments of atoms and molecules. They arise from the attraction of opposite electric charges, as for chemical bonding. Areas of the molecule with electron abundance lead to a partially negative load and are attracted by areas with an electron deficit (partially positive) of other molecules. These forces are secondary bond forces and are much weaker than the primary ones, such as covalent, ionic and metallic. Van der Waals forces are less dependent of the chemical structure of the materials. Furthermore they have a relatively greater reach. The equation for the van der Waals force between a sphere and a planar surface is given by:

$$F_{vdW} = \frac{A_H R}{6D^2}$$ Eq. 22

where A_H is the material specific Hamaker constant, D is the distance between the surfaces of sphere and plane and R is the particle radius.

Type of force	Subclasses	Main characteristic
Attractive forces		
van der Waals	Debye induced dipole force London dispersion force Casimir force	Ubiquitous, occurs both in vacuum and in liquids
Electrostatic	Ionic bond Coulombic force Hydrogen bond Change-exchange interaction	Strong, long-range, requires surface charging or charge-separation mechanism
Quantum mechanical	Covalent bond Metallic bond Exchange interaction	Strong, short-range, responsible for contact binding of crystalline surfaces
Repulsive forces		
Electrostatic	Coulomb force	Arises only for certain constrained surface charge distribution
Quantum mechanical	Hard-core or steric repulsion, Pauli repulsion	Short-range, stabilizing attractive covalent and ionic binding forces, effectively determine molecular size and shape
Dynamic interactions		
Non-equilibrium	Friction forces	Energy-dissipating forces occurring during relative motion of surface or bodies

Table 3.1: Selection of surface forces (adopted from Bhushan [57]).

3.2 Surface forces measurements techniques

The development of the theory of van der Waals forces stimulated an interest in measuring forces between surfaces to provide with a verification [58]. The most unambiguous way to measure a force-law is to position two bodies close together and directly measure the force between them, e.g., from the deflection of a spring. Techniques that are used nowadays for measuring the interactions between surfaces in vapours or liquids of macroscopic, colloidal and atomic dimensions let us study both static (i.e. equilibrium) and dynamic (e.g. viscous) forces. These methods provide precise information not only on the fundamental interactions but also into the structure of liquids adjacent to surfaces and other interfacial phenomena [1]. Particle adhesion and friction forces can be measured using various techniques [59]. However, the possibilities to study these phenomena between single particles or single particles and a surface are limited [60]. Direct measurements of adhesion forces, or rolling and sliding friction of microscopic particles are technically demanding, expensive, and of limited applicability. Currently, the most widely used techniques to determine experimentally the adhesion force between microscopic particles and surfaces are the atomic force microscopy (AFM) and the centrifuge technique [3].

Though both techniques provided us with valuable insights, they also have their limitations. Both are not applicable for routine applications and are experimentally demanding. With the centrifuge the contact times are long (in the range of hours) and after detachment no further experiments can be carried out with the same particle [61]. In the case of AFM experiments, each individual particle has to be attached to the end of cantilevers and the direction of contact is predetermined and not free to adjust [29]. The atomic force microscopy shows limitations when the adhesion of poly-dispersed sizes on a surface is studied. This technique can only determine the adhesion of a single particle per experiment, leading to a considerable effort to achieve a representative value for the adhesion force. However, it can also deal with irregular shaped particles after adapting the technique accordingly. The results are statistically treated to obtain the mean adhesion force of the particles. The centrifuge technique holds the advantage of determining the adhesion force of polydisperse powder materials and can be used to measure the adhesion force for particles with irregular shapes and rough surfaces. In the centrifuge, particles can change their orientation to adopt a configuration with lower energy. This possibility may lead to higher adhesion [3] compared to an AFM experiment. Finally, the centrifuge can also be applied to study particles with irregular or non-ideal shapes.

3.2.1 Atomic Force Microscopy

The atomic force microscope, AFM, had been invented by Binning, Quate and Gerber [62]. This technique, based on measuring attractive or repulsive forces between a tip and the sample, has become the most acknowledged instrument to image the topography of a sample. Firstly, operated in the repulsive/contact mode AFM is able to image the topography of surfaces with high resolution on the nanometer scale. Secondly the AFM can also be operated in the force spectroscopic mode allowing to measure surface forces [63-65]. Forces are detected by measuring the deflection of a very flexible cantilever beam having an ultra-small mass [57]. The force required to deflect this beam by measurable distances (10^{-2} Å) can be as small as 10^{-11}N. Below this force level, thermal noise is significant and affects the experimental results [66]. This level of sensitivity clearly enters the regime of interatomic forces between single atoms [62]. The measuring principle of a standard AFM is outlined below. The poorly defined geometry of the AFM tip pushed Ducker [67,68] et al. and Butt [69] to develop a new measurement technique the so-called colloidal probe method. This technique is described in more detail in Chapter 6.

Surface topography

The AFM technique can be utilized in order to determine surface topography, i.e. quality and possible changes from interactions. These can be quantified with the AFM in two commonly used modes, which are briefly presented here. In both methods, the sample is laterally scanned under the tip while simultaneously the separation-dependent force or force gradient between the tip and sample is measured [57].

The first is the so-called contact mode for which the tip touches the surface and the interaction force between tip and sample is measured by recording the cantilever deflection. While the tip touches the surface, the cantilever is bent upwards. In order to minimize the bending the piezo adjusts the sample height. The advantage of this mode is that the scanning can be much faster than for tapping mode. Furthermore a high resolution of the images can be achieved even in liquids and polymer melts.

In the intermittent contact, or so-called tapping mode, which was used within this work, the cantilever oscillates at the resonance frequency close to the surface and the change in oscillation amplitude due to damping is measured. At the end of the cantilever (at the tip position) the vibration amplitude is typically 1-10 nm [29]. Instead of scanning the surface at constant deflection or constant height, the sample is scanned at constant reduction of the

vibration amplitude. As a result, for most of the measurement time the tip is not in actual contact with the surface. The oscillating tip slightly taps the surface at the resonant frequency of the cantilever (70 – 400 Hz) with constant oscillation amplitude induced in the vertical direction with a feedback loop keeping the average oscillation amplitude constant. The oscillation amplitude is kept large enough so that the tip does not get stuck to the sample because of adhesive attraction. The tapping mode is used in topography measurements to minimize effects of friction and other lateral forces, especially when the determining the topography of soft surfaces.

Force measurements

The AFM can be used to measure local material properties and interactions between different samples. In a force measurement the force between a sample surface and a microfabricated tip is determined. The tip is located at the end of an ~100 µm long and 0.4-10 µm thick cantilever and the force vs. distance curve is obtained [58]. Alternatively, colloidal particles are fixed on the cantilever. This technique is called 'colloidal probe technique'. Within this work this technique was applied to measure forces by AFM. The deflection of the cantilever is commonly measured using the optical lever technique (Fig. 3.1).

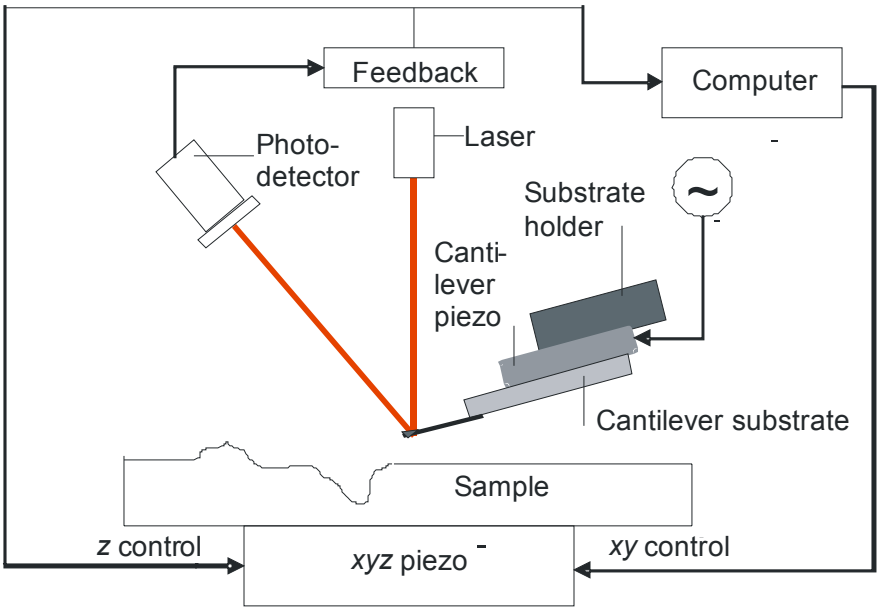

Fig. 3.1: Schematic of tapping mode used for surface roughness measurements (after Bhushan [57])

In an AFM force measurement, the sample is moved up and down by the piezoelectric scanner. In order to detect the movement of the tip, a beam from a laser diode is focused on the back of the cantilever. From this point the laser beam is reflected towards a sensitive photodetector that monitors its position. If the cantilever moves, the position of the reflected beam changes. The backside of the cantilever is usually covered with a thin gold layer to enhance its reflectivity. When a force is applied to the probe the cantilever bends and the reflected light-beam moves on the detector. With the help of the photodetector this change is converted into an electrical signal. The direct result of such a force measurement is the detector signal in volts, ΔV, versus the position of the piezo Δz_p, normal to the surface (Fig. 3.2.). To obtain a force-versus-distance curve, ΔV and Δz_p have to be converted into force and distance. To calculate the cantilever deflection from the detector signal, the corresponding conversion factor is needed which can be obtained from a linear fit of the 'constant compliance' region. The tip-sample separation is then obtained by subtracting the cantilever deflection from the piezo position. The force acting on the cantilever, F, is obtained by multiplying its deflection with its spring constant of the cantilever [29].

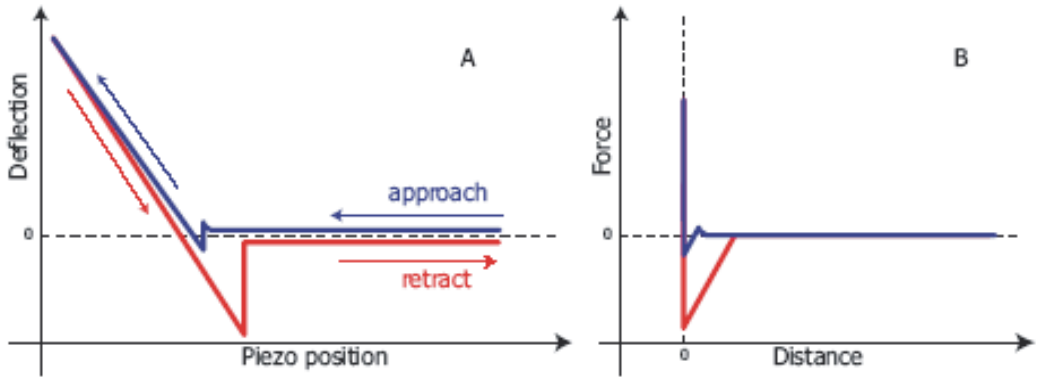

Fig. 3.2: Example of a force-distance-curve calibration. The two linear parts (zero force at constant compliance) are used to fix zero force and distance. a) deflection-piezo position curve which is directly measured, b) the calibrated force curve.

3.2.2 Centrifuge technique

The centrifugal force, which is required to detach particles from a planar surface, is measured by mounting the surface on an ultracentrifuge and rotating them at a defined speed. Detachment force of particles is determined from pictures of the surfaces taken after each run with increasing speed [54]. The centrifuge technique to measure adhesion force is based on the principle of centrifuge force applied on a particle rotating at a specific angular speed (Fig. 3.3). The particle has a defined mass and a specific position at a known distance from the rotation center. The centrifugal force will exceed the adhesion force between the particles and the surface above a critical centrifugal speed [3]. The centrifuge technique utilizes imaging analysis to determine the number of adhered particles on the proof disk surface before and after each centrifugation. Two centrifuge forces can be applied [70]: (i) the pressure force on the particles (press-on), which is applied to increase simultaneous contact between the particles and the substrate, where the sample is put with the side of the particles surface facing the centre of the centrifuge; and (ii) the force used to detach the adhered particles (spin-off), where the sample is placed in the centrifuge in the opposite direction of the previous case, in order to allow particle detachment from the surface. This first one is normally used to uniformize the particle deposition on the flat surface and their interaction with the surface, prior to the detachment tests. Additionally friction forces can be measured by turning the studied surface horizontally.

The centrifuge force F_{cen} generated in the compression or detachment direction, can be calculated as follows [7]:

$$F_{cen} = M\omega^2 d_c \qquad \text{Eq. 23}$$

where M is the mass of the particle; ω is the angular speed, that is limited due to the material stability of the rotor. This restricts adhesion measurements using the centrifuge method to particles larger than a few microns. The detachment of the particle will occur at a critical detachment angular speed, ω_d. Finally, d_c is the distance between the sample and the rotor centre (rotational axis). It is assumed that the adhesion force is equal in magnitude, but with opposing signal to the applied centrifugal force at detachment, as seen in Eq. 24

$$F_{ad} = -F_{cen}$$ Eq. 24

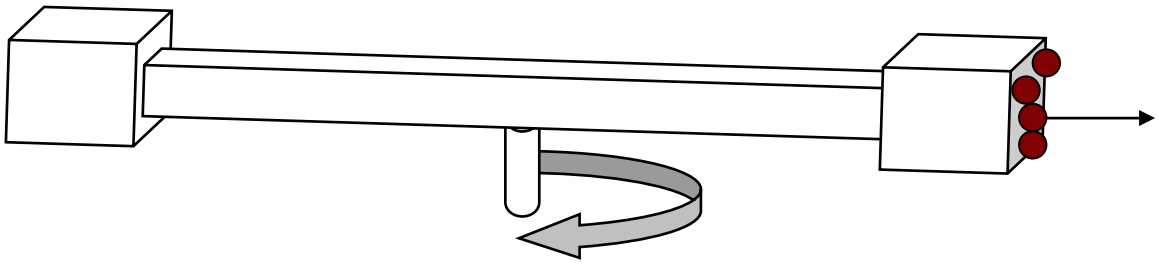

Fig. 3.3: Schematic of the centrifuge method to determine adhesion forces of particles on surfaces. Friction forces can also be analyzed when the particles are placed on a horizontal surface [54].

3.3 Van der Waals interactions between particles and surfaces

In order to describe the Van der Waals interactions between two particles, the individual forces acting between them are summed [3]. Here one has two possible approaches. The first is the summation over all molecules in the particles and not solely the particle surfaces. This is called the microscopic approach. However, it assumes a pairwise additivity of forces between all molecules, which in not necessarily true for all cases. The second approach is the macroscopic, or Lifshitz theory. This theory is derived from continuum quantum electrodynamics. It refers to interactions between macroscopic objects and expresses the dispersion forces as a function of distance in terms of bulk material properties, such as dielectric constants ε and refractive indices n.

Microscopic approach

In order to calculate the magnitude of the interaction between macroscopic bodies, e.g. a point charge and an infinitely extended plane, it is necessary to integrate over the molecular density of the entire plane. The potential between two molecules is $W=-C/D^6$, with C being the constant depending on the materials of interacting objects and intervening medium properties and D is the distance between them. The minus sign (-) refers to the attractive

character of the van der Waals forces [1,58]. The molar density ρ_B is integrated over the entire volume of the solid. By assuming a constant density of the molecules in the solid, the van der Waals energy between a molecule *A* and an infinitely extended body with a planar surface made of molecules *B* can be derived as follows:

$$W_{Mol/Plane} = -\frac{\pi \rho_B C_{AB}}{6D^3} \qquad \text{Eq. 25}$$

Integration over all molecules in the solid *A* leads to the van der Waals energy between two infinitely extended solids witch are separated by a parallel gap with the thickness *D*. The energy is given per unit area:

$$w = \frac{W}{A} = -\frac{\pi \rho_A \rho_B C_{AB}}{12D^2} \qquad \text{Eq. 26}$$

where *w* is the area dependent potential energy and ρ is the molecular densities, more precisely the number of atoms per unit volume. The negative derivative of *w* versus the distance is calculated and gives the force per area:

$$f = -\frac{A_H}{6\pi D^3} \qquad \text{Eq. 27}$$

with A_H as the Hamaker constant, that depends on the material characteristics and is defined as:

$$A_H = \pi^2 C_{AB} \rho_A \rho_B \qquad \text{Eq. 28}$$

Macroscopic theory – Lifshitz theory

In order to calculate the van der Waals forces between two surfaces, Lifshitz introduced a different way to determine the Hamaker constant by integrating over the static and frequency dependent dielectric permittivity of the materials [1,58]

$$A_{AB} \approx \frac{3}{4} k_B T \left(\frac{\varepsilon_1 - \varepsilon_3}{\varepsilon_1 + \varepsilon_3} \right) \left(\frac{\varepsilon_2 - \varepsilon_3}{\varepsilon_2 + \varepsilon_3} \right) + \frac{3h}{4\pi} \int_{\nu_1}^{\infty} \left(\frac{\varepsilon_1(i\nu) - \varepsilon_3(i\nu)}{\varepsilon_1(i\nu) + \varepsilon_3(i\nu)} \right) \left(\frac{\varepsilon_2(i\nu) - \varepsilon_3(i\nu)}{\varepsilon_2(i\nu) + \varepsilon_3(i\nu)} \right) d\nu \qquad \text{Eq. 29}$$

Lifshitz neglects the atomic structure of the materials and treats the solid as continuous media with certain optical properties. Here, ε are the static dielectric permittivities and $\varepsilon(i\nu)$ are the dielectric permittivities at the imaginary frequency $i\nu$, and $\nu_1 = 2\pi k_B T/h = 3.9 \cdot 10^{13}$ Hz at 25°C. The $\varepsilon(i\nu)$ can be written as:

$$\varepsilon(i\nu) = 1 + \frac{n^2 + 1}{1 + \nu^2 / \nu_e^2} \qquad \text{Eq. 30}$$

where n is the refractive index and ν_e is the main electronic absorption frequency in the ultraviolet, which is typically $3 \cdot 10^{15}$Hz. Both eq. 29 and 30 are approximations of the complete Lifshitz theory, in order to simplify the problem.

Nevertheless, both microscopic and macroscopic approaches, lead to essentially the same equations, with however a different calculation of the Hamaker constants.
Hamaker [61] proposed eq. 31, for calculating Van der Waals forces between a sphere of diameter d_s and a planar surface in contact:

$$F_{vdw} = \frac{A_H R_s}{6 Z_0^2} \qquad \text{Eq. 31}$$

where Z_0 is shortest separation distance between two surfaces and typically in the range of atomic dimensions, R_s is the particle-radius and A_H is the Hamaker constant.

The determination of the separation distance, Z_0, between two particles is the major difficulty in using eq. 31. This is due to the fact that this characteristic distance must always be defined for a new system and depends on several system-specific parameters. The definition of the

distance between macroscopic bodies, that is to be used in a force-law, depends on the specific body geometries. The most prominent examples are the plane-plane, the crossed-cylinders (used e.g., in a surface forces apparatus), and the sphere-plane geometry. The respective interaction energies are:

$$W_{p-p} = -\frac{A_H}{12\pi D^2} \qquad \text{Eq. 32}$$

The above equation provides with the energy per unit area for two parallel planes with infinite extension and is therefore independent of the contact area, A.

$$W_{cyl} = -\frac{A_H \sqrt{R_1 R_2}}{6D} \qquad \text{Eq. 33}$$

The curvature of the cylinder surface, given by R_1 and R_2, defines the actual characteristic distance for van der Waals interactions and is valid for infinitely long cylinders, i.e. with length $L >>$D.

$$W_{sp-pl} = -\frac{A_H R}{6D} \qquad \text{Eq. 34}$$

with D being the surface separation and R_1, R_2 the radii of the contacting spheres. For $R_1 = R_2$ the crossed-cylinders interaction equals that of a sphere-plane contact. The theoretical calculation for surface forces is mostly carried out for the plane-plane geometry. To transform these to the force laws for curved surfaces one can use the Derjaguin approximation, which will be presented in the next paragraph.

3.4 Contact models

It is well acknowledged that no solid material is completely rigid. Thus, two bodies in contact deform as a result of surface forces and/or applied normal force. Particles and/or substrates deform elastically and/or plastically under applied loads during adhesion, and particles-substrate analysis requires more accurate contact mechanics models, which should include a physical deformation component. The equations introduced above to calculate the interaction forces can in principle be used to calculate the adhesion force between rigid objects. In order to extend this to real bodies, one has to take the contact deformation into account. Several models have been developed to understand the adhesion, especially between. spherical particles and a flat substrate. One approximation would be to take the particles as perfectly rigid in contact. However this would limit the validity for systems with a small distance between the sphere and the substrate, i.e. shorter than the sphere radius. In order to avoid this limitation on interaction distance, an applicable approximation would be to consider an elastic contact between particles and substrate.

For the simple case of two interacting elastic spheres or an elastic sphere interacting with a non-deformable surface and in the absence of attractive surface forces, the vertical central displacement (compression) was derived by Hertz. In this model, the displacement and the contact area are equal to zero when no external force (load) is applied, i.e. at the point of contact and of separation.

In systems where attractive surface forces are present between the surfaces, the deformations are more complicated to determine. When a normal force is applied on the particles they deform in a way which is determined by the elastic and viscoelastic properties of the particle and the substrate material [71]. Furthermore, the deformation is affected by the surface roughness, the interaction between them (i.e. surface forces), and by any externally applied load [72]. Modern theories of the adhesion mechanics of two contacting solid surfaces are based on the Johnson-Kendall-Roberts (JKR) theory, or on the Derjaguin-Muller-Toporov (DMT) theory (Fig. 3.4). Furthermore, the Maugis theory can be considered which actually unifies the latter two approaches. The JKR theory is applicable to easily deformable, large bodies with high surface energy, whereas the DMT theory better describes very small and hard bodies with low surface energy [73,74].

The Hertz Model

A first model for the contact mechanics of elastic bodies was given by Hertz [75] in 1882. He considered the non-adhering perfectly elastic sphere pressed into contact with a 'rigid wall' (Fig. 3.4). Hence, this model describes the elastic deformation of the bodies (spheres) but neglects any attractive surface forces. Therefore it cannot be used to calculate adhesion forces. The contact radius, r_c, between the sphere, with a radius R, and a flat surface is calculated as a function of load, L:

$$r_c^3 = \frac{R}{K} L \qquad \text{Eq. 35}$$

where the elastic constant K is defined through the elastic properties of contacting bodies

$$\frac{1}{K} = \frac{3}{4}\left\{\frac{1-\nu_1^2}{E_1} + \frac{1-\nu_2^2}{E_2}\right\} \qquad \text{Eq. 36}$$

where E_i are the elastic moduli and υ_i are the Poisson ratios of the two materials.

The JKR and the DMT models

Roughly hundred years after the study of Hertz, analytical models have been developed to predict the mechanical behaviour of ideal sphere-sphere or sphere-plane contacts including surface forces, notably the Johnson, Kendall and Roberts (JKR) [73] and Derjaguin, Muller and Toporov (DMT) [74] models. These models included the dependence of both the material properties and the surface geometry, on the force acting between two surfaces.

Johnson, Kendall, and Roberts (JKR) extended the theory to two adhering solids, i.e. to solids that stick together when in contact, due to their possessing a finite surface energy. This leads to a greater contact area under a given load than the one predicted by Hertz's theory, with a tensile stress near the periphery of the contact region and a compressive stress within the contact area. A finite tensile load is required to separate the solids, and depends only on the solids radii and surface energy. According to the JKR theory, a particle in contact with a flat substrate induces short range forces (adhesion and elastic forces) between the substrate and the particle. This leads to deformation of both the particle and the substrate at the point of

contact. According to the JKR theory a finite elastic modulus, *K*, while having an effect on the load-area curve, has no effect on the adhesion force. This is an interesting and unexpected result that was nevertheless been verified experimentally. Horn et al. [72] identified two notable consequences of the JKR theory: first, it predicts that the solids would separate abruptly from a finite area of contact once the load reaches a critical tensile value (the pull-off or adhesion force). Secondly, there would be an (unphysical) infinite tensile stress at the edge of the contact zone and that each surface would bend to form a right angle along this line.

From the other side, Derjaguin, Muller and Toporov (DMT) argued that any attractive force between solids must have a finite range. This force should therefore act in a region just outside the contact zone where the surfaces are a small distance apart. The DMT theory does not calculate the surface profile but assumes that the deformed shape of the surface is Hertzian, and unaffected by the surface forces. This removes the singularities in the stress distribution and in the gradient of surface profile. Following this model one will predict that: (i) the solids will separate only when the contact area has been reduced to zero, and (ii) that the pull-off force is 4/3 times greater than the value found by the JKR model [3, 72].

Both of these models, JKR and DMT, consider elastically deformable solids in contact with either sphere-sphere or sphere-plane geometrics. They predict a pull-off force necessary to separate the solid that can be written as:

$$F_{ad} = 2\pi R^* W_A \qquad \text{(DMT)} \qquad \text{Eq. 37}$$

$$F_{ad} = \frac{3}{2}\pi R^* W_A \qquad \text{(JKR)} \qquad \text{Eq. 38}$$

where R^* is the radius of the particle in the case of a sphere-plane contact or the reduced radius of the two particles for a sphere-sphere contact as defined by:

$$R^* = \frac{R_1 R_2}{R_1 + R_2} \qquad \text{Eq. 39}$$

R_1 and R_2 are the radii of two spheres in contact.

The equilibrium work of adhesion, W_A, is defined by the negative of the Gibbs free energy change per unit area of interacting interfaces, and is expressed by the Dupré equation:

$$W_A = \gamma_1 + \gamma_2 - \gamma_{12} \qquad \text{Eq. 40}$$

where γ is the surface free energy per unit area, subscripts 1 and 2 describe the different phases of the system and γ_{12}, which is the total free energy change, can be calculated from:

$$\gamma_{12} = \gamma_1 + \gamma_2 - 2\sqrt{\gamma_1 \gamma_2} \qquad \text{Eq. 41}$$

The difference between JKR and DMT models lies on the assumption of the nature of forces acting between particle and substrate. Johnson et al. [73] assumed in their model that active forces act only inside the particle-substrate contact area, whereas Derjaguin et al. [74] included long-range surface forces operating outside the particle-substrate contact area [3]. The JKR model could be used to describe the adhesion characteristics of large and soft particles while the DMT theory is applicable for small and harder particles. The JKR theory considers the adhesion between the two spheres simply as a change in surface energy only where they are in contact, i.e. that the attractive force between them is of infinitely short range outside the contact.

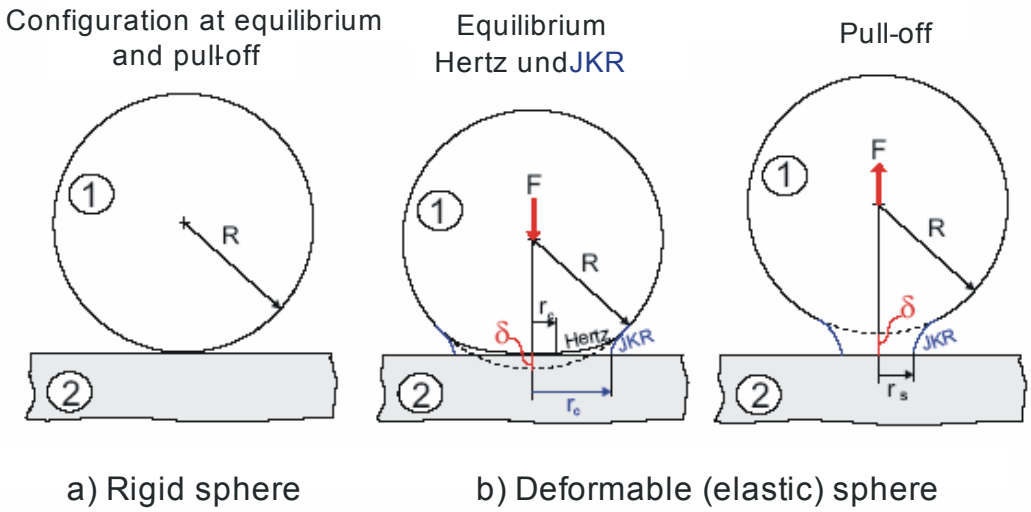

Fig. 3.4: a) Rigid sphere on rigid surface; b) deformable (elastic) sphere on rigid surface in the absence (Hertz) and presence (JKR) of adhesion; Pull-off: elastic adhering sphere about to separate spontaneously from adhesive contact (adopted from Israelachvili [1]).

The JKR-DMT transition using a Dugdale potential – Maugis model

In 1992, Maugis [76] verified that the JKR and DMT were actually limiting cases of a more general theory that can be applied for the entire range of materials parameters. Within his work, Maugis proposed the most complete and accurate theory. This theory applies to all materials, from large rigid spheres with high surface energies to small compliant bodies with low surface energies [55]. Maugis describes attractive forces between two contacting spheres with a Dugdale potential (Fig. 3.5)

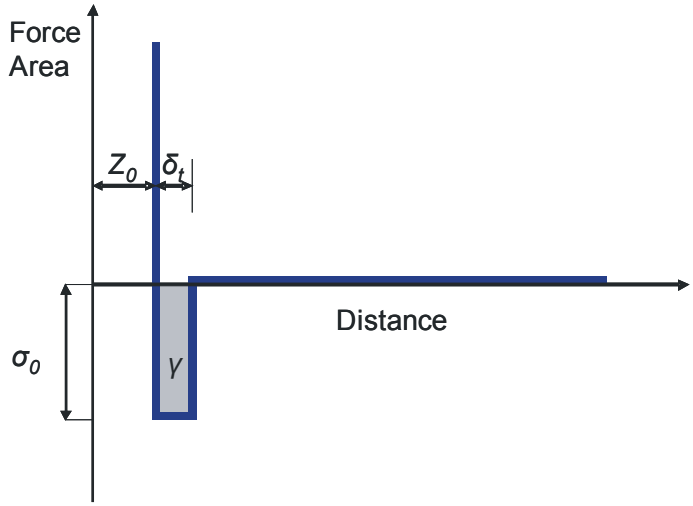

Fig. 3.5: The force-distance relation for the Dugdale model by Maugis [76].

A constant adhesive stress (force per unit area) σ_0 acts between the surfaces over a range δ_t. At greater separations, the attractive force is zero. The work of adhesion is thus [77]:

$$\gamma = \sigma_0 \times \delta_t \qquad \text{Eq. 42}$$

The so-called Maugis parameter, that is dimensionless, describes the full range of material properties and is defined as:

$$\lambda = 2\sigma_0 \left(\frac{R}{\pi \gamma K^2} \right)^{\frac{1}{3}} \qquad \text{Eq. 43}$$

or

$$\lambda = \frac{2.06}{Z_0}\sqrt{\frac{RW^2}{\pi K_2}} \qquad \text{Eq. 44}$$

in which Z_0 is again typical atomic dimension.

Maugis demonstrated that when λ increases from zero to infinity there is a continuous transition from the DMT approximation to the JKR approximation. If $\lambda \geq 5$, the JKR model applies and if $\lambda \leq 0.1$, the DMT model applies. Values between 0.1 and 5 correspond to the 'transition regime' between JKR and DMT models. This is depicted in Fig. 3.6.

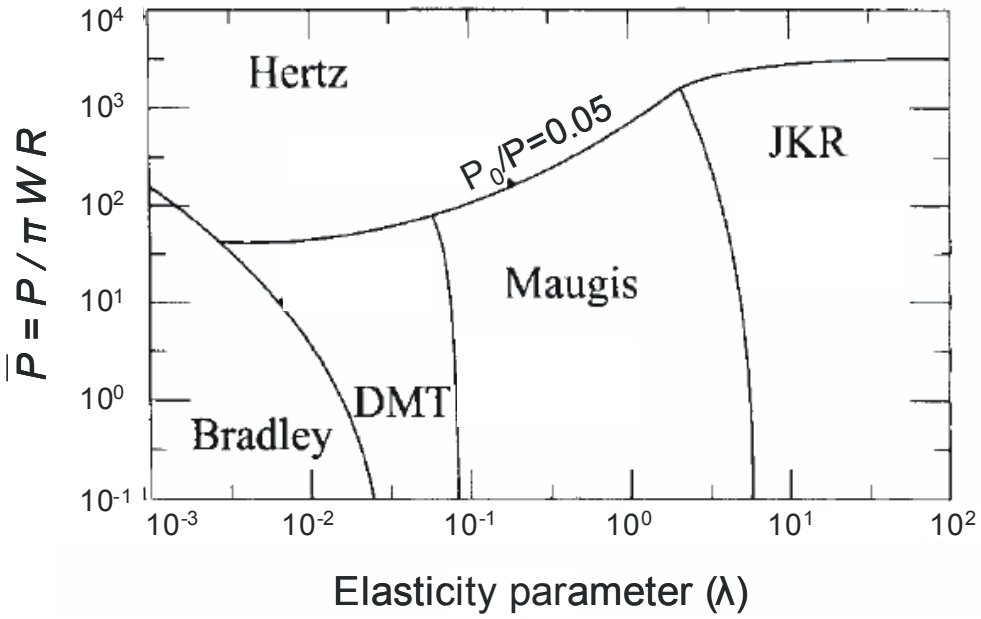

Fig. 3.6: Map of behaviour of bodies in different contact models adopted from Johnson [78] and Cappella [79].

3.5 Particle – surface coupling

Within this work, the particle-surface interaction was measured via a quartz crystal microbalance system. Therefore the above models have to be applied in this specific system utilized to study the contact mechanics between a polymeric film and solid particles.

The QCM has already been applied to study individual macroscopic contacts [30,80,81] and ensembles of small particles [82-84]. These experiments showed that the resonance frequency often increases when physically adhering particles are placed on a QCM [30]. In order to understand this increase, the particle-resonator system has been modelled as a pair of coupled resonators [30,83].

The use of the QCM for contact mechanics has been pioneered by Dybwad [30]. Dybwad placed a sphere onto a quartz resonator and found an increase in frequency. A positive frequency shift is incompatible with both the Sauerbrey equation and the Kanazawa equation, with the first applying to thin rigid films [43] and the second to semi-infinite viscoelastic media [48]. Even viscoelastic films usually lead to negative frequency shifts. Within all these models the effective mass of the resonator increases, thereby slowing down its movement. It is not directly comprehensible, how added mass should speed up the oscillation.

Dybwad [30] explains this increase by the fact that the sphere rests in place in the laboratory frame due to inertia. If the sphere is connected to the crystal via a small bridge (a "point contact"), the forces exerted by the crystal do not lead to an actual movement of the sphere in space, due to the inertial mass of the sphere that cannot follow the fast oscillation [33, 85] The positive frequency shifts occur when the crystal is put into contact with a sufficiently large sphere. This is due to the fact that the effective stiffness of the resonator is responsible for the positive frequency shift, rather than the increase of the system mass. However, since the sphere is connected to the crystal, it does exert a restoring force if the crystal is tangentially displaced. This restoring force adds to the internal stiffness of the crystal and thereby speeds up the oscillation. More importantly, Dybwad pointed out that the frequency shift can be exploited to measure the strength of the contact between the sphere and the quartz plate.

In his investigation, Dybwad has quantified the described behavior of the studied systems using the above considerations. According to his model, the sphere in contact with the surface forms a second resonator with its own resonance frequency, ω_s. The sketch at the

top of Fig. 3.7 shows the geometry and a mechanical representation. For a small mass tightly attached to the crystal, ω_s is much larger than the resonance frequency of the crystal, ω. These frequencies are coupled and this leads to the complication of the system response. As an example of this situation one can take the individual molecules physisorbed to the crystal surface. The Sauerbrey equation is recovered from the coupled-resonance model, when taking $\omega_s \gg \omega$. This situation is termed "inertial loading" in Fig. 3.7. Δf is negative as long as the adsorbed objects are small enough. However, for large (micrometer-sized) spheres attached to the crystal via weak bridges, ω_s, may be smaller than ω. In this limit, one arrives at a positive Δf, proportional to the stiffness of the contact and independent of the sphere's mass. This situation is termed "elastic loading" as depicted in Fig. 3.7. The sphere and the contact between the sphere and the surface constitute a resonating system of their own. In the mechanical representation, the crystal and the sample are modeled as coupled resonators with two resonance frequencies $\omega_p = (\kappa_p/m_p)^{1/2}$ (crystal) and $\omega_s = (\kappa_s/m_s)^{1/2}$ (sphere). The frequency shift, of the composite resonator relative to the unloaded crystal, depends on whether ω_s is higher or lower than ω. The resulting resonance frequency is high for small particles tightly attached to the crystal, which leads to Sauerbrey-type behavior ("inertial loading"). For small crystal resonance frequencies, the sphere remains immobile in space due to inertia, but the frequency shift exerts restoring the stiffness of the composite resonator ("elastic loading").

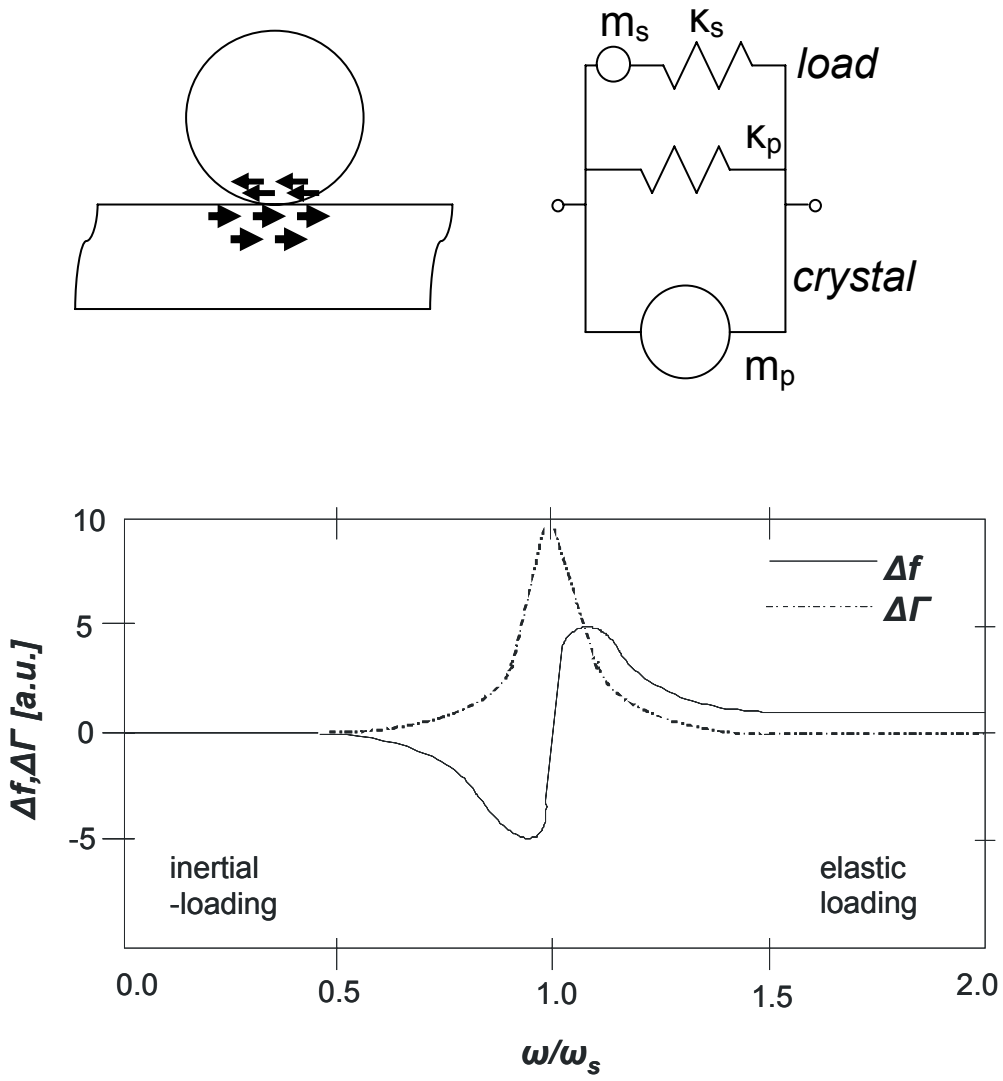

Fig. 3.7: (Left) Schematic representation of a sphere adsorbed to the surface of a quartz crystal microbalance. The sphere and the contact between the sphere and the surface constitute a resonating system of their own. (Right) mechanical representation, the crystal and the sample form a system coupled resonators with two resonance frequencies $\omega_p = (\kappa_p/m_p)^{1/2}$ (crystal) and $\omega_s = (\kappa_s/m_s)^{1/2}$ (sphere). The frequency shift of the composite resonator relative to the unloaded crystal depends on whether ω_s is higher or lower than ω. ω_p is high for small particles tightly attached to the crystal, which leads to Sauerbrey-type behavior ("inertial loading"). In the opposite limit, the sphere remains immobile in space due to inertia, but exerts a restoring the stiffness of the composite resonator ("elastic loading"). The bottom shows a plot of the solution of Eq. 45. Taken from Pomorska et al.[33]

3.5.1 Strong- and weak-coupling limit

The weak-coupling limit is of paramount importance in the context of this work. In the limit of weak-coupling, the frequency shift is positive and proportional to the stiffness of the contact. There is an intuitive explanation to the increase in frequency. One has to realize that the inertia clamps particles in space at high frequencies. A large sphere contacting the crystal across a narrow bridge cannot possibly follow the crystal's MHz oscillation. The sphere behaves like an immobile wall. Given that the contact exerts a restoring force onto the crystal, the overall stiffness of the composite resonator increases and the frequency increases accordingly. Only if the contact is stiff, that is if the inertial are much lower than the contact forces, does the sphere follow the crystal's motion. This is the strong-coupling limit. One can go from the weak-coupling limit to the strong-coupling limit by annealing an existing contact. This was done during this study by heating a glass-forming substrate to a temperature above the glass transition temperature T_g.

More quantitatively, the coupled-resonance model predicts:

$$\frac{\Delta f + i\Delta\Gamma}{f_F} = \frac{N_s m_s \omega}{\pi Z_q} \frac{(\omega_s^2 + i\omega\gamma)}{(\omega^2 - \omega_s^2 - i\omega\gamma)} = -\frac{N_s m_s \omega}{\pi Z_q} \frac{1}{1 - \dfrac{\omega^2}{\omega_s^2 + i\omega\gamma}} \approx \frac{-N_s m_s \omega}{\pi Z_q} \frac{1}{1 - \dfrac{\omega^2}{\omega_s^2}} \qquad \text{Eq. 45}$$

N_s is the number density of the spheres. The resonance frequency of the sphere-plate systems was also considered to be complex, where the imaginary part was termed $\omega\gamma$. The factor γ quantifies dissipative components of the sphere-plate interactions. The solution to Eq. 45 is shown in the lower part of the Fig. 3.7.

Further insight is obtained from Taylor expansions for large and small ω. For $\omega \ll \omega_s$, one finds:

$$\frac{\Delta f + i\Delta\Gamma}{f_F} \approx \frac{-N_s m_s \omega}{\pi Z_q} \frac{1}{1 - \dfrac{\omega^2}{\omega_s^2}} \approx \frac{-N_s m_s \omega}{\pi Z_q} \approx \frac{-2 f N_s m_s}{Z_q} \qquad \text{Eq. 46}$$

That is the Sauerbrey equation with $N_s m_s$ inserted for the mass per unit area. In the opposite limit of $\omega \gg \omega_s$, one finds:

$$\frac{\Delta f + i\Delta\Gamma}{f_F} \approx \frac{-N_s m_s \omega}{\pi Z_q} \frac{1}{1-\frac{\omega^2}{\omega_s^2}} \approx \frac{N_s m_s \omega_s^2}{\pi Z_q \omega} = \frac{1}{\pi Z_q} \frac{N_s \kappa_s}{\omega} \qquad \text{Eq. 47}$$

The last equation on the right-hand side made use of $\omega = (\kappa_s/m_s)^{1/2}$, where κ_s is the stiffness of the sphere-plate contact. Clearly, the frequency shift is positive, it is proportional to the stiffness of the contact, and it scales inversely with ω. Consequently, it scales inversely with the overtone order n. The equation above applies to the limit of purely elastic coupling.

When large diameter colloidal objects are adsorbed onto the surface of a quartz crystal microbalance, positive frequency shifts can be possibly observed. These most likely arise from point contacts between the adsorbate particles and the sensor surface.

With regard to the behaviour of spheres in contact, there are two well-characterized limits. If the spheres are tightly coupled to the crystal, they behave in essentially the same way as a film. For planar films, mass increase and a shift of the resonance frequency Δf are related by the Sauerbrey equation (as given in chapter 2.2.1) [43]:

$$\frac{\Delta f}{f_0} = -\frac{m_f}{\rho_q h_q} \qquad \text{Eq. 48}$$

here, m_f is the mass per unit area of the film, $\rho_q = 2650$ kg/m^3 is the density of quartz, h_q is the thickness of the crystal, and f_0 is the resonance frequency in the unperturbed state. The frequency shift is negative because the mass of the composite resonator increases. When small, monodisperse particles are placed on top of the QCM and are tightly attached one expects a frequency shift of:

$$\frac{\Delta f}{f_0} = -\frac{Nm}{A_q \rho_q h_q} \qquad \text{Eq. 49}$$

here, N is the number of particles on the active area A_q of the crystal and m is the mass of each particle. If the particles are evenly spread across the surface of the crystal, the size of the active area does not matter. It is the areal number density of spheres N/A_q, which determines Δf.

As derived by Johannsmann [86], the effective mass of the crystal is:

$$M = \frac{A_q \rho_q h_q}{2} \qquad \text{Eq. 50}$$

Note the factor of ½: M is *not* the total mass of the crystal.

The effective spring constant is:

$$K = \frac{A_Q G_Q n^2 \pi^2}{2 d_Q} \qquad \text{Eq. 51}$$

where G_Q is the crystal's shear modulus and n is the overtone order. The shift in the resonance frequency induced by N similar particles coupled with the same coupling constant k to the substrate is [30,83]:

$$\Delta f = N\left(\frac{1}{2\pi}\left[\frac{1}{2}\left(\frac{K}{M}+\frac{k}{M}+\frac{k}{m}\right) \pm \sqrt{\left(\frac{K}{M}+\frac{k}{M}+\frac{k}{m}\right)^2 - 4\frac{K}{M}\frac{k}{m}}\right]^{1/2} - f_0\right) \qquad \text{Eq. 52}$$

here, f_0 is the resonance frequency without particles. Eq. 52 differs from the form given by Dybwad [30] in the prefactor N. The original work was concerned with a single particle, while this work was carried out with ensembles. The factor N is extensively explained in the Chapter 3.6.2.

As discussed below, the solution for $k/m \approx K/M$ entails intricacies, which can be avoided by limiting the discussion to the cases, where the sphere is either tightly coupled to the crystal ($k/m >> K/M$, the minus sign applies before the square root in Eq. 52) or loosely

coupled to the crystal ($k/m << K/M$, corresponding to the plus sign before the square root). The tight-coupling limit basically is equivalent to the Sauerbrey regime. Δf is negative and proportional to the areal mass density Nm/A_Q (Eq. 49). The particles move with the crystal and increase its mass.

Weak coupling is less well understood. For fixed values of M, K, and m, the resonance frequency first increases weakly with increasing k due to the additional effective spring. When the coupling constant approaches the resonance condition, $k \to 4\pi^2 f_0^2 m$, the frequency increases steeply. For the example of a QCM with a fundamental resonance frequency at 6 MHz this is shown in Fig. 3.8. In this regime, the data have to be analyzed with care because both solutions of Eq. 52 may be visible in an experiment. However, for a large bandwidth, they may or may not be resolved. What appears as a broad resonance in the experiment may actually be a superposition of two peaks. At $k >> m\,(2\pi f_0)^2$ the minus sign in Eq. 52 applies and the frequency shift turns negative. This is the "strong-coupling regime". When further increasing k, the negative frequency shift decreases in magnitude to reach the value given by Eq. 49 for $k \to \infty$.

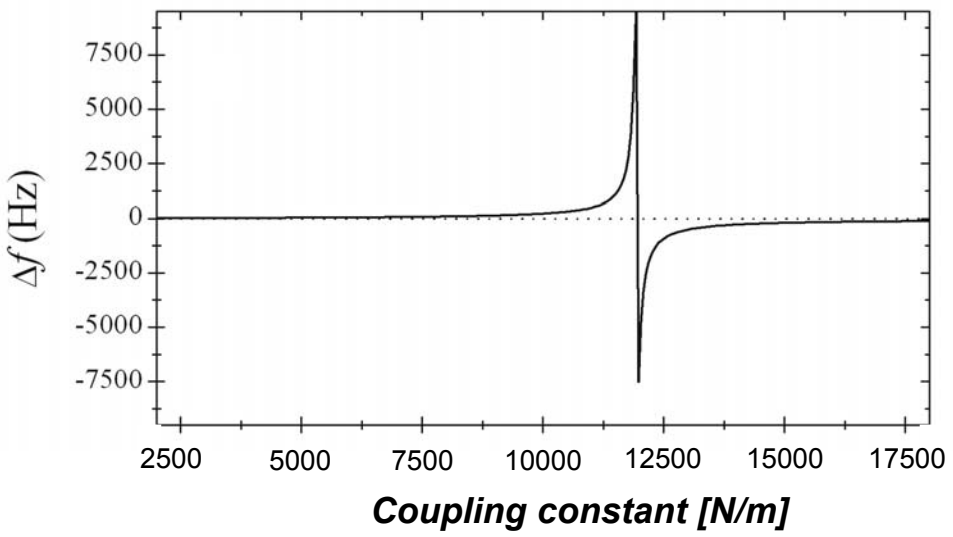

Fig. 3.8: Shift of the resonance frequency Δf (Eq. 52) for a QCM versus the coupling constant k. For the calculation was assumed that 100 particles of radius 10 µm and a mass of 8.4×10^{-12} kg are lying on the active area. The thickness of the quartz was assumed to be 0.434 mm and its mass 6×10^{-6} kg (corresponding to an active area of radius ≈4 mm), leading to a resonance frequency of f_0 = 6 MHz.

3.5.2 Extension of the Dybwad model to many spheres

As mentioned above, Dybwad's treatment applies to a single sphere. The extension of the model to many spheres results in a rather complicated set of equations. The difficulty goes back to the presence of more than one periodic solution to the equation of motion. Such a situation is well-known from the theory of the coupled pendulum. For the coupled pendulum there are two solutions, which are given by either a symmetric or an antisymmetric motion of the two arms. In the Dybwad model, there are two such modes as well. If the angular resonance frequency of the crystal, $(K/M)^{1/2}$ and the angular frequency of the coupled resonantor $(k/m)^{1/2}$ are the same, these are the symmetric (sphere moves in parallel to the crystal surface) and the antisymmetric (sphere moves antiparallel to the crystal surface) solutions. However, $(K/M)^{1/2}$ and $(k/m)^{1/2}$ are usually not the same. In most cases of practical interest one has either $k/m >> K/M$ or $k/m << K/M$. For such a situation, the modes are localized. One mode is a thickness-shear displacement of the crystal. The sphere closely follows the motion of the top surface. The other mode is given by an immobile crystal. The sphere moves relative to the top surface. Importantly, only the former mode is experimentally observed because only this mode induces a surface polarization inside the electrodes. It therefore suffices to investigate how the presence of the sphere shifts the frequency of this mode.

In the context of the QCM, a similar situation has been encountered before for the thickness-shear mode of a viscoelastic film resonance [87]. A thick viscoelastic film deposited on a quartz crystal has a resonance frequency of its own. The resonance condition is $d_f = \lambda/4$, with d_f the film thickness and λ the wavelength of sound. This "film resonance" constitutes a "coupled resonance" in much the same way as the sphere-plate contact. If the resonance frequency of the coupled resonance is the same as the resonance frequency of the resonator, one finds two modes. The existence of two such modes has also been observed experimentally.

The extension of the Dybwad model to numerous coupled spheres leads to cumbersome complications because every new sphere creates a new mode. As in vibrational spectroscopy, the number of modes increases with number of coupled particles. It has to be reminded that, the presence of more than one periodic solution to the force balance equation is by no means an artefact, it is rather an observed phenomenon. Simplification is possible by limiting one's attention to cases, where the frequencies of the coupled resonances are either much larger or

much smaller than the frequency of the resonator (weak-coupling limit and strong-coupling limit). Then all modes are localized and it suffices to consider the experimentally observable mode only.

There is a formalism adapted to this situation describe with the term "small load approximation", SLA, as given by Eggers et al. [81] and Johansmann et al. [88,89]. Other authors, e.g. Lucklum et al. use the word "surface impedance concept" [90]. One can show that the frequency shift of the crystal is given by [91]:

$$\frac{\Delta f + \mathrm{i}\Delta\Gamma}{f_F} \approx \frac{\mathrm{i}}{\pi}\frac{Z_L}{Z_q} = \frac{\mathrm{i}}{\pi Z_q}\left\langle\frac{\sigma}{\dot{u}}\right\rangle_{area} \qquad \text{Eq. 53}$$

$Z_L = \sigma / \dot{u}$ is the "load impedance", σ is the tangential stress at the crystal surface, $\dot{u}$ is the lateral speed at the crystal surface and angle brackets (<>) denote an average. The "load" here may consist of any object perturbing the crystal's motion. Well-known loads are the thin film in the Sauerbrey sense and the viscous liquid as described by Borovikow [66] and Kanazawa [67]. Other types of loads might be layers of biological cells, adsorbed vesicles, a sand pile, froth, or liquid droplets. Any type of load can be predicted and modelled within the small load approximation, provided that the stress induced at the crystal surface, σ is known. Again, the SLA requires that the stress obeys the relation for small loads, $\langle\sigma\rangle \propto Z_q \dot{u}$. A sphere-plate contact is such a load except for the situation when $k/m \approx K/M$. Within the small load approximation, N identical spheres behave similar to a single sphere. The presence of N spheres just amounts to a prefactor of N on the right-hand-side of Eq. 54.

If the sample consists of small spheres, the shifts of frequency and bandwidth are [84]:

$$\frac{\Delta f + \mathrm{i}\Delta\Gamma}{f_F} \approx -\frac{N}{A_Q}\frac{m\omega}{\pi Z_q}\frac{1}{1-\dfrac{\omega^2}{\omega_S^2 + \mathrm{i}\omega\gamma}} \qquad \text{Eq. 54}$$

with the angular resonance frequency of a particle $\omega_S^2 = k/m$. The force constant providing for the link between the sphere and the sensor surface was considered to be complex, that is, k was replaced by $k + i\omega m\gamma$, with γ as a damping coefficient.

There are two benefits from the use of the small load approximation. Firstly, Eq. 54 is simpler than Eq. 52. It avoids the two solutions. Also, the strong-coupling (Sauerbrey) limit and the weak-coupling limit can be derived simply by using $\omega_S >> \omega_0$ (Sauerbrey limit) and $\omega_S << \omega_0$ (weak-coupling limit) [92]. Second, Eq. 54 encompasses dissipative processes, which lead to an increase in bandwidth. Even though Eq. 54 is algebraically distinct from Eq. 52 it leads to a rather similar phenomenology.

In the next step derivation of the Sauerbrey limit and the elastic loading limit from Eq. 52 is presented. For notational brevity, the derivation for a single particle (N = 1) is written down. The derivation for many particles is recovered by replacing m with Nm and k with Nk. Firstly the Sauerbrey limit is derived, which is found for stiff contacts ($k \to \infty$):

$$
\begin{aligned}
2\omega_r^2 &= \left(\frac{K}{M}+\frac{k}{M}+\frac{k}{m}\right)-\sqrt{\left(\frac{K}{M}+\frac{k}{M}+\frac{k}{m}\right)^2-4\frac{K}{M}\frac{k}{m}} \\
&= \frac{K}{M}+\frac{k(M+m)}{Mm}-\sqrt{\left(\frac{K}{M}+\frac{k(M+m)}{Mm}\right)^2-4\frac{K}{M}\frac{k}{m}} \\
&= \frac{K}{M}+\frac{kM_{tot}}{Mm}-\sqrt{\frac{K^2}{M^2}+2\frac{K}{M}\frac{kM_{tot}}{Mm}+\left(\frac{kM_{tot}}{Mm}\right)^2-4\frac{K}{M}\frac{k}{m}} \\
&= \frac{K}{M}+\frac{kM_{tot}}{Mm}-\frac{kM_{tot}}{Mm}\sqrt{2\frac{K}{M}\left(\frac{kM_{tot}}{Mm}\right)^{-1}+\frac{K^2}{M^2}\left(\frac{kM_{tot}}{Mm}\right)^{-2}+1-4\frac{K}{M}\frac{k}{m}\left(\frac{kM_{tot}}{Mm}\right)^{-2}} \\
&\approx \frac{K}{M}+\frac{kM_{tot}}{Mm}-\frac{kM_{tot}}{Mm}\left(1+\frac{K}{M}\left(\frac{kM_{tot}}{Mm}\right)^{-1}+\frac{1}{2}\frac{K^2}{M^2}\left(\frac{kM_{tot}}{Mm}\right)^{-2}-2\frac{K}{M}\frac{k}{m}\left(\frac{kM_{tot}}{Mm}\right)^{-2}\right) \\
&= \frac{K}{M}+\frac{kM_{tot}}{Mm}-\frac{kM_{tot}}{Mm}-\frac{K}{M}-\frac{1}{2}\frac{K^2}{M^2}\left(\frac{kM_{tot}}{Mm}\right)^{-1}+2\frac{K}{M}\frac{k}{m}\left(\frac{kM_{tot}}{Mm}\right)^{-1} \\
&= -\frac{1}{2}\frac{K^2}{M^2}\frac{Mm}{kM_{tot}}+2\frac{K}{M}\frac{k}{m}\frac{Mm}{kM_{tot}}=\left(-\frac{1}{2}\frac{K^2}{M^2}+2\frac{K}{M}\frac{k}{m}\right)\frac{Mm}{kM_{tot}} \\
&\approx 2\frac{K}{M}\frac{M}{M+m}
\end{aligned}
\qquad \text{Eq. 55}
$$

For the calculation above the following approximations were used:

In line 3: $M+m = M_{tot}$

In line 5: $\sqrt{1+\varepsilon} \approx 1+\varepsilon/2$

In line 8: $k \to \infty$

In the following, $\omega_0^2 = K/M$, $\Delta\omega << \omega$, and $1/(1+\varepsilon) \approx 1-\varepsilon$:

$$2\omega_0^2 + 4\omega_0\Delta\omega + 2\Delta\omega^2 = 2\omega_0^2 \frac{M}{M+m} = 2\omega_0^2 \frac{1}{1+m/M}$$

$$2\omega_0^2 + 2\omega_0\Delta\omega \approx \omega_0^2\left(1-\frac{m}{M}\right)$$

$$2\frac{\Delta\omega}{\omega_0} = -\frac{m}{M} = -\frac{2}{A_Q\rho_Q d_q}m \qquad \text{Eq. 56}$$

$$\frac{\Delta\omega}{\omega_0} = \frac{\Delta f}{f} \approx -\frac{m}{A_Q\rho_Q d_q}$$

In line 11: $M = A_Q\rho_Q d_Q/2$. Again, note the factor ½.

One has $\rho_Q d_Q = Z_q/(2f_F)$, with Z_q the acoustic impedance of AT-cut quartz and f_F the frequency of the fundamental.

The elastic coupling limit is found for the opposite limit of $k \to 0$:

$$2\omega_r^2 = \frac{K}{M} + \frac{kM_{tot}}{Mm} + \sqrt{\frac{K^2}{M^2} + 2\frac{K}{M}\frac{kM_{tot}}{Mm} + \left(\frac{kM_{tot}}{Mm}\right)^2 - 4\frac{K}{M}\frac{k}{m}}$$

$$= \frac{K}{M} + \frac{kM_{tot}}{Mm} + \frac{K}{M}\sqrt{1 + 2\left(\frac{K}{M}\right)^{-1}\frac{kM_{tot}}{Mm} + \left(\frac{K}{M}\right)^{-2}\left(\frac{kM_{tot}}{Mm}\right)^2 - 4\left(\frac{K}{M}\right)^{-1}\frac{k}{m}}$$

$$\approx \frac{K}{M} + \frac{kM_{tot}}{Mm} + \frac{K}{M}\left(1 + \left(\frac{K}{M}\right)^{-1}\frac{kM_{tot}}{Mm} + \frac{1}{2}\left(\frac{K}{M}\right)^{-2}\left(\frac{kM_{tot}}{Mm}\right)^2 - 2\left(\frac{K}{M}\right)^{-1}\frac{k}{m}\right)$$

$$= 2\frac{K}{M} + \frac{kM_{tot}}{Mm} + \frac{kM_{tot}}{Mm} - 2\frac{k}{m}$$

$$2\omega_0^2 + 4\omega_0\Delta\omega + 2\Delta\omega^2 = 2\omega_0^2 + 2\frac{kM_{tot}}{Mm} - 2\frac{k}{m}$$

$$\omega_0^2 + 2\omega_0\Delta\omega \approx \omega_0^2 + \frac{k}{m}\left(\frac{M+m}{M} - 1\right) = \omega_0^2 + \frac{k}{M}$$

$$\Delta\omega = \frac{1}{\omega_0}\frac{k}{2M} = \frac{1}{\omega_0}\frac{k}{A_Q\rho_Q d_Q}$$

$$\Delta f \approx \frac{1}{2\pi}\frac{2f_F}{Z_q}\frac{k}{\omega_0} \qquad \text{Eq. 57}$$

$$\frac{\Delta f}{f_F} \approx \frac{1}{\pi Z_q}\frac{k}{\omega_0}$$

As shown above, Eq. 52 reduces to the Sauerbrey equation in the limit of tight contacts ($k \to \infty$). Furthermore, the "weak-coupling limit" is obtained in the limit $k \to 0$. The following relation holds:

$$\frac{\Delta f}{f_F} \approx \frac{1}{\pi Z_Q} \frac{N}{A_Q} \frac{k}{\omega} \qquad \text{Eq. 58}$$

$f_F = 2Z_Q/d_Q$ is the fundamental resonance frequency (f_F = 6 MHz for presented study). $Z_Q = 8.8\times10^6$ kg m^{-2}s^{-1} is the acoustic impedance of an AT-cut quartz. $\omega = 2\pi f$ is the angular frequency with f being the resonance frequency including a possible load. In principle, Eq. 58 is implicit in frequency, because f appears on both sides ($\Delta f = f - f_0$, $\omega = 2\pi f$, where f_0 is the resonance frequency of the unloaded state.). However, Δf is so small that one may safely replace $2\pi f$ by $2\pi f_0$, which turns Eq. 58 into an explicit equation.

3.5.3 Distribution of contact stiffness

It is realistic to assume that the coupling constants between particles and a surface are also widely distributed rather than having one precise value. For a semi-quantitative approach it can be assumed that the coupling constants are distributed like a normal Gaussian:

$$P(k) = \frac{1}{\Delta k\sqrt{2\pi}} \exp\left[-\left(\frac{\bar{k} - k}{\Delta k} \right)^2 \right] \qquad \text{Eq. 59}$$

here, $P(k)dk$ is the probability to find a coupling constant in the interval $k \ldots k + dk$. $\bar{k}$ is the mean coupling constant and Δk characterizes the width of the distribution. As examples, Fig. 3.9 shows three distributions of coupling constants around the mean value of $\bar{k} = 11938$ N/m for Δk = 1000, 2000, and 3000 N/m. This particular value of $\bar{k}$ was chosen because with $m = 8.4 \times 10^{-12}$ kg it leads to a resonance frequency of 6 MHz.

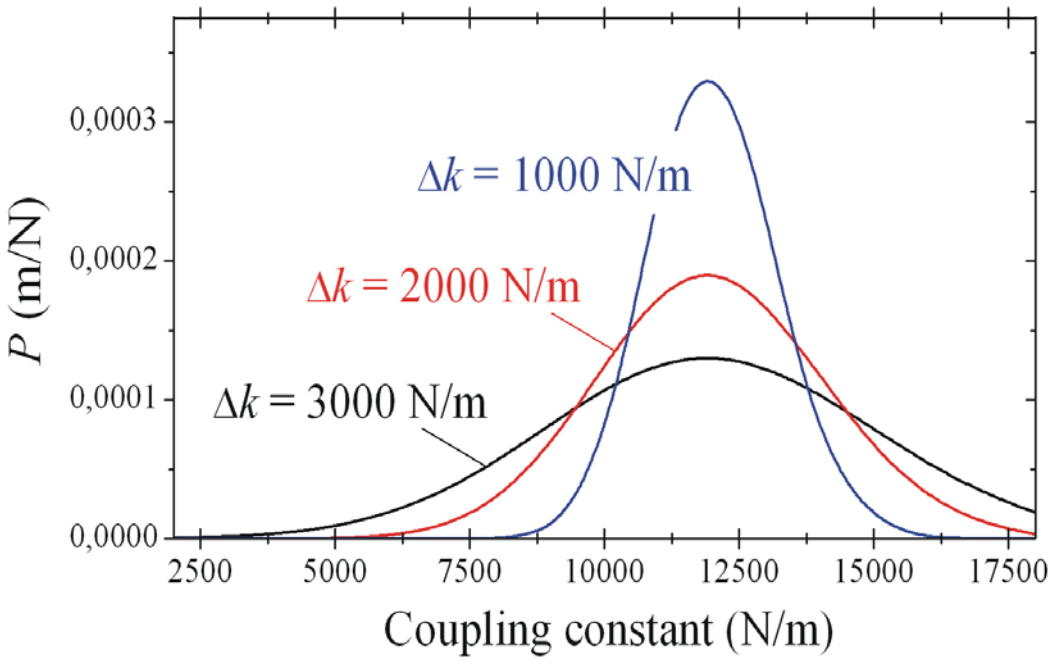

Fig. 3.9: Gaussian distributions of coupling constants according to Eq. 59 for three distributions with Δk = 1000, 2000, and 3000 N/m centred around $\bar{k} = 11938$ N/m.

A question can be raised on how does the observed frequency shift depend on the mean coupling constant at a given variation Δk. In order to calculate the frequency shift, it is convoluted as given by Eq. 52 with the probability P:

$$\Delta f(\bar{k}) = \int_0^\infty P(k)\Delta f(k)\ \mathrm{d}k \qquad \text{Eq. 60}$$

It has to be noted that $\int_0^\infty P(k)dk = 1$. Three examples obtained with $\bar{k} = 11938$ N/m and Δk = 1000, 2000, and 3000 N/m are plotted in Fig. 3.10. For each curve three regimes can be distinguished. First, for the case of weak coupling, the frequency shift is positive and increases with increasing mean coupling constant. Within the second regime, the frequency shift decreases from its maximum positive value to its minimum negative value. This regime spans a larger and larger range on the $\bar{k}$ axis with increasing width of the Δk. At the same time, maximum and minimum get less and less pronounced with increasing Δk. Finally, the third regime that can be defined is the case for which after the minimum $\Delta f(\bar{k})$, the frequency shift is still negative but becomes smaller and smaller, approaching the value that corresponds to the strong-coupling regime.

The higher Δk is, the smoother the derived curves are. It has to be considered that the sharp positive and negative peaks in Eq. 52 are reduced by orders of magnitude.

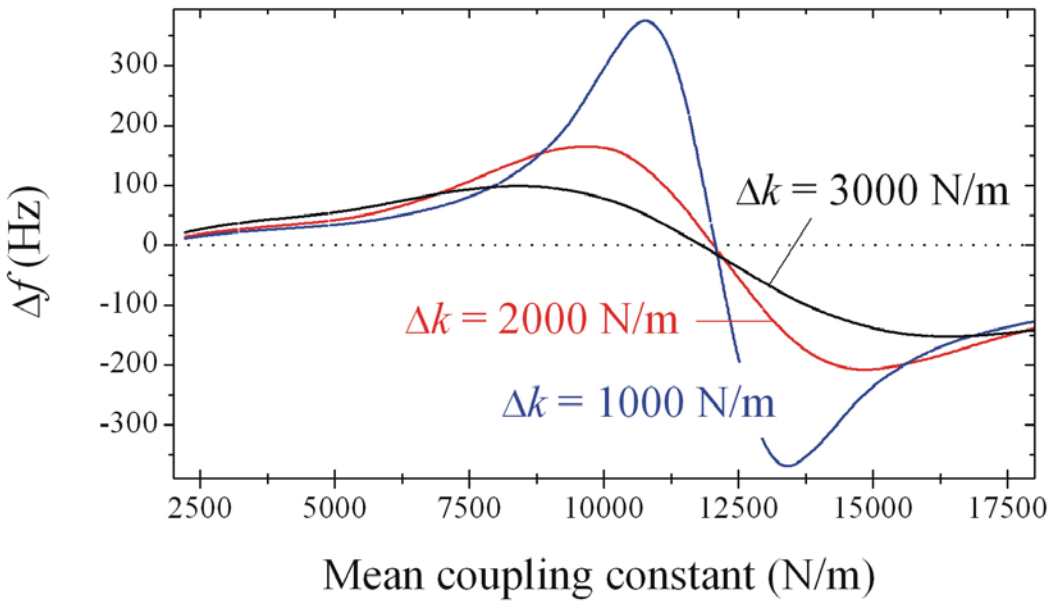

Fig. 3.10: Frequency shift versus the mean coupling constant $\bar{k}$ for the three Gaussian distributions with Δk = 1000, 2000, and 3000 N/m were calculated with Eq. 60.

3.5.4 Amplitude dependence of frequency and bandwidth

A particularly interesting feature in high-frequency contact mechanics is the case, for which nonlinear mechanical behaviour is experimentally observed. As discussed in the introduction, adhesion is usually quantified by the force (or, alternatively, the energy) needed to break a contact. Such a measurement occurs deep in the nonlinear regime of the stress-strain relation. The frequency shift as predicted by Eq. 53, on the other hand, refers to small stress and strain, that is, to the linear portion of the stress-strain curve. Measurements of Δf may occur at amplitudes of oscillation well below 0.1 nm and linear behaviour is indeed expected at this level.

At first glance, the measurement of an adhesion force and the measurement of shear stiffness in the linear regime have little to do with each other. However, in high frequency mechanics, linear behaviour and rupture are both limiting cases of a more general scenario termed “partial slip”. In the small-amplitude limit, partial slip approaches elastic behaviour, while at large amplitudes, partial slip turns into “gross slip”. “Gross slip” here denotes sliding,

which implies detachment, should there be a force pulling vertically onto the particle. Evidently, the transition between stick and slip always is continuous if one looks at very short time scales. However, the cascade of local rupture events usually is so fast that it can only be detected with equipment accessing short time scales such as the QCM.

Nonlinear phenomena can be accessed with the QCM, as long as the nonlinearities are small. As long as $\Delta f/f_0 << 1$, the QCM is only weakly perturbed and, in consequence, behaves only weakly nonlinear (if nonlinear at all). Central to the analysis is the assumption that the motion of the crystal stays close to sinusoidal, even in the presence of the load. The load changes the resonance frequency and the bandwidth, but it does not disrupt the periodic motion altogether. Going through details, one finds the relation [93,94]

$$\frac{\Delta f(u_0)}{f_F} = -\frac{1}{\pi A_Q Z_Q}\frac{2}{\omega u_0}\left\langle F_{\parallel}(t)\cos(\omega t)\right\rangle_{time}$$
$$\frac{\Delta \Gamma(u_0)}{f_F} = -\frac{1}{\pi A_Q Z_Q}\frac{2}{\omega u_0}\left\langle F_{\parallel}(t)\sin(\omega t)\right\rangle_{time} \qquad \text{Eq. 61}$$

$\Delta\Gamma$ is the change in the half width at half height ("bandwidth", for short). Angular brackets denote an average. u_0 is the amplitude of motion. $\omega = 2\pi f \approx 2\pi f_0$ is the angular frequency. $F_{\parallel}$ is the tangential force, where a restoring force has negative sign. Eq. 61 can be cast into complex form as:

$$\Delta f + i\Delta\Gamma = \frac{-2 f_F \left\langle F_{\parallel}\exp(i\omega t)\right\rangle_{time}}{(\pi A_Q Z_Q \omega u_0)} \qquad \text{Eq. 62}$$

In essence, the QCM operates like a lock-in amplifier. Δf and $\Delta\Gamma$ pick out the in-phase and the out-of-phase component of the force, respectively. If force and displacement are linearly related, $F_{\parallel} = ku = ku_0\cos(\omega t)$, Eq. 61 reduces to Eq. 53. Here, $u = u_0\cos(\omega t)$, where $u(t)$ is the lateral displacement between the centre of the sphere and the substrate. The frequency is independent of amplitude. Should, however, the force depend nonlinearly on displacement, the frequency will become amplitude-dependent. This situation is known from the theory of pendulum. Here, the restoring force is proportional to the sine of the angle rather

than the angle itself. For this reason, pendulum clocks run slower than expected if the amplitude of motion is too large.

Under certain conditions, the time average in Eq. 61 can be converted into a weighted average over the displacement between sphere and substrate, u. For Δf, one has

$$\begin{aligned}
\Delta f(u_0) &= -\frac{2f_F}{\pi A_q Z_q \omega_0 u_0}\left\langle F_{\parallel}(t)\cos(\omega t)\right\rangle_{time} \\
&= -\frac{1}{\pi^2 n A_q Z_q u_0}\frac{1}{T}\left(\int_0^{T/2} F_{\parallel\leftarrow}(t)\cos(\omega t)\,\mathrm{d}t \;+\int_{T/2}^{T} F_{\parallel\rightarrow}(t)\cos(\omega t)\,\mathrm{d}t\right) \\
&= -\frac{1}{\pi^2 n A_q Z_q u_0^2}\frac{1}{2\pi}\int_{-u_0}^{u_0}\left(F_{\parallel\leftarrow}(u,u_0)+F_{\parallel\rightarrow}(u,u_0)\right)\frac{u/u_0}{\sqrt{1-(u/u_0)^2}}\,\mathrm{d}u \\
&= -\frac{1}{\pi^3 n A_q Z_q u_0}\left\langle\left(F_{\parallel\leftarrow}(u,u_0)+F_{\parallel\rightarrow}(u,u_0)\right)\frac{u/u_0}{\sqrt{1-(u/u_0)^2}}\right\rangle_{displacement}
\end{aligned} \qquad \text{Eq. 63}$$

The frequency shift is a weighted average of the *sum* of $F_{||\leftarrow}$ and $F_{||\rightarrow}$. $F_{||\leftarrow}$ and $F_{||\rightarrow}$ are the forces experienced during decreasing and increasing displacement, respectively. It has to be noted that the motion occurs laterally. "Increasing displacement" is movement to the right. Evidently, symmetry requires $F_{\parallel\rightarrow}(-u) = -F_{\parallel\leftarrow}(-u)$. $T = 1/f$ is the time for one vibration. For the shift in bandwidth, $\Delta\Gamma$, the outcome of the calculation is:

$$\begin{aligned}
\Delta\Gamma(u_0) &= -\frac{2f_F}{\pi A_q Z_q \omega_0 u_0}\left\langle F_{\parallel}(t)\sin(\omega t)\right\rangle_{time} = -\frac{1}{\pi^2 n A_q Z_q u_0}\frac{1}{T}\int_0^{T} F_{\parallel}(t)\sin(\omega t)\,\mathrm{d}t \\
&= -\frac{1}{\pi^2 n A_q Z_q u_0}\frac{1}{T}\left[\int_1^{-1} F_{\parallel\leftarrow}(t)\,\mathrm{d}(\cos(\omega t)) + \int_{-1}^{1} F_{\parallel\rightarrow}(t)\,\mathrm{d}(\cos(\omega t))\right] \\
&= -\frac{1}{\pi^2 n A_q Z_q u_0^2}\int_{-u_0}^{u_0}\left[-F_{\parallel\leftarrow}(u,u_0)+F_{\parallel\rightarrow}(u,u_0)\right]\mathrm{d}u \\
&= \frac{-2}{\pi^2 n A_q Z_q u_0}\left\langle -F_{\parallel\leftarrow}(u,u_0)+F_{\parallel\rightarrow}(u,u_0)\right\rangle_{displacement}
\end{aligned} \qquad \text{Eq. 64}$$

The shift in bandwidth is an integral over the difference of $F_{||\leftarrow}$ and $F_{||\rightarrow}$, that is, $\Delta\Gamma$ is proportional to the area under the hysteresis loop (Fig. 3.11). In line 4, the relation $\cos(\omega t) = u/u_0$ was used. The minus sign before $F_{||\leftarrow}$ is a consequence of the exchange of integration boundaries.

If the forces are a function of displacement only, that is, $F_{||} = F_{||}(u)$, as opposed to $F_{||}(u,u_0)$, Eqs. 63 and 64 can be explicitly inverted. They turn into Volterra integral equations of the first kind. For these particular equations, analytical solutions are known [95]. A similar formalism has been used in atomic force microscopy, where the interaction forces between the tip and the substrate are derived from shifts of the resonance frequency of the cantilever [96-98]. However, in contact mechanics, the forces usually depend on position as well as amplitude and inversion of Eqs.63 and 64 requires further assumptions.

In the context of this work, the discussion is limited to a qualitative level, based on graphical representations of the force-displacement relation as shown in Fig. 3.11. Panel A shows the purely elastic case. There is no hysteresis and $\Delta\Gamma$ therefore vanishes. $F_{||\leftarrow}$ and $F_{||\rightarrow}$ are both equal to ku. Inserting the relation $F_{||\leftarrow} = F_{||\rightarrow} = ku$ into Eq. 63, one recovers Eq. 53. Panel B shows viscoelastic coupling, still obeying linear behaviour. There is a viscous component to the force, $F_{vis} = \xi\, \mathrm{d}u/\mathrm{d}t$ (ξ the drag coefficient) and the area under the curve is not zero. Also, since the viscous force depends on speed, the force at any given position depends on the amplitude of motion, u_0. Eq. 64 therefore cannot be directly inverted. In this particular case, one can relate the drag coefficient ξ to the bandwidth $\Delta\Gamma$ using viscoelastic behaviour as an input to the model. The result is $\Delta\Gamma = N f_F \xi \big/ \left(\pi A_Q Z_Q\right)$. For a proof, one can start from Eq. 53, replace Δf by $\Delta\Gamma$ and further replace k by $\omega\xi$.

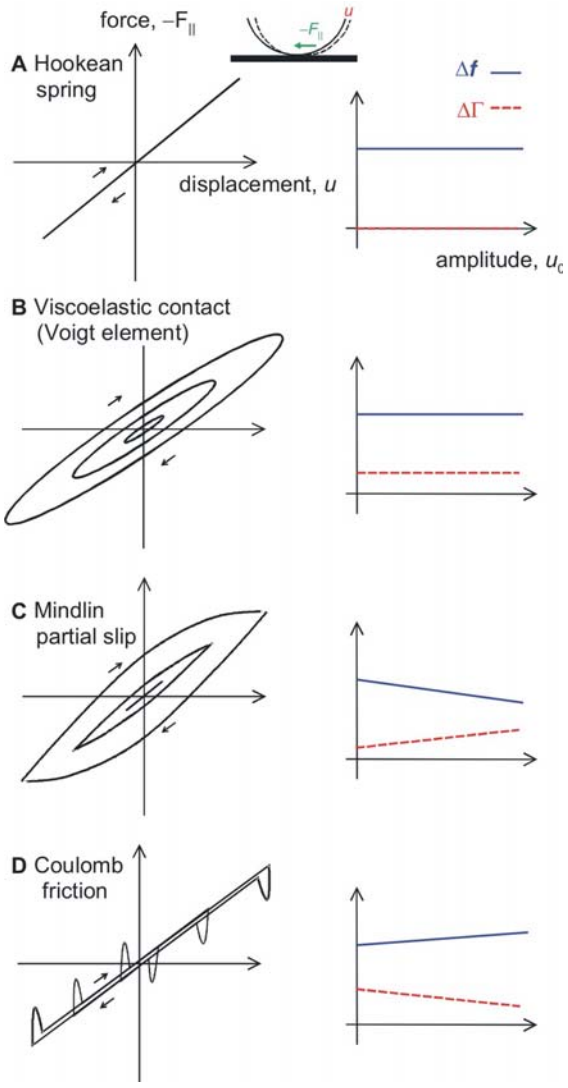

Fig. 3.11: Force–displacement relation (left) and resulting amplitude-frequency relations (right, blue, solid) and amplitude-bandwidth relations (right, red, dashed). For Mindlin-type partial slip (**C**), the area under the hysteresis loop increases more than quadratically with amplitude, and $\Delta\Gamma$ therefore increases with amplitude (Eq. 64). Coulomb friction (**D**) leads to a weaker-than-quadratic dependence of the area on amplitude. $\Delta\Gamma$ therefore *decreases* with amplitude.

Panel C in Fig. 3.11 shows the case of partial slip in the Mindlin sense [99,100]. In the context of QCM experiments, partial slip has been described in detail by Johannsmann [101]. When exerting a lateral force onto a sphere-plate contact, there is a stress singularity at the rim of the contact area. The high local stress leads to a ring-shaped area, inside which the surfaces slide relative to each other. With increasing lateral force, the sliding portion of the contact zone increases in size, until the entire contact finally slips ("gross slip"). The quantitative description of partial slip goes back to Mindlin [100]. He assumes that sliding sets in

once the local tangential stress exceeds the product of the normal stress times the static friction coefficient, μ_S. For oscillatory loading, the lateral displacement, $u(t)$, and the lateral force, $F_{||}(t)$, are related by [101]

$$\frac{F_{\|\leftarrow}(t)}{\mu_S F_\perp} = +\left[\frac{F_{\|0}}{\mu_S F_\perp} - 2 + \frac{1}{\sqrt{2}}\left(1 + \frac{2u(t)}{3\lambda_S} + \left(1 - \frac{F_{\|0}}{\mu_S F_\perp}\right)^{\frac{2}{3}}\right)^{\frac{3}{2}}\right]$$
$$\frac{F_{\|\rightarrow}(t)}{\mu_S F_\perp} = -\left[\frac{F_{\|0}}{\mu_S F_\perp} - 2 + \frac{1}{\sqrt{2}}\left(1 - \frac{2u(t)}{3\lambda_S} + \left(1 - \frac{F_{\|0}}{\mu_S F_\perp}\right)^{\frac{2}{3}}\right)^{\frac{3}{2}}\right] \qquad \text{Eq. 65}$$

$F_{||0}$ is the tangential force at $u = u_0$. One has $u_0 = 3/2 \cdot \left[1 - \lambda_S\left(1 - F_{\square 0}/\left(\mu_S F_\perp\right)\right)^{2/3}\right]$. Here, $F_\perp$ is the force load normal to the QCM surface. The characteristic length λ_S is given by $\lambda_S = \mu_S F_\perp / k$. It is termed "partial slip length" in analogy to the elastic length $\lambda_e = F_\perp / k$ used by Berthoud and Baumberger to describe multi-asperity contacts [102]. Inserting Eq. 65 into Eqs. 63 and 64 leads to a prediction for Δf and $\Delta\Gamma$. In the small amplitude limit ($u(t) << \lambda_S$) one finds [101]:

$$\frac{\Delta f}{f_F} \approx \frac{k}{\pi A_q Z_q \omega}\left(1 - \frac{1}{6}\frac{u_0}{\lambda_S}\right)$$
$$\frac{\Delta\Gamma}{f_F} \approx \frac{\Delta\Gamma_{offset}}{f_F} + \frac{k}{\pi A_q Z_q \omega}\frac{2}{9\pi}\frac{u_0}{\lambda_S} \qquad \text{Eq. 66}$$

$\Delta\Gamma_{offset}$ is an offset, induced by viscoelastic coupling and radiation of acoustic energy into the sphere. Using Eq. 66, the partial slip length can be determined from plots of Δf and $\Delta\Gamma$ versus amplitude. For known normal force, $F_\perp$, the partial slip length can be converted to an apparent μ_S. Again, this analysis requires an assumption, which is the Mindlin model.

The central feature of the Mindlin model (partial slip) occurs for non-Hertzian contacts, as well. For instance, partial slip also applies to multi-contact interfaces because those micro-

contacts, which are located at the rim of the macroscopic contact area, rupture first [103]. These contacts experience the largest lateral stress and the smallest vertical load.

In Fig. 3.11 D, another case is displayed, which is the Coulomb-type friction. In Coulomb friction, the force of dynamic friction is independent of speed. Around the turning points of the motion, dynamic friction turns into static friction, which is stronger than dynamic friction. The force-displacement relation is given by a bar-shaped area in the centre (dynamic friction) and spikes at the edges (static friction). Coulomb friction in its original meaning was developed for sliding contacts. However, the essential ingredients to Coulomb-type friction may apply for sphere-plate contacts under oscillatory load as well. A dynamic friction force independent of speed is found, whenever, firstly, the motion is impeded by barriers, and secondly, the energy needed to overcome a barrier is fully dissipated immediately after the respective barrier has been passed. A typical "barrier" here would be the arrest of crack propagation at pinning sites. Static friction in this context implies a peak in the pinning force at the turning points of motion. Such a peak is plausible, as well.

There is a characteristic qualitative difference between Mindlin-type microslip and Coulomb friction. This difference reflects the fundamental difference between conventional mechanics and granular mechanics. In Mindlin microslip, the area under the hysteresis loop increases with amplitude. In terms of material science, this is why railway tracks are made out of gravel. When a pile of gravel is loaded with some external object (such as a train) its ability to dissipate energy outperforms just about all other engineering materials. This happens because the integrated area of slipping contact keeps increasing with increasing load. Only after partial slip turns into "gross slip" is this situation reversed. Gross slip in the context of railway tracks implies large scale movement of the entire structure, which requires enormous forces.

The peculiar behaviour of "granular contacts" is evident in the QCM results. For Mindlin microslip in the small amplitude limit, the area under the hysteresis loop depends cubically on amplitude [99]. The dissipated energy becomes large because the sliding portion of the contact increases with amplitude. Dividing the dissipated energy by u_0^2 (Eq. 64) one finds that $\Delta\Gamma$ increases roughly linearly with amplitude. This situation is found in experiments after the contact is first established. For Coulomb-type friction, on the other hand, the size of the hysteresis loop scales either linearly with amplitude (dynamic friction) or does not depend on amplitude at all (static friction). In both cases, $\Delta\Gamma$ decreases with amplitude. In experiments, this situation is encountered after annealing (Fig. 5.5).

3.5.5 Lateral stiffness of multi-asperity contacts

Using the Hertzian contact theory one expects a lateral spring constant of a single contact of about [101]

$$k = G^* a$$
$$\frac{1}{G^*} = \frac{1}{8}\left(\frac{2-\nu_1}{G_1} + \frac{2-\nu_2}{G_2} \right) \qquad \text{Eq. 67}$$

Here, a is the radius of contact. The indices 1 and 2 label the two contacting materials, G^* is the effective shear modulus, G is the shear modulus, and ν is Poisson's number. It has to be noted that Eq. 67 assumes a semi-infinite substrate and neglects roughness. The contact radius, a, as predicted from Hertz theory is:

$$a = \sqrt[3]{F_\perp R / E^*}$$
$$\frac{1}{E^*} = \frac{3}{4}\left(\frac{1-\nu_1^2}{E_1} + \frac{1-\nu_2^2}{E_2} \right) \qquad \text{Eq. 68}$$

here $F_\perp$ is the adhesion force, E is the Youngs' modulus, and E^* is the reduced Youngs' modulus. Using $E = 2\,(1+\nu)\,G$ and $\nu \approx 1/3$, one finds that $E^* \approx 5/6\,G^*$.

There are two reasons why a multi-asperity contact between a sphere and plate would be stiffer under a shear load than a single contact. The first argument has to do with the fact that the vertical load carried by a contact scales as the cube of the contact radius, a^3, while the lateral spring constant scales as a (Eq. 67). A similar result has been found in bioadhesion. The phenomenon is termed contact splitting [104]. Here, the difference in scaling occurs between vertical load ($\sim a^3$) and rupture force ($\sim a$). Contact splitting is exploited by some animals in order to increase the dry adhesion between their feet and the object they need to stick to.

In order to bring the argument across, simplifying assumption have to be made: The contact is made across a finite number (N_c) of identical nanoscopic contacts; the contacts are

not elastically coupled to each other, all individual contacts behave according to Hertz theory, all have the same radius of curvature, $R_c \sim R\, N_c^{-1/2}$, they share the vertical load equally between them, and they all contribute equally to the lateral stiffness. Further, it has to be assumed $E^* \sim G^*$. The combination of Eq. 67 and 68 now reads:

$$k \sim N_c\, G^* a = N_c\, G^* \left(\frac{F_\perp R_c}{N_c G^*} \right)^{1/3} = N_c^{1/2} \left(G^* \right)^{2/3} \left(R F_\perp \right)^{1/3} \qquad \text{Eq. 69}$$

This scaling analysis predicts that the lateral contact stiffness increases with the number of contacts. Note however, that the contacts have to be elastically independent. The assumptions certainly are not fully correct for a contact between rough surfaces. Elastic coupling between the contacts, in particular may change the outcome of this calculation [105].

A second reason, why roughness may increase the lateral stiffness of a contact has to do with the distribution of loads. As the analysis by Mindlin shows, the distribution of local stress in the contact zone shows sharp peaks at the rim of the contact zone. When distributing the vertical load between numerous small nano-contacts, some of these nanocontacts will be situated further away from the centre than the rim of equivalent single-asperity contacts. Roughness "spreads out" the distribution of the load-carrying contacts. Since the local stress increases with distance from the centre, the more distant contacts do more efficiently support lateral stress than the central contacts. This contrasts to vertical load. The vertical load is strongest in the centre. The situation resembles beam bending, where hollow rods resist bending stronger than full rods of the same cross-sectional area. Moving the supporting material away from the neutral plane stiffens the respective element.

4. Materials and methods

4.1 Experimental setup

QCM.

Throughout this work, AT-cut quartz crystals with a fundamental resonance frequency of 6 MHz and a thickness of 0.27 mm were used (China National Scientific Instruments and Material Corp., Hangzhou, China). The blanks were optically polished and had a diameter of 25.4 mm. After cleaning in an ultrasonic ethanol bath, a 2 nm thick adhesive layer of chromium followed by a 100 nm thick gold layer with diameter of 10 mm was evaporated on the quartz surface. This gold electrode was electrically grounded during experiments. On the back side, a gold electrode of 7 mm diameter and 200 nm thickness was deposited (again with 2 nm of adhesive Cr layer) (Fig. 4.1). It was connected to a Network Analyzer (Agilent E5100A 10 kHz – 180 MHz). Outside the active area of about 7 mm diameter the oscillating amplitude decays exponentially as described in Chapter 2.1.4.

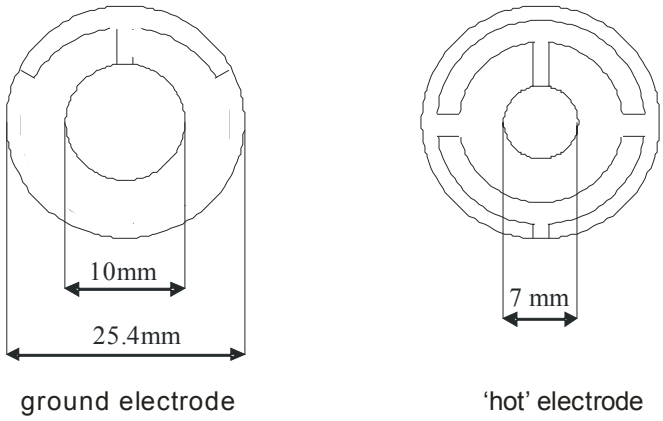

Fig. 4.1: Shape of the sputtered gold electrodes, 'active' electrode 200 nm Au, and ground electrode 100 nm Au, both on 2 nm Cr

Drive level [dBm]

The drive level of a crystal is a function of the reactance of the input and output capacitance of the inverter or active device and all other external components, including the crystal [31]. The drive level of a crystal is a measurement of the power dissipation experienced by a crystal in a given circuit. The drive level is expressed in milliwatts (mW) or microwatts (μW), where 0 dBm corresponds to 1mW of power. The frequency of quartz resonator depends on the drive level. At high amplitudes of oscillation, a slight elastic nonlinearity increases the apparent spring constant, thereby increasing the resonance frequency.

During this work the driving voltage provided by the Network Analyzer was adjusted in units of dBm. The recorded dBm were converted to Volts with the equation Power = $\text{Voltage}^2/Z_{el}$ with Z_{el} being the impedance of the cable (50Ω for BNC cables). For the scale, 0 dBm corresponds to about 223 mV_{rms}, which corresponds to 630 mV maximum amplitude (peak-to-peak).

A sinusoidal voltage of amplitude U_0 was applied. This results to an electrical power, which is calculated and expressed in dBm. This above mentioned voltage quantity corresponds to $dBm = 20 \cdot \log\left(U_0 / 0.317\text{V}\right)$. The excitation with this voltage is done with a specific frequency corresponding to an harmonic for the quartz. The 3rd harmonic at 18 MHz was recorded and used here (unless mentioned otherwise), because it was more stable than the 1st harmonic.

Video system

To reduce the influence of mechanical vibration, the whole setup was placed on an active vibrations-isolation table (Newport Corporation, Irvine, CA, USA). In order to determine the adhesion force between particles and surfaces, the QCM holder was turned upside down, facing downwards (Fig. 4.2). As a result, particles fell off as soon as the adhesion force was overcome by their weight and vibrational motion.

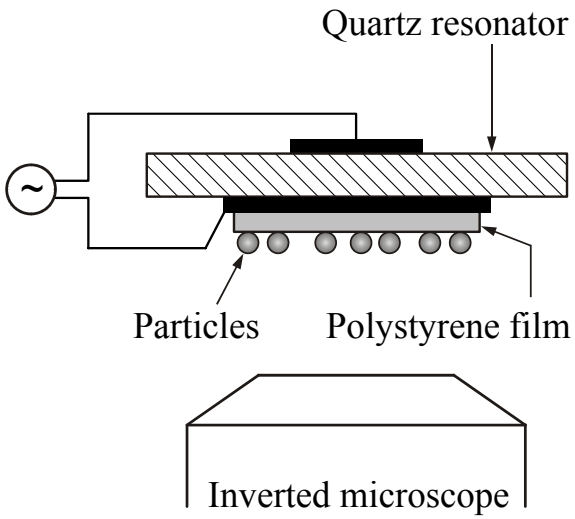

Fig. 4.2: Experimental setup for adhesion measurements with a quartz resonator.

A stereomicroscope (Leica MS 5) with a 1× objective and a five-step magnification changer (0.63×, 1.0×, 1.6×, 2.5×, 4.0×) was used. The upright microscope was altered to an inverted configuration. A digital camera (Watec WAT-202D) was connected to the system by means of a C-Mount-Adapter (0.63×). The QCM was illuminated with a fibre optic ring light source attached to the microscope. Magnifications of 0.63 and 1.6 were applied, showing a field of view of 1 cm and 0.4 cm respectively. With the higher magnifications the position of an individual particle was imaged. Three different behaviours were distinguished: 1) no movement of the particles, 2) lateral motion, and 3) particles fall-off.

4.2 Materials and sample preparation

Borosilicate glass particles

Spherical borosilicate glass particles (Duke Scientific Corporation, California, USA) having mean diameters of 5, 10, 15, and 20 ± 1 μm were used as received. Without taking the quartz out from the holder, the particles were deposited on the polymer surface. For this purpose, a thin metal-wire, washed before with THF and dried with nitrogen or left in a vacuum oven to dry, was used to pick-up several hundreds of the particles from the bulk. They were placed on the quartz surface by shaking. In order to deposit them in the center of the quartz, the particles were deposited through a 1 mm diameter hole of an aluminium film used to cover the holder. The smaller the particle-diameter was, the stronger the tendency of the particles to agglomerate. For the 5 μm particles agglomeration was unavoidable while for 20 μm particles practically no agglomeration was observed. The surface with deposited particles was imaged by video camera connected to the microscope. In Fig. 4.3 representative images of particles distribution on the quartz surface are shown. The images were analysed by Image Pro Plus software (Media Cybernetics, Inc. Silver Spring, MD, USA) to determine the number of the particles. The mean density of particles was 33200, 12900, 8700, 3200 particles per cm^2 for 5, 10, 15 and 20 μm particles, respectively. The microsphere density is roughly 2500 kg/m^3 (Duke Scientific Corporation data sheet).

Spin-coating

Spin-coating is widely used for producing thin layers, for example photoresist or dielectric coatings, in the manufacture of microprocessors [106]. In this method a small amount of a diluted polymer solution is pippetted onto a spinning quartz. Excessive solution is flung from the disc and the remaining layer thins as a result of centrifugal forces and evaporation. The solution leaves behind a uniform polymer layer. Daughton and Givens [107] have reported the final thickness to be independent of the volume of solution applied. Thickness of the layers increases with the concentration and decreases with rotational rate.

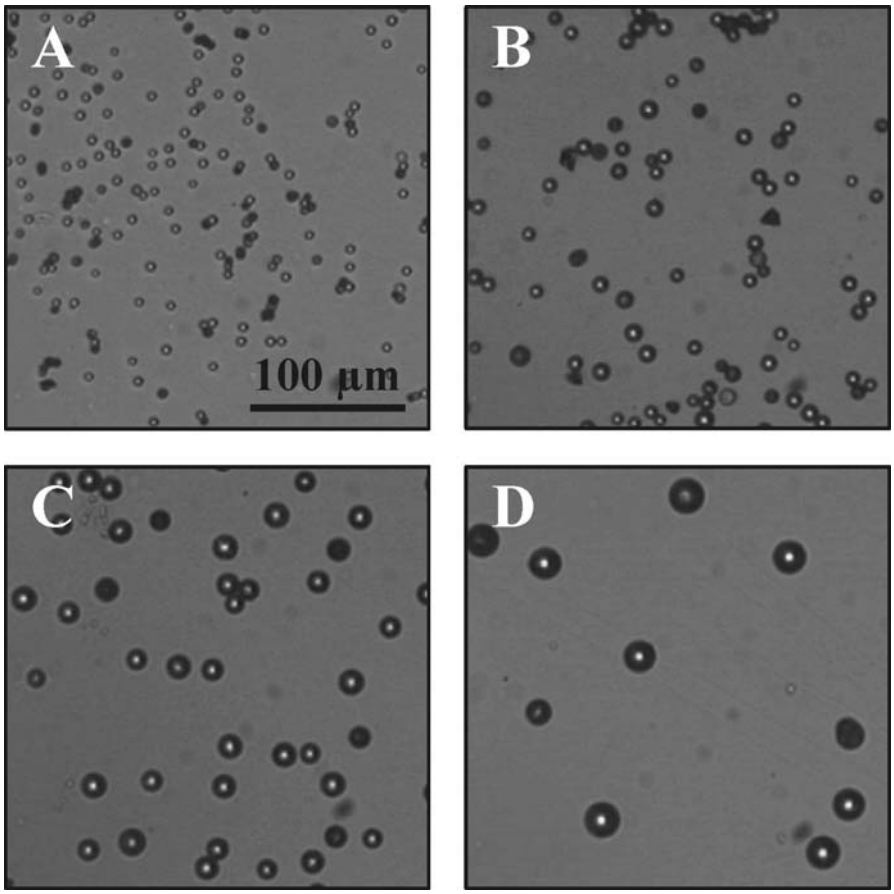

Fig. 4.3: Representative video images of 5 (A), 10 (B), 15 (C) and 20 µm (D) diameter glass particles on polystyrene films on a QCM.

Polystyrene films

Polystyrene (PS) with M_w = 11700 g/mol was dissolved in toluene (20 g/L). To remove any dust, the solution was filtered through Millipore filters of 0.2 µm pore size (Millex MILLIPORE, Syringe Driven Filter Unit, hydrophobic PTFE) before the polymer was spin coated onto gold electrode at 1600 rpm for 60 s. Afterwards, samples were annealed for 15 min at 150^{o}C in a preheated oven. After annealing, the quartz blank was left to cool down to room temperature. As expected, after depositing a PS film on the gold electrode the resonance frequency of the QCM decreased according to the mass density of the film. No significant dependence of the resonance frequency on the driving amplitude was observed up to amplitudes u_0 of 10 nm (Fig. 4.4). For amplitudes between 10 and 16 nm a slight increases of the resonance frequency was detected, which is small compared to the changes observed due to the addition of particles. This frequency increase can be identified with nonlinearities which occur at higher driving amplitudes. All experiments described, if not otherwise

mentioned, were performed at amplitudes < 10 nm, in order to eliminate the influence of nonlinearities. When applying small amplitudes (≤0.5 nm) the partial slip is of negligible influence. Furthermore loss of particles is also negligible, thus no frequency shift due to mass loss is expected. Spectra recorded at low amplitudes should therefore reflect only changes caused by different particle–bonding to the surface, as mentioned in Chapter 3.5.

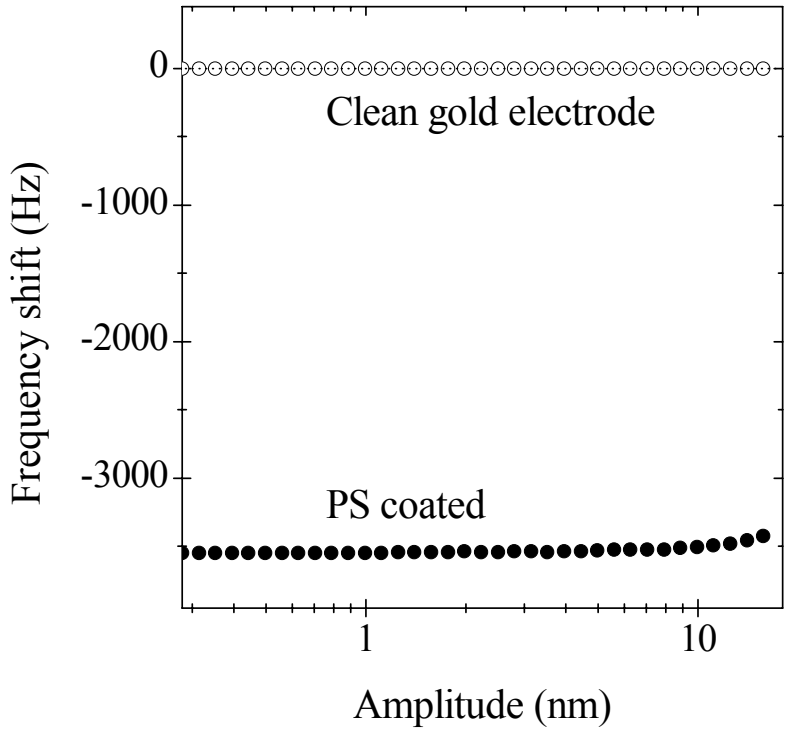

Fig. 4.4: Resonance frequency versus amplitude at an excitation frequency of 18 MHz before and after forming a polystyrene film of 157 nm thickness.

The film thickness was in the range of 100 – 180 nm as calculated from the QCM response with the Sauerbrey equation Eq. 18. For a quartz thickness of d_Q = 0.27 mm and quartz density ρ_Q = 2650 kg/m^3 the film thickness was calculated and compared to direct measurements. These were taken by utilizing ellipsometry (Ellipsometer EP^3 - SE, Nanofilm, Germany) in order to verify the QCM results. The deviation was found to be less than ~ 30 nm, which is an acceptable result and suggest a good agreement between the two methods (QCM vs. ellipsometry), considering the Sauerbrey model for QCM (described in Chapter 2.2.3).

Surface qualitiy.

The quality of the gold electrodes and the surface coating was checked by atomic force microscopy imaging in tapping mode. A detailed description of this specific methodology and procedure is given in Chapter 6.

5. Results and discussion

5.1 QCM oscillation amplitude

In order to calculate the amplitude of the quartz crystal resonator motion, u_0 (Fig. 5.1), the Eq. 5 derived by Johannsmann [36] was applied, for which the effective amplitude, u_0 is given by:

$$u_0 = \frac{4d_{26}}{\pi^2 n^2} Q U_0 \qquad \text{Eq. 70}$$

here, $d_{26} = 3.1\times10^{-12}$ m/V is piezoelectric strain coefficient, Q is the quality factor, n is the overtone order (in this case $n = 3$), and $U_0 = 0.317\times10^{(\mathrm{dBm}/20)}$ V is the driving voltage.
After spin coating the PS film on the electrode surface, the mean decrease of the amplitude is in the order of 4 nm.

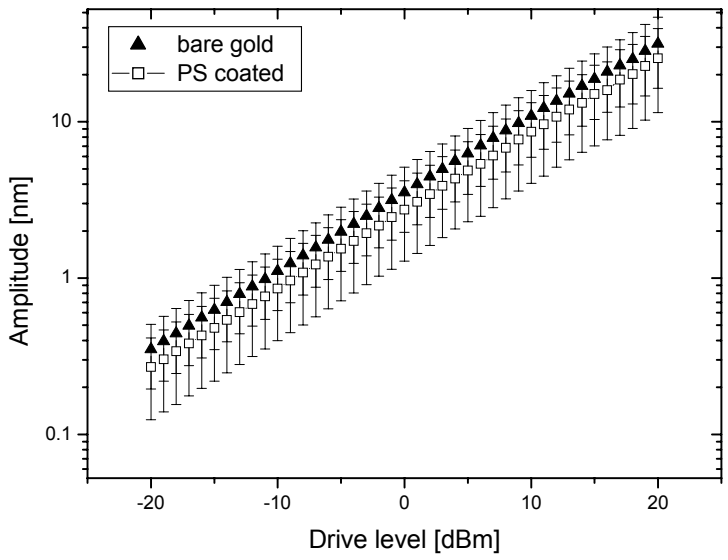

Fig. 5.1: Amplitude vs. drive level for clean gold electrode and PS coated gold electrode.

5.2 Critical amplitude for particle detachment

In order to study the interaction between quartz crystal and particles, experiments were performed over a wide amplitude range. Particle distribution on the surface, as well as possible particle-detachment during oscillation, was observed by video microscopy. This approach allowed to determine the amplitude value required to induce particle movement. More precisely, depending on the applied amplitude, one could clearly distinguish between three different behaviours: 1) no movement of the particles, 2) lateral motion (observed only before annealing) and 3) particles falling off. The specific amplitude value leading to particle detachment (3rd case) is defined here as the critical amplitude. Above this amplitude the mass of the system changes and influences the measured frequency response significantly. The experiments performed initially for studying the particle-surface coupling were done at amplitudes much smaller than the critical one, thus ensuring that no particle-detachment took place. In a different series of experiments, this specific critical amplitude for particle detachment was determined for each system. Furthermore, surface changes occurred during the particles movement were determined by AFM imaging and are described later in Chapter 6.

Critical amplitude before annealing of PS-film

The amplitude required for loosing the primary bonding between particles and surface for different quartz blanks was determined. The Fig. 5.2 shows results for different quartzes and different particles sizes before annealing, when determining the oscillation amplitude at which the first motion of particles occured. For very small particles (5 μm diameter), which fell off at lower amplitudes, the differences between different quartzes were not significant. The deviation of the critical amplitude was in the range of 1 nm (approximately 67% of the mean value). The mean value of the critical amplitude was 1.5 nm. For 10 μm the mean value was 3 nm, with a deviation ~ 2 nm (~ 67%). However, in the case of 15 μm diameter particles, the deviation between single quartzes was very high, ~16 nm (above 100% of mean value). As depicted in Fig. 5.2, for one quartz the particles fell off at an amplitude of approx. 4 nm, while in another case more than 20 nm amplitude had to be applied in order to simply move the particles on the surface. The mean value of the critical amplitude was 10 nm. Finally the mean value of the critical amplitude for 20 μm particles before annealing was 5 nm, with deviation ~ 2 nm.

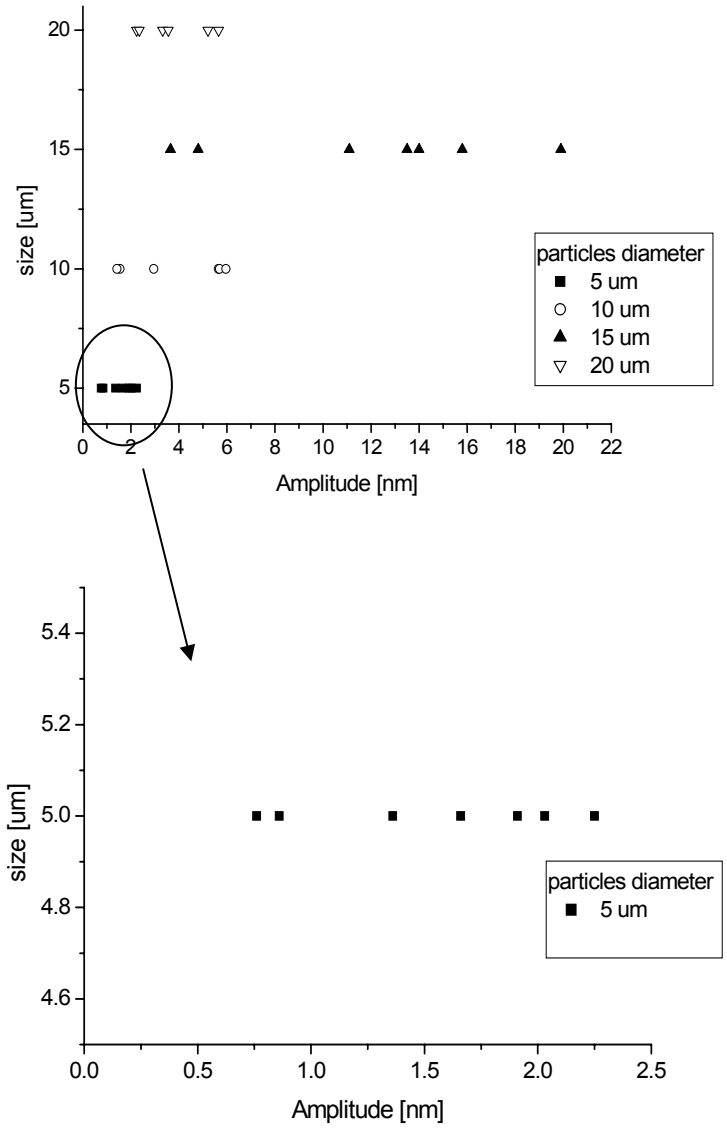

Fig. 5.2: Critical amplitude before annealing. Size of the particles vs. driving amplitude – breaking of primary bonding before annealing; Below, only the data for 5μm plotted for clarity.

Critical amplitude after annealing

After annealing at 150^0C for 15min, the trend of the amplitude at particle detachment did not change (see Fig. 5.3.). First the smallest particles were lost, i.e. 5 μm diameter by mean critical amplitude 0.6 nm (deviation ± 0.5 nm). For 10 μm particles the mean critical amplitude value was ~ 5 nm. The 15 μm particles started to move by 15 nm amplitude. For 10 and 15 μm particles the deviation in a range of 8 nm was measured. The broadest distribution of amplitudes after annealing was found for 20 μm particles, with values between 2 and 18 nm and a mean of 8 nm.

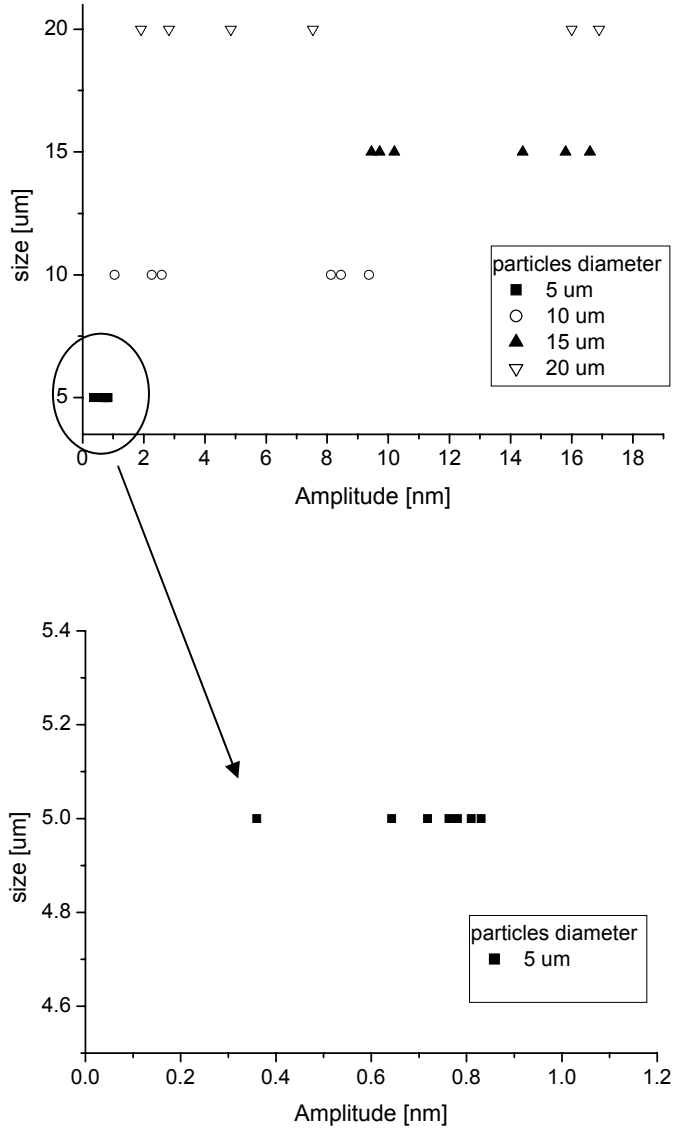

Fig. 5.3: Upper: Critical amplitude after annealing. Size of the particles vs. driving amplitude necessary to break the primary bonding after annealing; Lower: same data plotted at magnifified scale

When data before and after annealing are compared (Fig. 5.4.), it can be concluded that just for 5 μm particles after annealing, the necessary amplitude to loose the particles from the surface is lower than before. For the rest cases no such distinction can by made, thus the deviation of 5 μm is not considered statistically significant.

These deviations of the singe values determined for particle detachement in every experiment can be attributed to the different surface quality of each quartz-polymer film system used. Furthermore, as already mentioned, one has always to consider a distribution of the

particle/surface coupling intensity. A certain fraction of the particles is detached. This amount of detached particles depends on particle diameter and can be affected by the polymer film quality and homogeneity. Another explanation is that, before annealing (rough surface), the particle detaches when it meets a high resistance during its movement (as a ball rolling over a "bumpy" road). After annealing, the particle settles in a meniscus of the surface. The probability that it moves outside during its oscillatory movement is lower, however if this takes place, the particle will also detach as easily as before.

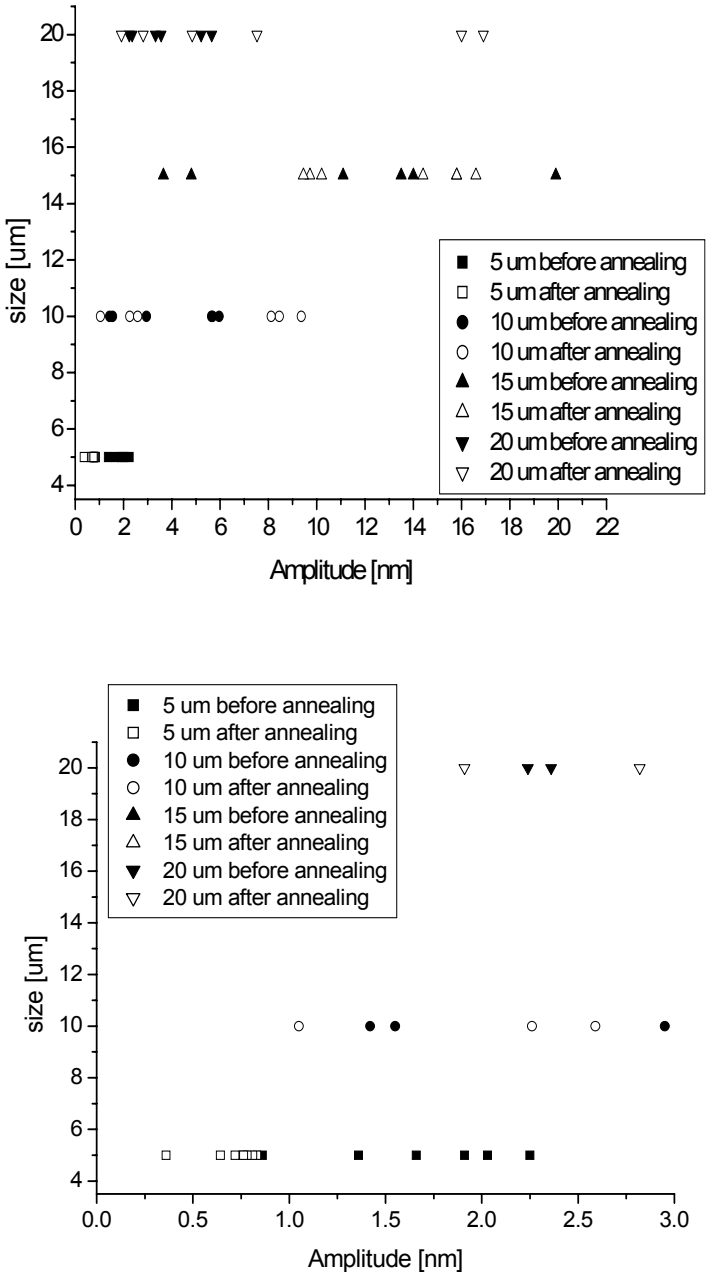

Fig. 5.4: Upper: Critical amplitude. Size of the particles vs. driving amplitude before and after annealing; Lower: same data plotted at magnified scale.

5.3 Contact between particles and polymer-film

To obtain more specific information on contact strength between particles and the PS surface, the following experimental procedure was used: as a first step, the quartz was characterized by a QCM frequency sweep directly after gold sputtering. In this way, the base line to compare the changes in measured resonance frequency and to estimate the film thickness was recorded. In a second step, a PS solution in toluene was prepared and the polymer film was spin coated onto the quartz surface. The samples were annealed for 15 min by 150^0 C, in a preheated oven. After annealing, the sample was cooled-down to room temperature. The data points for the bare PS film were recorded. In the following, all frequency shifts are referenced to the PS-coated crystals prior to the deposition of spheres. In the next step, particles were placed on the top of the quartz without taking it out from the holder and the amplitude was slowly increased. The sweep - step was repeated at least three times. Unless stated otherwise, the frequency shift Δf was determined in the limit of small amplitudes (< 0.5 nm) where partial slip is of negligible influence. Afterwards, the annealing of the film with attached particles was performed for 15 min by 150^0 C. The sample was cooled-down to room temperature and the frequency shift measurements were repeated. Finally, the surface was checked by AFM with respect to structural changes, utilizing the tapping mode as described in Chapter 6.

20 µm particles

After the deposition of particles with a diameter of 20 µm on a PS coated surface the measured resonance frequency always increased (Fig. 5.5.). From optical microscopy, the areal number density N/A_Q in the particular experiment shown in Fig. 4.3. was determined to be about 30 particles/mm^2.

Right after the first deposition of particles (Fig. 5.5, black squares) a Δf of 350 Hz was observed. Such an increase of the resonance frequency after addition of particles has been observed before [30]. This system is in the weak-coupling regime. Quantitative analysis of the frequency shift with Eq. (58) yields a surprisingly high value for the spring constant, k. Particle counting using video microscopy yielded a particle density N/A_Q of the order of 30 particles/mm^2. With $\Delta f \approx 350$ Hz (first sweep), Eq. (58) yields a spring constant of $k \approx 6000$ N/m. This value can be compared to Hertz theory. The spring constant and the modulus are

given in Eq. 67, while the contact radius, a, as predicted from Hertz theory is derived in Eq. 68.

In the following, the glass beads are taken to be much stiffer than polystyrene. In other words the second terms in Eqs. 67 and 68 ($G_2 \approx E_2 \approx \infty$) are neglected. For polystyrene at MHz frequencies, the shear modulus has been determined to be about 2 GPa [108]. Inserting these values, one finds a lateral spring constant of about 1000 N/m, which is a factor of 6 lower than the experimental value. In order to match the experimental value of 6000 N/m, one would have to use a shear modulus of 25 GPa, which is highly unrealistic. The contact radius according to Hertz theory is 110 nm, used here for comparison reasons. This value is less than the thickness of the polystyrene film. While the finite thickness may be of some influence in principle, it is hard to see how the correction should amount to a factor of 6. Unexpectedly high values for the spring constant as derived from Hertz theory have been found before [109]. The discrepancy has often surpassed a factor of 10. While there is no rigorous explanation at hand, it can be suggested that the result can be understood on a qualitative level, assuming a multiasperity contact.

In the first sweep, the oscillation amplitude was increased from $u_0 = 0.1$ nm to 4 nm (to avoid nonlinearities above ~10 nm). Video microscopy did not reveal significant movement of the particles. Less than 5% of the particles fell off or moved on the surface. In the second sweep, the resonance frequency increased by 2.5 kHz relative to the clean PS film. This indicates a tighter coupling. This “consolidation” of the particle-PS contact can be interpreted in the following way: Neither the particle nor the PS surface is perfectly homogeneous. During the first sweep, the particles rotate and oscillate and in this way they obtain an optimum binding position. In the third sweep (Fig. 5.5, red circles) only a slight decrease in the resonance frequency was observed. No changes were detected by video microscopy, suggesting that the mean coupling constant shifts back to slightly lower values during that sweep.

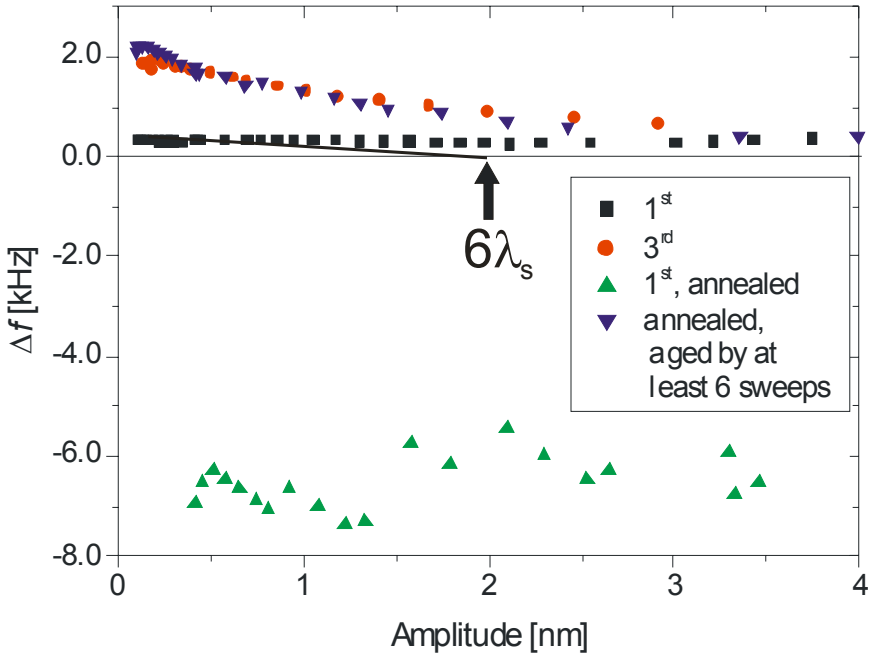

Fig. 5.5: Shifts of frequency versus amplitude of oscillation for the 20 µm particles. All spheres had been deposited on a polystyrene film of thickness 160 ± 20 nm. Black squares show the first sweep after particle deposition. Red circles show the third sweep after deposition. The oscillation of crystal has changed the nature of the contact. Green upper triangle show the first sweep after high-temperature annealing of polystyrene film. The negative frequency shift suggests increase of the contact strength. Blue lower triangles show results taken after extended aging of these contacts. Higher oscillation amplitude has modified the nature of the contacts.

The fact that consolidation is a major effect was supported by the AFM adhesion force measurements. Adhesion varied from one position to another by a factor of approximately 2-3. Furthermore, the absolute value of 30-70 nN is relatively low. The model of Johnson, Kendall, and Roberts [73] was utilized for an estimation of the adhesion. The adhesion force between an elastic sphere and a planar surface is $F = 3\pi WR/2$, where W is the work of adhesion per unit area. With W = 0.03 N/m and F = 70 nN an effective radius of the sphere can be estimated to be 0.5 µm. This is much lower than the actual radius and indicates that surface roughness and particle inhomogeneities, as mentioned above, can lead to a significantly reduced contact area.

The partial slip length is read from the Δf-vs-amplitude by fitting a straight line to the data at low amplitudes and extrapolating this line to $\Delta f = 0$ according to Eq. 61. The dashed lines at the top of Fig. 3.11 show these extrapolations. For the particles with 20 µm diameter, the partial slip length is of the order of 0.6 nm. With an adhesion force of $F_\perp$ = 1.1 µN and a

spring constant of $k = 6000$ N/m, one finds an apparent static friction coefficient of $\mu_S \approx F_\perp/(k\lambda_S) \approx 0.3$. While this value is in the expected range, μ_S derived from λ_S and the Mindlin model has occasionally also been found to be somewhat larger than unity [109]. This may well go back to a short-coming of the Mindlin model. However, a μ_S being larger than unity may also be a consequence of the fast oscillation. This would imply, that the induction of partial slip takes time and is less efficient at MHz frequency, than it would be in conventional macroscopic experiments.

At this point one can contemplate the possibility of a *rotation* of the sphere under the force of inertia. The Mindlin model assumes that the bulk of the sphere remains in rest. It neither translates, nor rotates. Evidently, this is not fully realistic. One expects a slight periodic rotatory component to the motion, in which case the presented experiments would probe rolling friction rather than Mindlin microslip. The deformation pattern in the contact zone would consist of a combination of shear and elongation, rather than pure shear. Finite element calculations show that the amplitude of rotation is very small [110]. The pattern of deformation mostly is a shear deformation. However, if the moduli of the two contacting materials are different, there still is a *vertical* stress component at the rim of the contact area. This fact is well known from fracture mechanics [111]. For a hard-soft contact, shear-induced crack propagation always entails a normal tensile stress, termed „mode II crack opening“ in this context. The essence of the Mindlin model (partial slip) certainly remains correct even for mode II, concerning crack opening, but the details may need refinement.

After three sweeps on the QCM-particles system, the quartz crystal (including the particles) was annealed at 150°C for 15 min in a preheated oven. After annealing and cooling the frequency decreased to Δf = 6.9 kHz (Fig. 5.5, green upper triangles). Following the Dybwad model, one concludes that the contacts are now in the tight-coupling regime. Annealing leads to the formation of a PS meniscus and binds the particles stronger to the quartz. Meniscus formation was confirmed by atomic force microscopy (AFM). Under control of an optical microscope a particle was removed from the surface with the tip of an AFM. Subsequently, the PS surface was imaged in tapping mode. The dimensions of the remaining menisci could be determined by AFM (Fig. 6.6).

Using the Sauerbrey equation, one can check whether the weight of the particles as determined by QCM matches the number density from particle counting. The latter was 30 particles/mm^2. If one assumes that the particles are tightly bound, the density of 26 particles/mm^2 is calculated from Eq. 18. One could conclude that roughly 80% of the particles

are tightly bound to the QCM surface and follow its movement. In the framework of Fig. 3.8, the system would be on the far left in the strong-coupling regime. However, it should be pointed out that this is no unique conclusion. The system could also be in the intermediate regime with $\bar{k}$ being slightly above the resonance point.

In the following sweeps leading to the aged state (blue lower triangles), the resonance frequency gradually increased until the same state, as before temperature annealing, was reached. This increase is interpreted as a reduction of the mean coupling constant. Actually, the frequency shift remained below 4 kHz, as long as the amplitude sweeps did not exceed 3 nm. However, after several sweeps, it was observed that, for amplitudes above 4 nm the frequency shift reached the level that the system exhibited before annealing (see Fig. 5.5).

After annealing no particle movement or detachment was detected by video microscopy, an observation which is in agreement with the negative frequency shift (for mass loss one would expect an increasing Δf) and excludes mass loss. However, as discussed in the above paragraph, after "ageing" with repeating sweeps above a specific relatively large amplitude (here 4 nm), the system retrieves the increased frequency shift values. Therefore it is concluded that, if the amplitudes are high enough, the bond between the particles and the PS surface can be reduced again to the level of the binding strength before annealing. With decreasing mean coupling constant the system can go from negative frequency shifts in the strong-coupling regime to positive frequency shifts in the weak-coupling regime.

15 µm particles

A similar positive frequency shift after particle deposition was observed with 15 µm particles. In the example shown in Fig. 5.6, the frequency increased by 360 Hz upon addition of particles. It further increased by 390 Hz in the second sweep. Afterwards, it remained constant as long as the oscillation amplitude did not exceed 5 nm. No particle movement or loss of particles was observed by video microscopy. Annealing caused Δf to become negative (1.9 kHz). As for the 20 µm particles, the decrease of the resonance frequency is attributed to a tight coupling of the particles and the accompanying increase in effective mass. In contrast to the larger particles, the resonance frequency did not change in all following sweeps, even when increasing the amplitude to 10 nm. Video microscopy showed no indication of particle movement or loss.

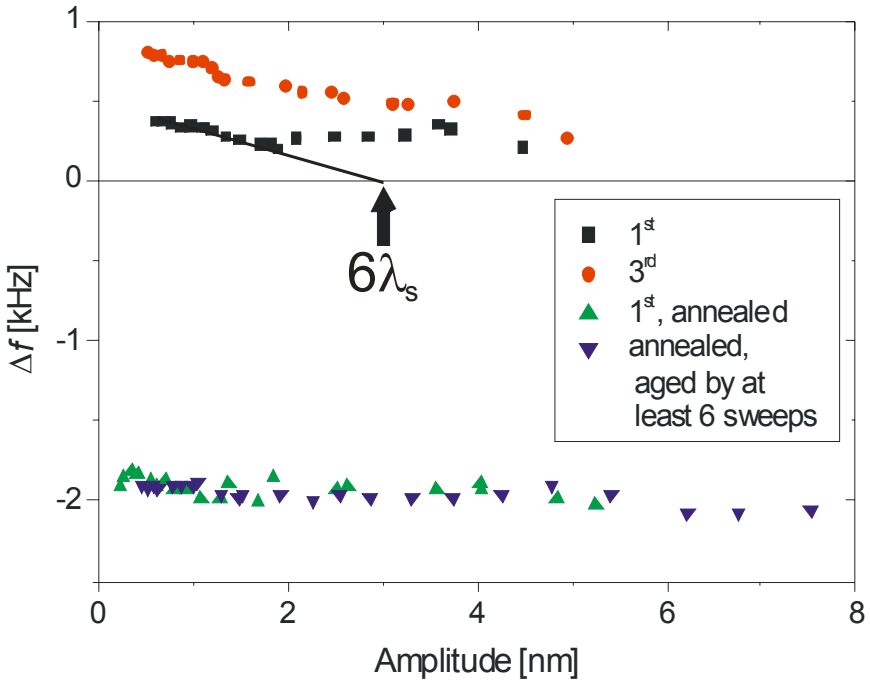

Fig. 5.6: Shifts of frequency versus amplitude of oscillation for the 15 µm particles. Black squares show the first sweep after particle deposition. Red circles show the third sweep after deposition. Green upper triangle show the first sweep after high-temperature annealing of polystyrene film. Blue lower triangles show results taken after extended aging of these contacts by large amplitude oscillation of the crystal.

To explain the fact that the 15 µm particles were not decoupled by resonating at high amplitude, the force acting on the particle is calculated. Assuming that particles move with the quartz surface, their position is given by $u_0 \cos(\omega_0 t)$. The force required to oscillate the particle is then:

$$F_{osc} = -m\omega_0^2 u_0 \cos(\omega_0 t) \qquad \text{Eq. 71}$$

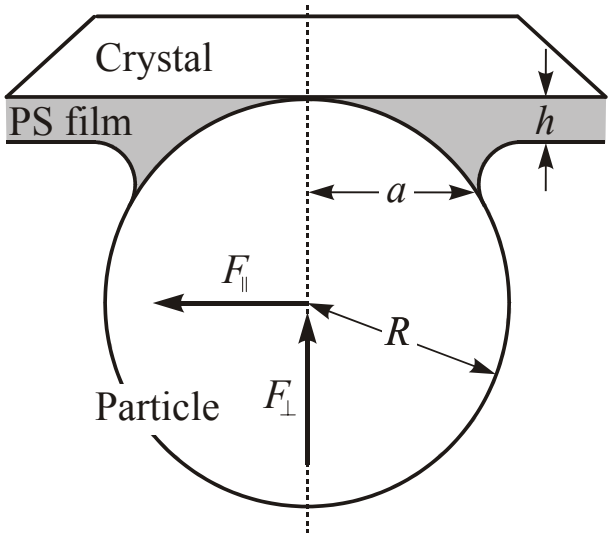

Fig. 5.7: Schematic of a particle after annealing with a meniscus of PS.

The peak force is $4\pi R^3 \rho u_0 \omega_0^2 / 3$. It increases with the third power of the particle radius. This has to be compared to the force binding the particles to the surface. This binding force is expected to grow proportional to *R*, though it is not clear how the binding between the particle and the PS surface is broken. One might argue that in the absence of elastic strain the adhesion force is proportional to the contact area. For a given film thickness with $h << R$, the contact area is approximately given by πa^2, where *a* is the contact radius. Here, the influence of the meniscus is neglected. With $a^2 = 2hR - h^2 \approx 2hR$ the contact area increases proportionaly to *R*. Thus, the oscillation force due to the inertia of the particle increases with R^3 while the binding to the PS is expected to increase only with *R*. For large particles the oscillation force is more likely to detach the particles, while for small particles the binding force should dominate.

One might also argue via the torque. To detach the particle from its meniscus it would need to roll up onto the film. The maximal torque leading to it is $(R-h)\cdot 4\pi R^3 \rho u_0 \omega_0^2 / 3$ $\approx 4\pi R^4 \rho u_0 \omega_0^2 / 3$. Adhesion appears to resist to rolling. For a particle to roll, the torque aF_{adh} has to be overcome. Assuming that the adhesion force scales with the contact area, the resistance is proportional to $a^3 = (2hR)^{3/2}$. Again, large particles should detach more easily under an oscillating lateral force than small particles.

The experiments with the 15 µm particles revealed an intrinsic problem of the particle-surface system, as described by the Dybwad model, which complicates the quantitative interpretation of the results. Due to inertia effects, spheres of specific mass do not exactly

follow the oscillatory movement. Therefore do not contribute to the frequency shift as expected from the Sauerbrey model. Within the semi quantitative model (Fig. 3.8), this is explained by the system being in the intermediate regime between strong and weak coupling. When $\bar{k}$ is around the resonance condition, ($\bar{k} \approx \omega^2 m$), a quantitative analysis is difficult and this is probably the case with these specific particle-masses. Therefore, when comparing the number of particles per unit area observed by microscopy with the mass per unit area derived from the Sauerbrey equation, the latter is often found to be much smaller, due to the phenomena described above (inertia, contact distribution and mean coupling constant approximately in the resonance condition due to the particle mass). The difference for this specific system amounted to up to a factor of 5.

10 µm particles

Deposition of 10 µm particles caused the frequency to increase by 280 Hz (Fig. 5.8, black squares). Increasing the oscillation amplitude up to 5 nm caused no optical detectable changes, although the frequency decreased by 75 Hz in the second sweep. The frequency shift Δf remained stable after the second sweep. The red circles in Fig. 5.8 show the third sweep. In contrast to the larger particles, annealing caused an *increase* of Δf to a value of $\Delta f \approx +450$ Hz, rather than a decrease. Evidently, annealing in this case was not sufficient to reach the strong-coupling regime. Parameter $\bar{k}$ increased, pushing the system to towards the resonance condition (thereby increasing Δf). However, the increase did not carry the system beyond the resonance condition.

Sweeps with a maximum amplitude of about 6 nm caused a further small increase of Δf by about 50 Hz. Increasing the amplitude to 10 nm caused particle loss and a decrease of Δf down to 285 Hz. Further increasing the amplitude to 16 nm left the sample unchanged.

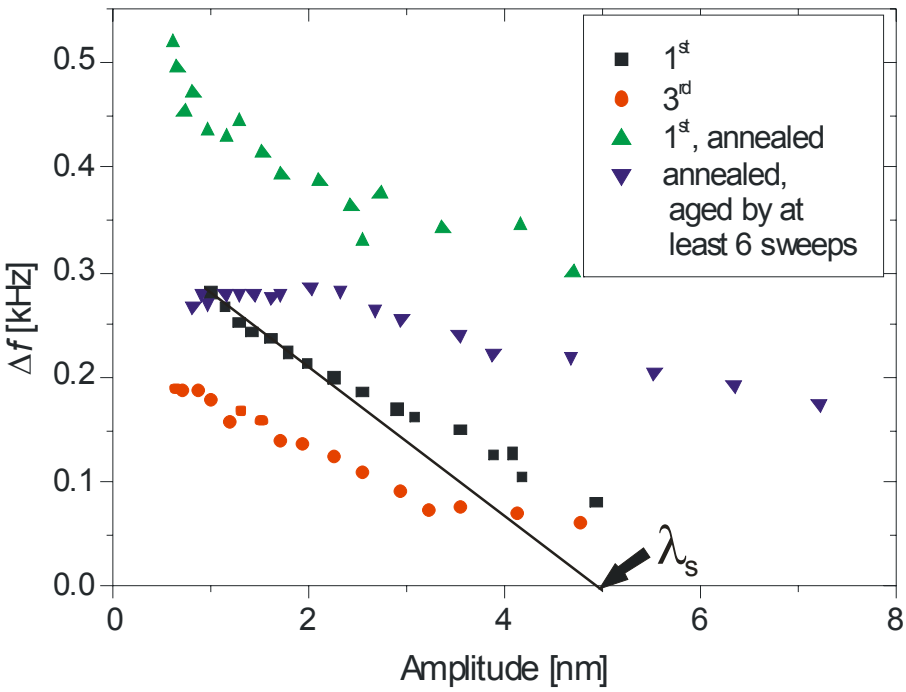

Fig. 5.8: Shifts of frequency versus amplitude of oscillation for the 10 µm particles. Black squares show the first sweep after particle deposition. Red circles show the third sweep after deposition. Green upper triangle show the first sweep after high-temperature annealing of polystyrene film. Blue lower triangles show results taken after extended aging of these contacts by oscillation of the crystal.

5 µm particles

When the smallest particles were added, a decrease of the frequency by $\Delta f \approx$ -200 Hz was observed (Fig. 5.9). Three amplitude sweeps did not change the frequency. After annealing, the frequency decreased up to $\Delta f \approx$ -400 Hz. Aging the sample at high amplitudes further decreased the frequency down to -600 Hz. These particles were found to be in the strong-coupling regime.

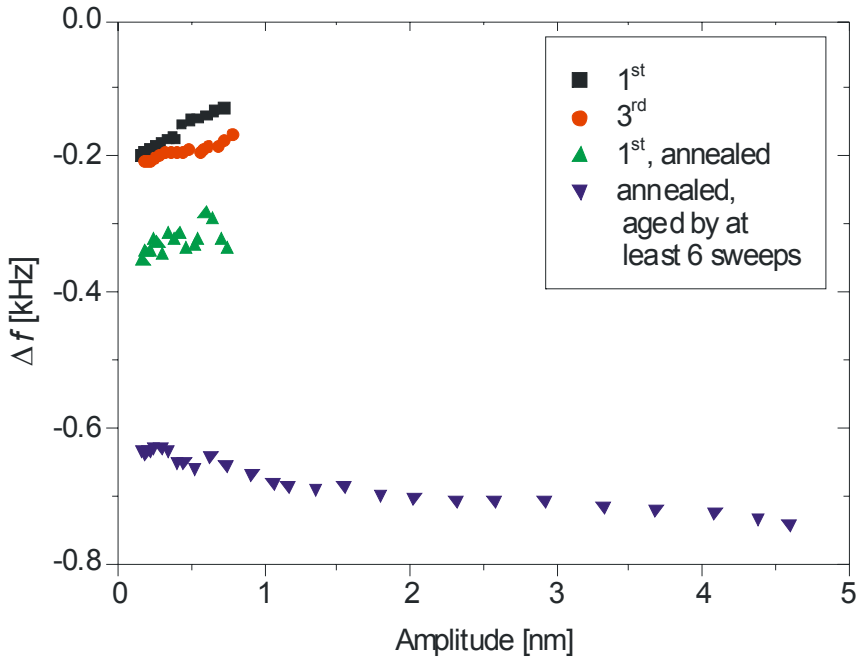

Fig. 5.9: Shifts of frequency (top) and bandwidth (bottom) versus amplitude of oscillation. Black squares show the first sweep after particle deposition. Red circles show the third sweep after deposition. Green upper triangle show the first sweep after high-temperature annealing of polystyrene film. Blue lower triangles show results taken after extended aging of these contacts by oscillation of the crystal.

5.3.1 Reproducibility issues

Each measurement was performed with a new quartz blank. As expected, there is a distribution in the quartz quality, clearly observed in the more than 300 pieces used, which affected the reproducibility of the measurements. Moreover, each electrode evaporation and polymer film deposition could be a further source of variation. The single measurements were repeated typically 10 times for 10 different quartz blanks. There was a qualitative agreement on the observed trends, while the absolute frequency values dependent strongly on the individual quartz and the particle number brought onto the surface. Therefore one representative value for each particle/surface combination that showed the typical response was reported.

5.4 Effect of overtone order

The resonance of the quartz crystals was measured with a HP 5100A network analyser. With this setup it is possible to excite and evaluate up to 20 overtones, depending on the quality of the quartz blanks [51]. These overtones are found at frequencies $f_n = n \times f_0$ with $n = 2k + 1$, k being an integer and f_0 being the fundamental frequency.

As presented by Laschtisch [112] the amplitude decreases with increasing overtone order due to the individual quality factors of each harmonic. The surface oscillation speed increases with the overtone order, mainly from the first to the third harmonic, also due to the strongly increasing quality factor, which is an expected behaviour. For each quartz however, the quality factor of the harmonics increases with increasing overtone order.

In this section, the mechanical microcontacts of fine particles are studied using the quartz crystal microbalance under oscillation and specifically focusing on the higher overtones. While for the previous experiments the focus was in the 3rd harmonic, here the effects on the higher harmonics (5th, 7th, 9th etc.) were additionally investigated. This is the first time that the analysis of the higher harmonics is utilized for such a study with the quartz-crystal system and it could provide with useful information for the particles movement and interaction with the polymer surface. The experimental procedure and sample preparation are the same as for the steps described in Chapter 4, with the only difference lying in the studied overtone (higher overtones instead of only the 3rd).

The correlation between particle/surface contact and higher overtones was done here by focusing on 5th and 7th overtone, of 30 and 42 MHz respectively. In order to have a defined comparison with the other results, the 3rd harmonic at 18 MHz was also recorded. In each experiment, the frequency shifts were measured for a stepwise increasing drive level. At each applied drive level the above overtones were successively measured before moving to the next higher amplitude value. As previously described, the particles were dry deposited on the PS surface and for each measurement step three runs were recorded. The PS film was annealed, by 150^{o} C for 15 min, in order to influence the binding between particles and the polymer surface.

5.4.1 Amplitude sweeps

The experiments had to be performed using very low amplitudes, in order to avoid particle dislocation or detachment. The mass change was avoided in order to study only the particle-surface interaction without any influence of particle-detachment on the recorded frequency shifts. Therefore the drive level applied was between -20dBm and -10dBm. The highest amplitude was detected for the 3rd overtone. As shown in Fig 5.10 for the PS coated electrode it was in the range between 0.24 and 0.75nm. The particle deposition caused an amplitude decrease, specifically for the 3rd overtone it was between 0.19 and 0.54 nm. Through annealing the amplitude was further lowered to the level of 0.05 – 0.1 nm. In this region the amplitude is not high enough to provoke particle movement on the surface. Furthermore, it should not significantly influence the binding strength. Therefore, all frequency shifts detected within this part of the study can be attributed solely to the applied oscillation. Phenomena such as partial slip, particle-detachment and particle movement ("jumping") can be excluded.

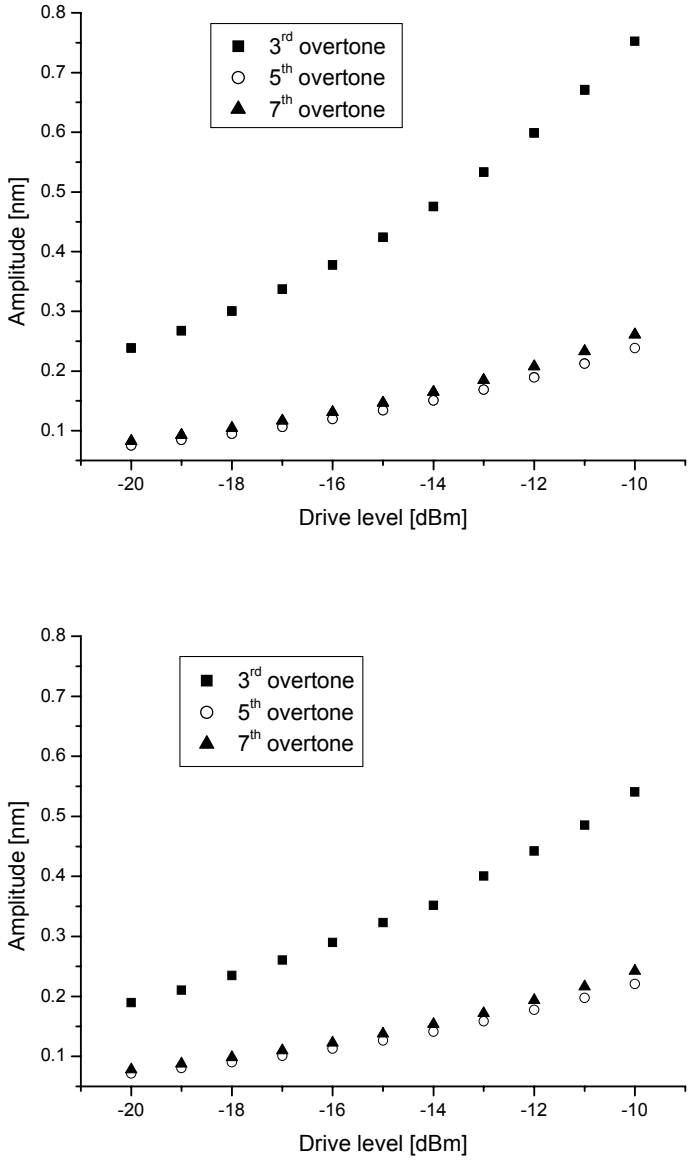

Fig. 5.10: Amplitude for 3rd, 5th and 7th overtone for PS coated electrode (above) and after particle (diameter 10μm) deposition (below). The amplitude level decreased significantly for all overtones.

5.4.2 Particles – surface interaction

5 μm particles

For the case of 5 μm particles the representative data for overtone comparison are presented in Fig. 5.11. As mentioned above, the smallest particles, deposited on the PS coated gold, caused for the 3rd overtone a frequency decrease, in this case by Δf = -1553 Hz. Similar behaviour was observed for the 5th overtone, where the frequency decrease was much stronger, Δf = -57379 Hz. The opposite effect was detected for the 7th overtone, where the frequency increased by Δf = +1085 Hz. As mentioned above, the amplitude range during these experiments was very low (down to 0.05 nm) and no optical changes on the surface were detected. Nevertheless, frequency shifts during each sweep for each overtone were recorded. Specifically the driving amplitude was in the range of 0.04 – 0.12, 0.02 – 0.06, 0.04 – 0.12 nm for 3rd, 5th and 7th overtone respectively, for the 1st run before annealing. The frequency shift as a function of the amplitude, D, during a sweep is defined as $df(D)$ and was also measured. For the 3rd overtone $df(D)$ was approximately -100Hz to -200 Hz. The 5th overtone frequency exhibited a $df(D)$ = -30 to -50 Hz, while the 7th overtone actually increased by $df(D)$ = 20 – 40 Hz.

After annealing, the frequency decreased by -5367 Hz and -58958 Hz for 3rd and 5th overtone respectively, using the clean PS film values as a reference. For the 7th overtone the frequency increased by +3526 Hz. Additionally during these three sweeps no particle movement was detected optically, however the frequency as a function of drive level for each sweep increased by 350 – 500 Hz, 50 – 150 Hz, 50 – 110 Hz for the 3rd, 5th, 7th overtone respectively.

The smallest particles exhibited a gradually decreasing frequency after deposition and after annealing for the 3rd and 5th overtones, as expected. However, the 7th overtone exhibited a deviating behaviour with a positive Δf at both tests (before and after annealing). The same contradiction was found for the frequency as a function of drive level at each sweep.

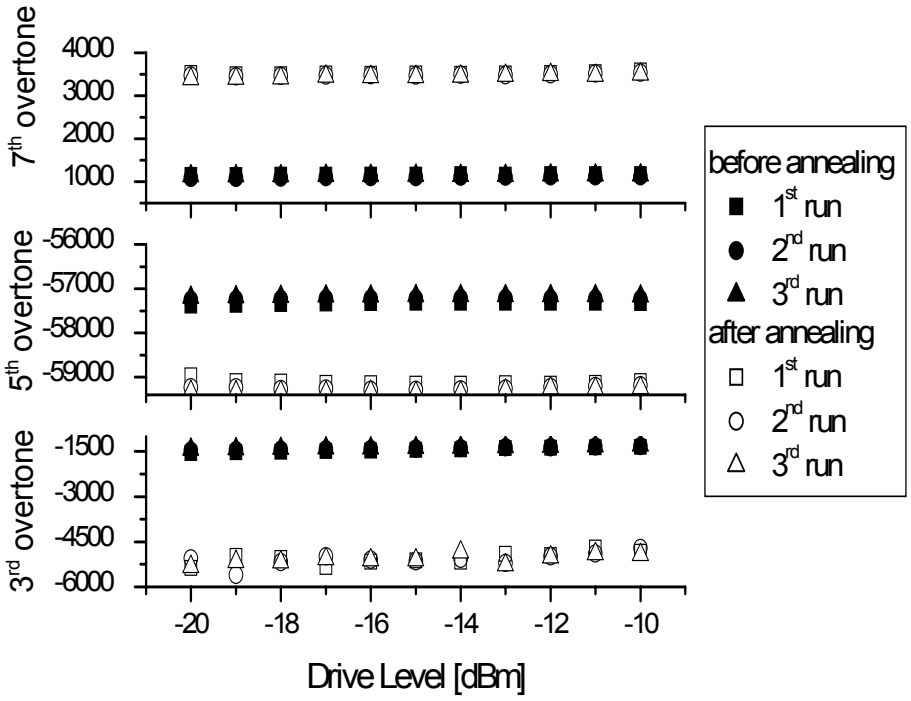

Fig. 5.11: Frequency shift for 5μm particles by 3rd, 5th and 7th overtone before and after annealing with particles. The 7th is the only overtone in this case exhibiting positive frequency shift.

10 μm particles

Deposition of 10 μm diameter particles caused the frequency increase by Δf = +230, +90, +33 Hz for 3rd, 5th and 7th overtone respectively (Fig. 5.12). The driving amplitude before annealing was in the range of 0.19 – 0.54 (3rd), 0.07 – 0.22 (5th), 0.08 – 0.24 nm (7th). During the measurement, the frequency as a function of drive level was not constant. For the 3rd overtone during a single sweep d$f(D)$ = -25 to -70 Hz, while for the 5th and 7th a minimal frequency increase by 1 – 30 and 1- 20 Hz, respectively, was observed. During the whole measurement process no particle movement was optically recorded.

In contrast to the other particles sizes, annealing caused an increase of the frequency for 3rd overtone by +491 Hz relative to clean PS film, while for 5th and 7th overtone Δf = –1713 and - 5257 Hz respectively, as presented in Fig. 5.12. In agreement with the observations for the 5 μm particles, also in this case during each sweep, the frequency varied as a function of drive level. For all three overtones d$f(D)$ during each sweep increased by 150 – 270 Hz, 50 – 70 Hz, 130 – 150 Hz for the 3rd, 5th and 7th overtone respectively.

Concerning these particle sizes, the 3rd overtone was consistently increasing after annealing. The higher overtones, 5th and 7th however exhibited an increase and only after annealing they decreased.

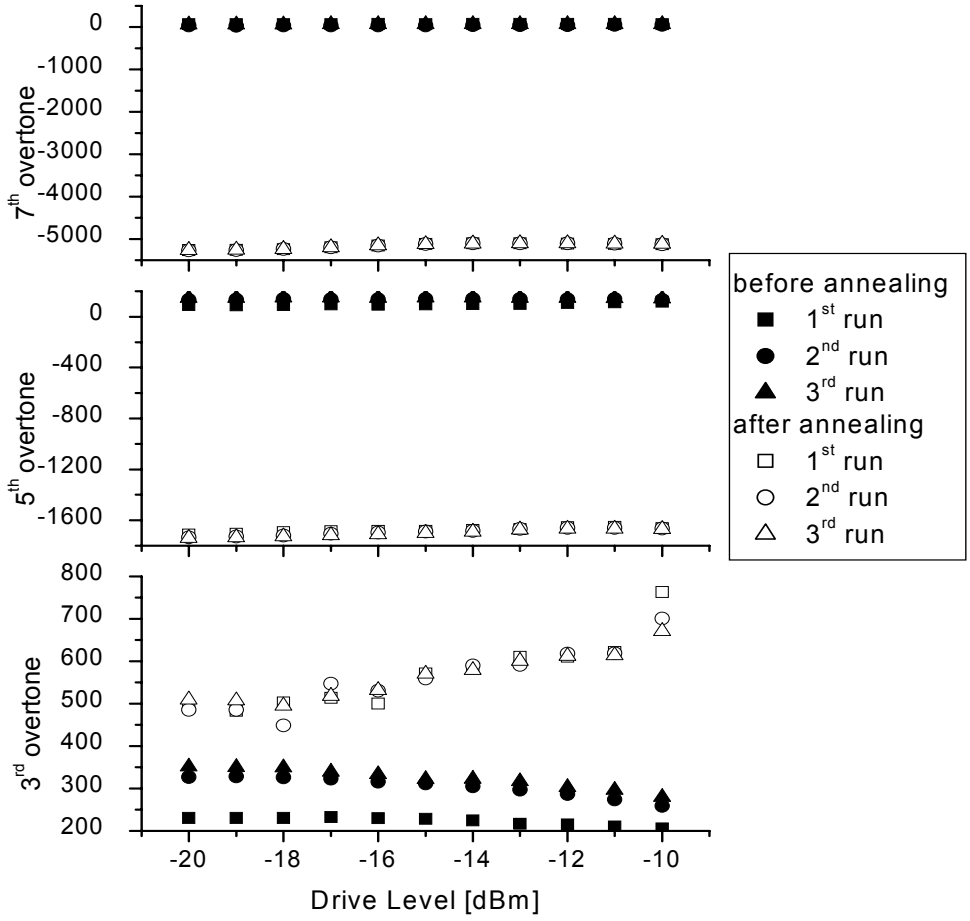

Fig. 5.12: Frequency shift for 10 μm particles by 3rd, 5th and 7th overtone before and after annealing with particles.

15 μm particles

A representative example of the experiment with 15 μm particles is depicted in Fig. 5.13. After particle deposition all three overtones were detected and the frequency increased by Δf = +356, +264 and +253 Hz for 3rd, 5th and 7th overtone respectively. During each sweep d$f(D)$ decreased by 10 – 70 Hz for each overtone. No particle movement or loss was observed by video microscopy. Annealing caused a significant frequency decrease measured by 3rd overtone at Δf = -3180 Hz, by 5th overtone at Δf = -15354 Hz. The 7th overtone resonance was not measurable due to insufficient sensitivity of the quartz.

For these larger particles, a frequency increase was observed before annealing and a significant decrease afterwards. Both detected overtones exhibited the same trend for particle deposition and annealing as well as during each individual sweep.

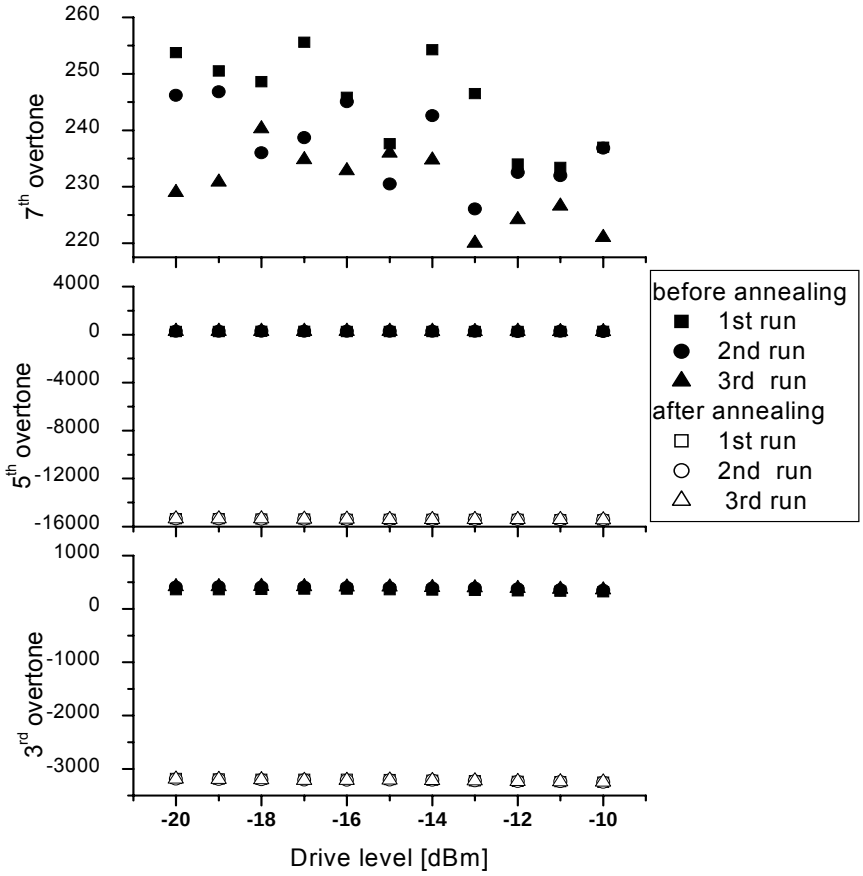

Fig. 5.13: Frequency shift for 15 µm particles by 3rd, 5th and 7th overtone before annealing and after annealing. After annealing resonance by 7th overtone was not measurable.

20 µm particles

After depositing the largest particles, 20 µm, on the polymer surface the resonance frequency increased for all three overtones in the range of Δf = 200 – 500 Hz (Fig 5.14). In this case the frequency-change during single sweep before annealing was minimal, d$f(D)$ = 1 to 15 Hz. As in other cases, no particle movement was optically observed. After annealing, the 5th overtone was not detectable, i.e. the resonance could not be found. For the 3rd overtone, the frequency decreased by Δf = -6857 Hz and the changes during single sweep were in the range of 100 Hz. For the 7th the frequency increased by +9547 Hz and remained stable with minimal changes of ~ 7 Hz.

As for 15 μm, the lowest resonance frequency, 3rd, exhibited a negative shift while the 7th increased significantly. The measured shift was relatively constant over the applied amplitude range for both recorded overtones, as well as before and after annealing. The mass of the particles appears to be large enough to obtain a constant resonance value at each sweep. However, the 7th overtone as before, appears to be affected by a different binding process than the 3rd.

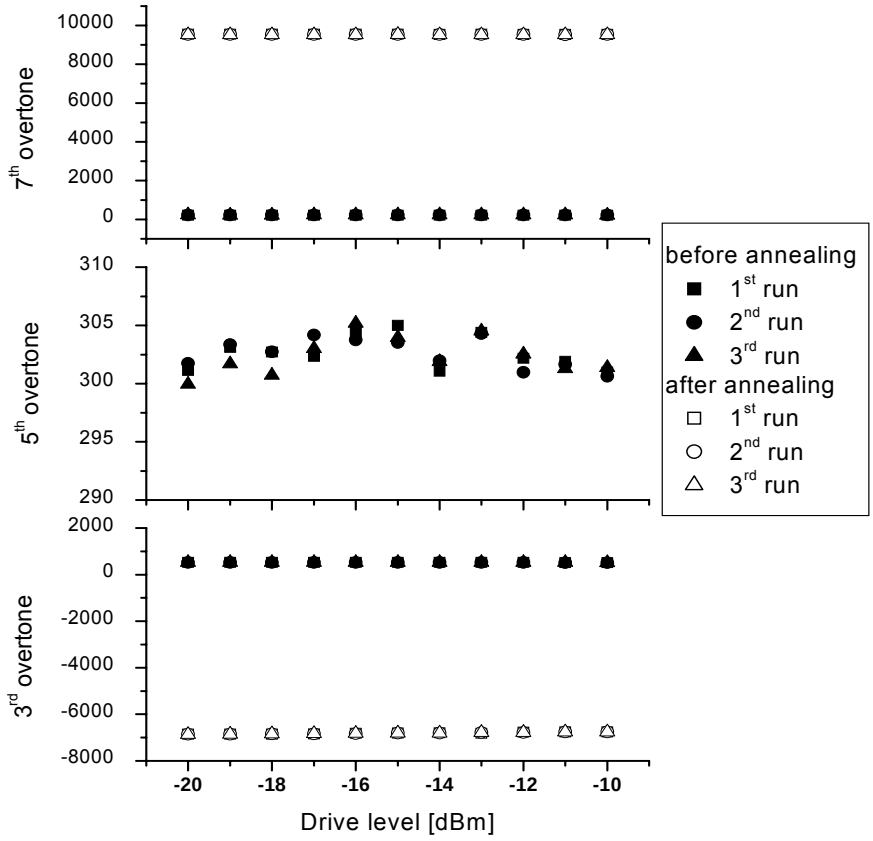

Fig. 5.14: Frequency shift for 20 μm particles by 3rd, 5th and 7th overtone before annealing, 3rd and 7th overtone after annealing

Summarizing the results presented for different particle diameters, the frequency shift at each overtone is relatively stable for the applied amplitude range. Minimal deviations are demonstrated in the level of ±10 Hz. In general for small particles, i.e. < 15μm, the shift for specific overtones can increase after annealing. For large particle diameters annealing causes a frequency shift decrease observed at all overtones.

The QCM vibration can drastically change the micromechanical contact between the surface and the attached particles. The oscillation can provoke the consolidation and enhancement of the particle-surface coupling. However, for specific higher frequencies, one observes a break-

down of the contact. More specifically, for particles with 5 and 20 μm at higher overtones (42 MHz, 7th harmonic) even very strong and stable particle-surface coupling can be destroyed. The frequency shift after annealing is in both cases therefore positive, which indicates that the system is in the weak-coupling regime. The opposite effect can be observed in the case of 10 μm particles where at 5th and 7th overtone, the system enters the tight-coupling regime and the frequency shifts are negative for these frequencies, indicating contact consolidation.

Furthermore, as for the most cases of the 3rd harmonic, at the 5th overtone an enhancement of the coupling between particle and surface is observed, after annealing. However, the oscillation at the highest here studied overtone, the 7th, appears to break the contact and the system enters the weak-coupling regime. The later happen for almost all particle diameters, before and after annealing, indicating that the forces applied on the particles are much higher than for the 5th overtone.

5.5 Calculation of particles per surface area

The number of particles on the active QCM surface can generally be estimated by optical measurements or calculated using the Sauerbrey equation (Eq. 18). Optical analysis was done for all particle sizes and the results were compared to the number of the particles detected by the quartz frequency shift, Δf. If the following assumption is made, that the particles are tightly bound and effectively increase the mass on the quartz, their number can be calculated from the frequency shifts, utilizing Eq. 18. The frequency shift value after annealing was used. The above equation is applicable only for a negative frequency shift. For the optical analysis of each quartz surface at least 30 images were taken and the mean particle-density on polymer surface was estimated. The effective area is assumed to be equal to the area of the small electrode (r = 0.35 cm, A = 0.38 cm^2). In the table 5.1, the number of the particles from imaging is compared to the calculated value for different overtones and the deviation of each value calculated from Δf to the quartz signal is attached.

A significant deviation is observed between the particle surface density microscopically observed and values deduced from the QCM measurements. The agreement is good for the largest particles. However, for the smallest particles, especially 5 μm, the surface density is by far overestimated. The difference between values delivered by each overtone is also significant. An example is the 15 μm case, where the 3rd underestimates while the 5th

overestimates the number of the particles. Nevertheless, for all cases except the smallest particles a qualitative agreement can be found.

It can be concluded that a significant fraction of the particles are tightly bound to the QCM surface and follow its movement, contributing to the particle surface density calculation i.e. giving a negative frequency shift. However, a remaining significant number of particles for all diameters is bound in a way that causes positive frequency shift or is not effective. It must be noted that the Sauerbrey model was applied for films and in this case it is not sufficient to describe the varying particle behaviour and the distribution of binding forces between particle and the polymer.

Therefore, the method appears to be applicable only for large particles, i.e. with diameters above 15 µm. For the case of smaller diameters, the particle density estimated by QCM would deviate even significantly. Thus it is relative for diameters <15 µm and can be used only for qualitative comparisons.

Particle diameter	Particle density - microscopy Particle/mm^2	Number of particles - microscopy particle/eff. Area	Quartz response 3rd overtone particle/eff. area	Quartz response 5th overtone particle/eff. area	Quartz response 7th overtone particle/eff. area
20 µm	**22**	**836**	**964** (+ 15%)	No data	Frequency increase
15 µm	**58**	**2204**	**1057** (-52%)	**3064** (+39%)	No data
10 µm	**43**	**1634**	Frequency increase	**1155** (-30%)	**2531** (+54%)
5 µm	**232**	**8816**	**48431** (+549%)	**318590** (+3613%)	Frequency increase

Table 5.1: Comparison of optical measurements (reference) with calculated particle density via quartz response and Sauerbrey equation. The deviation of the latter from the reference values is also given. Image size 1mm^2.

Mass of single particle: ø 20µm $M_p = 1.07 \cdot 10^{-11}$kg, ø 15µm $M_p = 4.52 \cdot 10^{-12}$kg,
ø 10µm $M_p = 1.34 \cdot 10^{-12}$kg, ø 5µm $M_p = 1.67 \cdot 10^{-13}$kg.

6. Atomic Force Microscopy – Force Measurements and Surface Imaging

Within this work, the Atomic Force Microscope (AFM) was used as a tool to image the topography of the surface at high resolution and to measure force-versus-distance-curves. The latter provided us with the range of adhesion force between particle and the surface. Knowing the interaction forces between colloidal particles and surfaces is a precondition for understanding the stability of dispersed systems and adhesion phenomena. In this chapter, the use of AFM to measure directly the force between a planar surface and an individual colloid particle is described. Therefore, a glass sphere was attached to the force sensor in the microscope and the force between the particle and the surface was measured, under ambient conditions. In the second part of this chapter, the surface changes occurring during quartz oscillations are studied and analysed.

6.1 Force measurements – colloidal probe technique

A modified AFM probe can be used for direct measurements of colloidal forces. This approach was presented by Ducker [67,68] et al. and Butt [69] and its application to adhesion force measurement was reviewed by Kappl et al. [113]. In this method a micron-sized particle, of well defined spherical shape is glued to the end of an AFM cantilever, which serves as the force sensor. This type of configuration allows direct force measurements. Additionally, the same single particle, that is already attached to the AFM cantilever, can be used for further experiments. In that case, the particle-surface should be examined after each measurement/application and any contamination must be excluded before proceeding with the next experiments. The accessible range of particle size is typically limited to a range between 1-50 μm [113]. The measuring principle of the colloidal probe technique is otherwise identical to that of a standard AFM as introduced in Chapter 3.2.1.

Particle attachment

In order to measure the adhesion force between particles and the polystyrene (PS) coated surface using the colloid probe technique, borosilicate glass spheres with 10 μm diameter were glued with epoxy glue (UHU plus endfest 300, UHU, Buehl, Germany) to the end of AFM cantilevers (Schaefer Technologie, Langen, Germany, tipless rectangular silicon cantilever, length 350 μm, 2.0 μm thick, resonant frequency 21 kHz). For securing the placement of extremely small amount of glue and the colloidal particle in correct position, onto the very end of the cantilever, a micromanipulator (three dimensional oil-hydraulic manipulator MNO-203, Narishige Group, Japan) under the control of an optical microscope was used.

Spring constant calibration

To evaluate the adhesion force value from the experimental data, the cantilever deflection has to be multiplied with the spring constant of the cantilever. The spring constant of the cantilevers was determined by the reference spring method introduced by Gibson et al. [63] and Torii et al. [114]. The reference cantilever was calibrated using the thermal noise method introduced by Hutter and Bechhoefer [115]. According to the reference spring method, two cantilevers are used. The one is the 'unknown' with an attached sphere and the second 'standard' cantilever is calibrated by thermal tuning.

The 'unknown' cantilever was attached to a substrate, with the particle side up, and pressed against the 'standard' lever, that is mounted in the sensor head of the AFM in the normal configuration. In the first step, a force vs. distance curve with the 'standard' lever being driven against a flat and hard surface (e.g. lever holder) is obtained. In the next step, the end of the 'standard' cantilever is brought in contact with the end of the 'unknown' lever, see Fig. 6.1. The series of force-distance curves are obtained in order to arrive at a representative average value of the slope. Deflection of the 'standard' lever as a function of the z-height of the stage is measured during the approach and retract cycles. Since the force constant, k_0, of the 'standard' lever is known, that of the 'unknown', k_1, can be calculated from [63]

$$k_1 = k_0\left[C(D/N) - 1\right] \qquad \text{Eq. 72}$$

where *D* is the z-height travel of the stage, *C* is the nV to nm conversion factor, and *N* is the deflection (in nA) of the 'unknown' cantilever after contact.

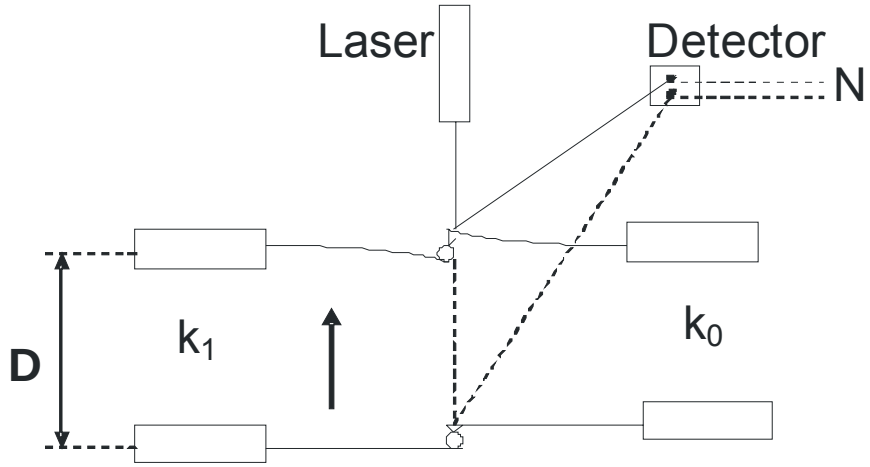

Fig. 6.1: Schematic setup for spring constant calibration of the mass loaded cantilever. 'Standard' lever, k_0, 'unknown' lever, k_1, in their initial position, and after the sample stage has been moved a vertical distance *D*. The deflection of the 'unknown' lever is *N*.

6.2 Adhesion force measurements

The adhesion force between borosilicate glass particle, with diameter of 10 μm attached to the cantilever (Fig. 6.2) and polystyrene (PS) coated surface was measured. All results were taken by using the so-called force-volume-mode. In this mode, forces-distance curves are not only measured on one selected point of the sample, but are acquired in every point corresponding to a pixel of the AFM image. Form the array of force-distance curves the spatial variation of the interactions throughout the sample surface can be obtained [29]. Within this work the force curves were taken on a grid of 32 × 32 points, within a scan area of 500 × 500 nm. The measured adhesion force for this system, F_{adh}, was in the rage between 30 – 70 nN depending on the position on the surface. A histogram of adhesion forces for the specific system is shown in Fig. 6.3. Those data represent the value of measured adhesion force for the same cantilever taken in three different positions on the same PS coated quartz crystal. As expected this measurements shows a specific distribution of adhesion forces, rather than a single value. For the estimation of the adhesion energy the theory of Johnson, Kendall, and

Roberts[73] was applied in order to model the experimentally observed interactions (see Chapter 3.5). The adhesion force between an elastic sphere and a planar surface is $F = 3\pi WR/2$, where W is the work of adhesion per unit area. Assuming a typical value of W = 0.03 N/m for polymer surfaces and the measured adhesion force F = 70 nN an effective radius of the sphere would result in R = 0.5 µm. This is much lower than the actual particle radius and indicates that the surface roughness reduced the contact area significantly. If the actual particle radius is used in the above relation (R is set to 5µm), then from the maximum measured force of 70 nN, one would calculate a work of adhesion as low as W = 0.003 N/m, which is far too small for the specific system.

The influence of surface roughness and surface heterogeneity on variation of force value was investigated and reported by several research groups [22,23,25-27,116]. Roughness can cause a significant change in the contact area of two particles, depending on the location of this contact. Heterogeneity in chemical composition or molecular structure, at different length scales can cause a different energy of adhesion and thus a variation in the effective adhesion force, depending on the precise contact location. Nevertheless, for this specific system, roughness can only partially reduce the work of adhesion and is not the only factor for the almost 10-times lower W calculated compared to the expected values.

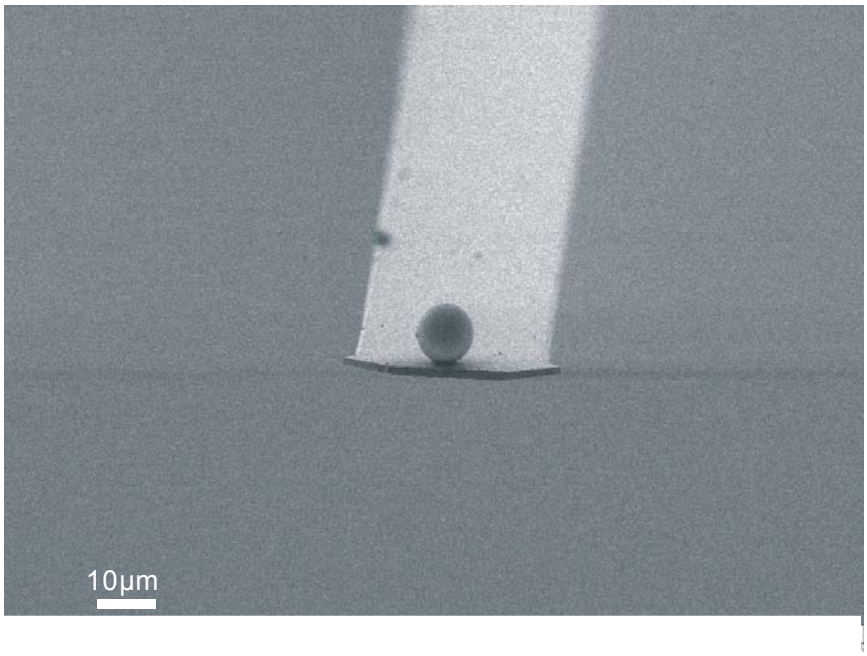

Fig. 6.2: SEM image of borosilicate glass particle attached to the cantilever

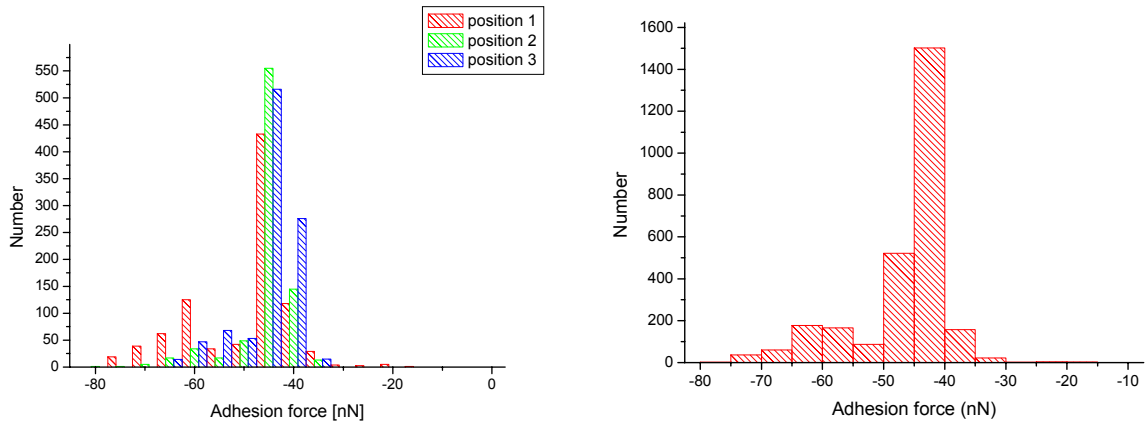

Fig. 6.3: Histogram of the distribution adhesion forces for one cantilever in 3 positions on the PS surface. On the right side the average values of the measurements at all three positions are plotted.

6.3 Surface changes caused by particles - Surface Imaging

In the previous paragraphs, the method of measuring forces with the AFM was presented. Moreover, the AFM technique can be utilized in order to determine surface topography, i.e. quality and possible surface changes from interactions. These can be quantified with the AFM in two commonly used modes, which are briefly presented in the Chapter 3.2.1.

6.3.1 Surface quality

AFM imaging in tapping mode (Dimension 3100, Veeco Instruments, cantilever tapping mode, OMLCLAC 160 TS-W2, Silicon) was used during this work to measure the roughness of the quartz surface. Surface roughness is one of the factors describing the surface quality and the influence on the interaction between particles and surface. Further factors of surface quality, which are less important for this system, can be the chemical homogeneity and density fluctuations. Firstly, the quality of gold electrodes was determined and an average root-mean-square (rms) roughness of σ_{rms} = 1.1 nm or below over an area of 5 x 5 μm^2 was found, which is quite low. Secondly, polystyrene (PS) coated gold electrodes were imaged and a mean rms roughness of 0.78 nm over an area of 5 x 5 μm^2 was found, confirming the good surface quality with relatively low roughness.

6.3.2 Surface damage by the particles

Within this section, the surface changes occurring during quartz oscillations are described. When the particles follow the QCM surface movement, the forces reach values that can be calculated by $F = m\omega_r^2 A_0$, where m is the particle mass, ω_r is the resonance frequency and A_0 the amplitude. For the 20 μm particles, with m = 10 ng, ω_r = 113 MHz, and $A_0 \approx 20$ nm peak forces are calculated to reach 2.7 mN. This can lead to high local stresses in the polymer. Assuming a contact area of 1 μm^2 for example, leads to an applied pressure of 3 GPa. Such a pressure may lead to irreversible deformation of the polymer surface. For this reason, by utilizing AFM the polymer film was investigated, regarding deformation that are attributed to the glass particle movement takes place. The particle was removed from the surface using an AFM tip. The particle detachment using the AFM setup was simultaneously monitored with an optical microscope. Subsequently, the PS surface was imaged in tapping mode and the detected particle traces were quantified.

As a first control, particles were placed on an annealed PS coated surface without quartz oscillation. After 24 h the particles were carefully removed with the help of the cantilever and the surface was directly afterwards imaged with the AFM tapping-mode technique. It was observed that the particles left barely visible marks on the surface. The picture in Fig. 6.4 depicts an example of the imprint left by a 20 μm particle. The diameter of this mark was 0.6 μm with a depth of less than 10 nm. The fact that such structures, which are quite small compared to the particle diameter, could be found after the particle-removal is surprising. Nevertheless, there was no doubt that this is an imprint of a particle on the surface, since these structures were repeatedly detected.

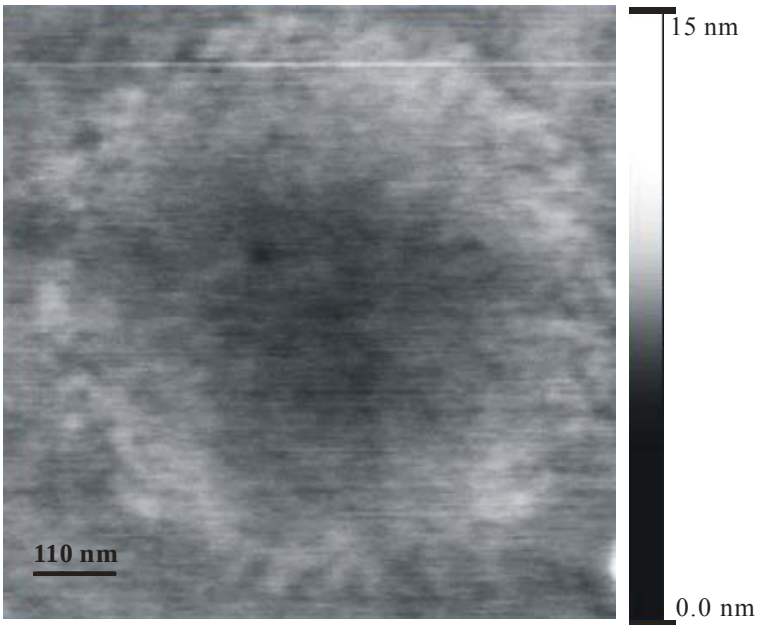

Fig. 6.4: Structural changes on the PS coated gold before quartz oscillation and after removing a 20 μm particle.

After resonating the quartz up to the amplitude where the particles started to move and change their position, the structural changes induced at the film surface were detected (Fig. 6.5). Different kinds of marks were observed, suggesting that the particle-behaviour was heterogeneous. In some cases, the particles remained at their lateral position and formed an imprint at that point (Fig. 6.5a). In other cases, several such repeating imprints side-by-side and partially overlapping were observed (Fig. 6.5b). The particle seemed to have jumped from one position to the next but stayed at every position for many vibrations of the QCM. Finally, several particles appeared to have "jumped" at every vibration of the QCM so that periodic marks were left in the PS film, which should be correlated with the QCM frequency (Fig. 6.5c).

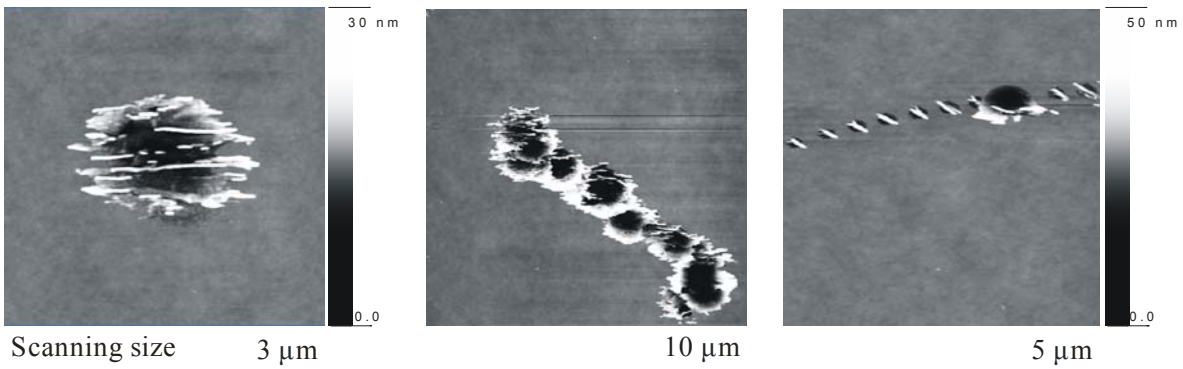

Fig. 6.5 (a – c): AFM image of surface changes after quartz stimulation with 20 µm particles. a) circular prints after particle detachment with diameters - ~1.3µm, depth ~ 20nm, occurring for less than 50% of the particles. b, c) dislocation of the particle on the surface, occurred for less than 3% of the particles

These particular traces allowed us to estimate particle velocity during the quartz oscillation. In the example shown in Fig. 6.5c, the 20 µm particle needed 6 periods in order to move 3 µm. At a frequency of 18 MHz that leads to an escape velocity of 9 m/s. Assuming that the particle was trapped at the upper right mark for many periods it had to accelerate to the speed of 9 m/s within one half period (28 ns). To achieve the corresponding acceleration of 3.2×10^8 m/s^2 a minimal force of 3.5 mN is required. This force magnitude is in agreement with the above estimation of the forces acting on the particles. Structural changes, as shown in Fig. 6.5, were observed for 10 - 20 µm particles. Only the smallest 5 µm particles left no structural changes, at least not within the applied amplitude range.

An alternative explanation, which leads to a lower estimate for the horizontal velocity, v_h has to be also mentioned. Due to the vibration of the QCM the particle is not only accelerated horizontally but also vertically. Considering that it has to overcome the polystyrene meniscus it is reasonable to assume that a vertical component, v_v, is present. Like a stone thrown at grazing angle over water the particle might jump up and down while moving laterally over the polystyrene surface. The force attracting it back to the surface is the van der Waals force. At each touch of the surface an imprint is left behind due to the vibrating QCM surface. In order to estimate the lateral velocity of the particle, the time for one jump has to be determined first. The vertical velocity has to be lower than the escape velocity. The escape velocity is the velocity of the particle which would allow it to escape the van der Waals attraction. Setting the potential van der Waals energy of the particles in contact with the surface, $A_H R/6D_0$, equal to the kinetic energy required to leave the surface, $mv_e^2/2$ with $m = 4\pi R^3\rho/3$, an escape velocity is obtained from the following relationship:

Eq. 73

$$v_e = \frac{1}{R}\sqrt{\frac{A_H}{4\pi\rho D_0}}$$

With typical values for the parameters ($A_H = 2\times10^{-20}$ J, $D_0 = 0.17$ nm, $\rho = 2500$ kg/m^3) a value of $v_e \approx 6$ mm/s is derived. In the present set of experiments the particles fall off once gravitation is stronger than the van der Waals forces. For a particle radius of 10 μm a fall-off distance of $D = 18$ nm is obtained. The time of one jump can be estimated to be $\tau = D/v_e \approx 3$ μs. With a spacing of 0.5 μm (6 "particle-jumps" in a distance of 3μm) between the elongated marks on the surface, the horizontal velocity is estimated to be approximately 0.16 m/s.

6.3.3 Meniscus formation

The final step in the surface characterisation was to obtain images after annealing with particles on the PS coated electrode, thus confirming the meniscus formation. The particles were removed by an AFM cantilever and a microscope camera allowed their detection. The removal was carefully performed and controlled in order to minimize the destruction of the meniscus and leave the rim unaffected. Nevertheless, for some cases the particle was strongly bonded to the film, thus causing rim damage during removal and detachment. However this was easily detectable and taken into consideration. An alternative method of particle removal is difficult to apply, because the position of the removed particle has to be exactly defined for the AFM image. For the majority of the particle/surface contacts, this method did not significantly change the shape of the meniscus.

Three main types of meniscus shape were detected. The first was a symmetric imprint of a radius which corresponded to a full particle/polymer contact area. This is demonstrated in Fig. 6.6 and 6.7, where one can assume that the particle was tightly bound and the meniscus dimensions were correlated to the particle diameter. Figure 6.6 shows an example of the meniscus formed by a 10 μm particle. Similar structural changes were imaged for all particle sizes, e.g. for 20 μm as demonstrated in 6.7. The meniscus created was 80 – 130 nm deep and the diameter was in the range of 3 to 6 μm, dependent from the particle size.

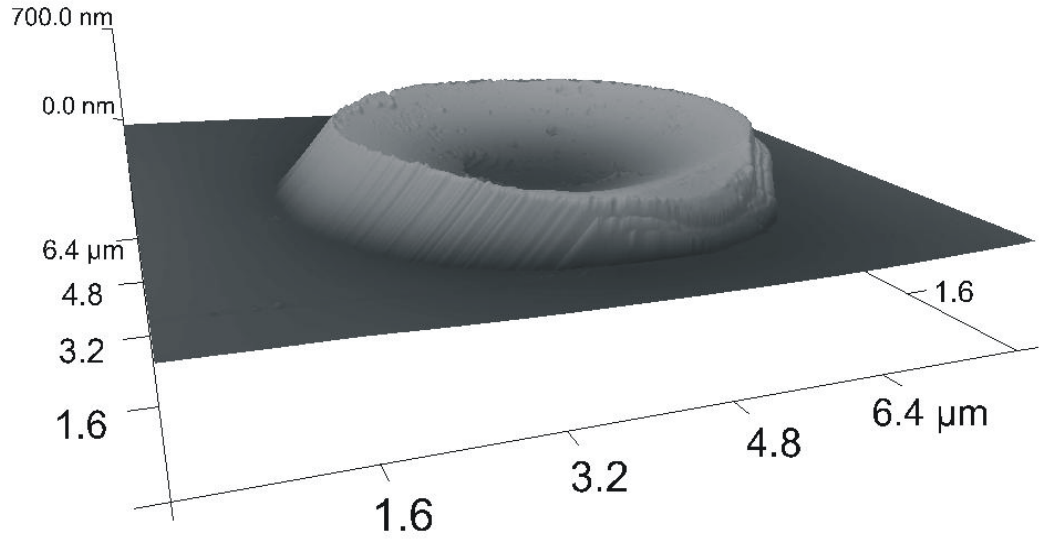

Fig. 6.6: AFM image of the meniscus after sample annealing with 10 µm particles; diameter 4.5 µm, meniscus height ~ 400 nm, scanning size 8 µm

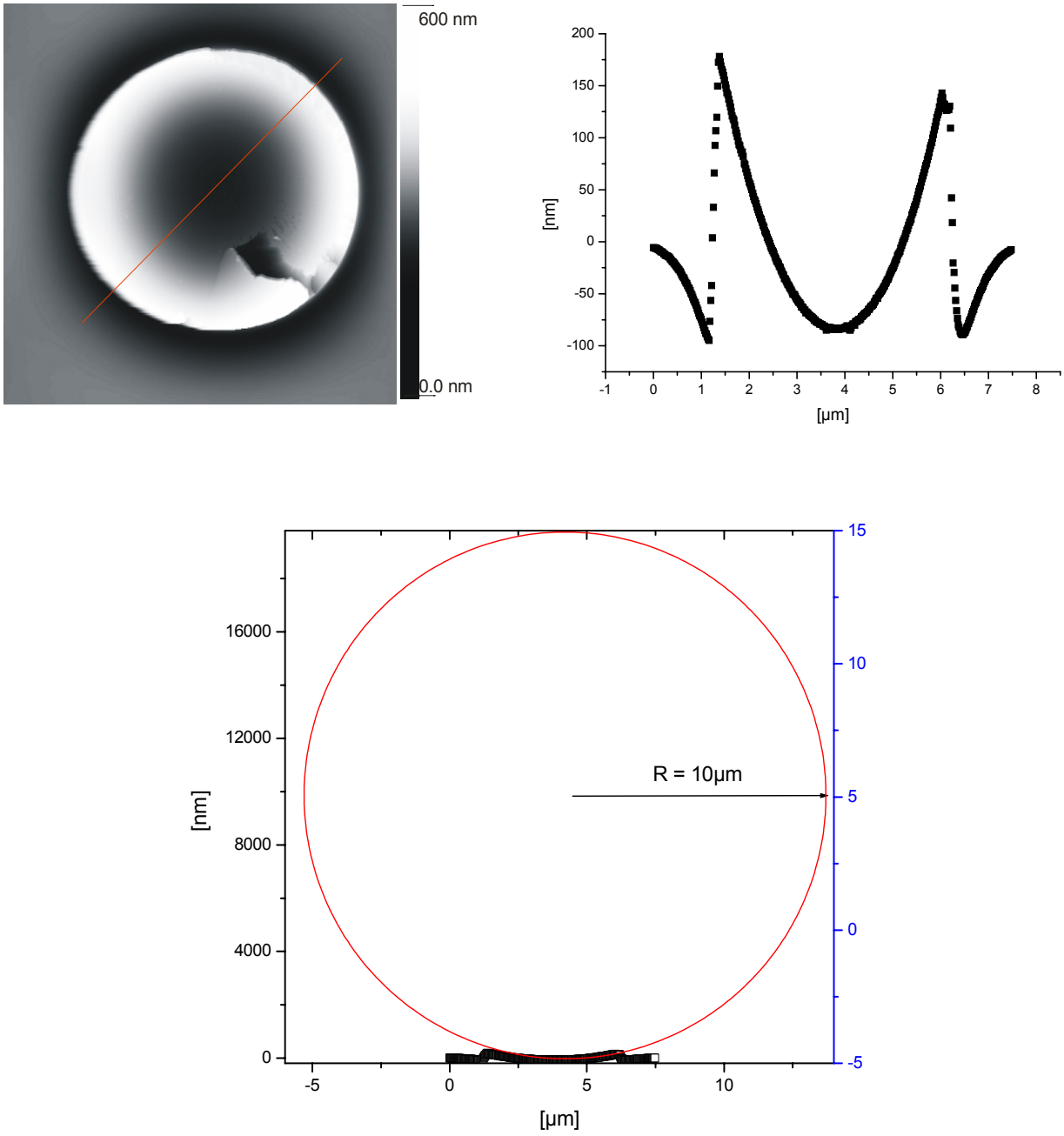

Fig. 6.7: Upper left: an AFM image of a meniscus created by a 20 µm particle, after 5 min annealing by 160^{0}C. Upper right: the cross-section of the depicted meniscus (red line in the left picture). Lower: Representation of the particle-surface meniscus contact on µm scale.

The second type was an asymmetric meniscus, with one "side" higher than the other, as shown in Fig. 6.8. In addition, the imprint exhibited additionally a plateau. The latter is a "flat" area in the center of the particle position on the surface with a diameter of approximately 2 μm. This is however not to be confused to a damaged rim due to particle removal but it is clearly due to an irregular inhomogeneous meniscus development. This could be attributed in e.g. film inhomogeneity. A complete penetration of the film by the particle in this case is excluded and the observed plateau is indeed a polymer surface. In case a mechanical destruction of the meniscus during the manual particle removement would take place, the meniscus rim would be obviously and clearly interrupted and broken, as demonstrated in Fig. 6.7.

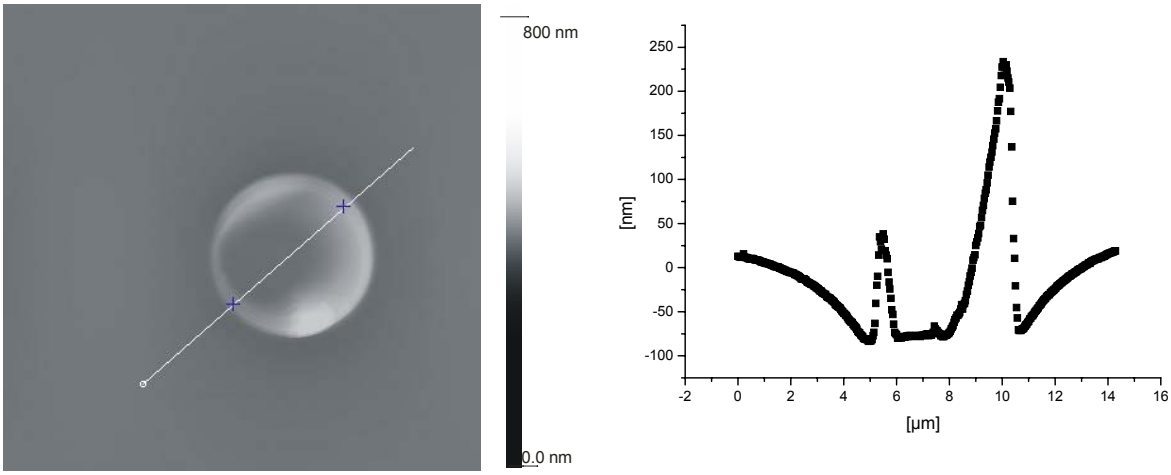

Fig. 6.8: Left: Asymmetric meniscus formed from a 10 μm particle on the surface after 15 min annealing by 160^0C. Right: Cross-section of the depicted meniscus (line with red-points in the left picture).

The third type of meniscus shape was a relatively symmetrical form including a smaller symmetrical meniscus in the centre, presented in Fig. 6.9, 6.10. In the middle of the meniscus the contact point between the particle and the PS film could be recognised and imaged, which resembles a very small plateau of 2 µm diameter. A smaller meniscus appears to be formed in the middle of the main meniscus.

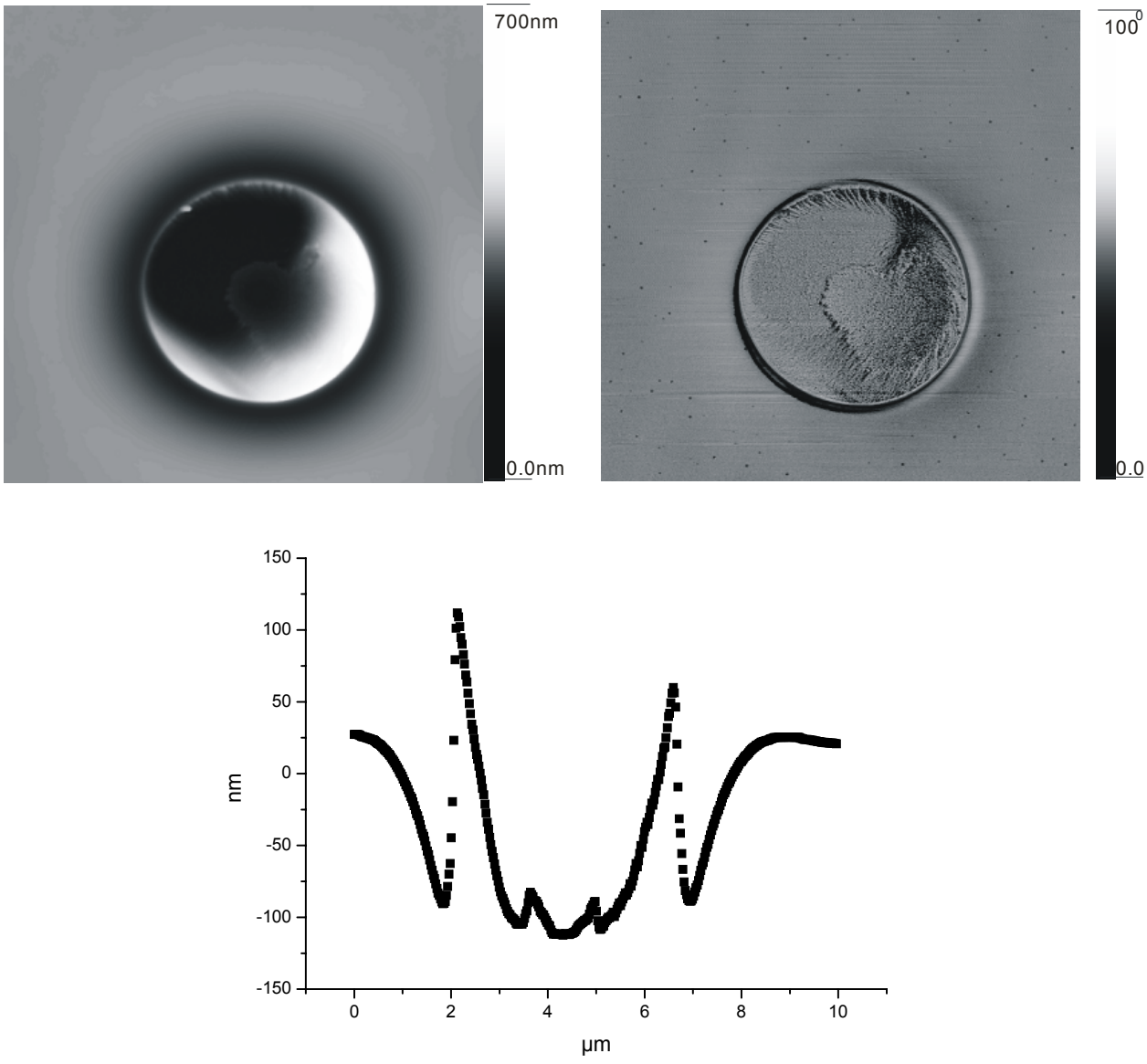

Fig. 6.9: Height (upper left) and phase (upper right) images of the meniscus formed by a 15 µm particle on the PS surface after 15 min annealing. The smaller homocentric meniscus is clearly depicted and regarded as the effective contact area. In the lower figure this is also clearly demonstrated in the plot of the cross-section and the approximately 1µm diameter secondary meniscus.

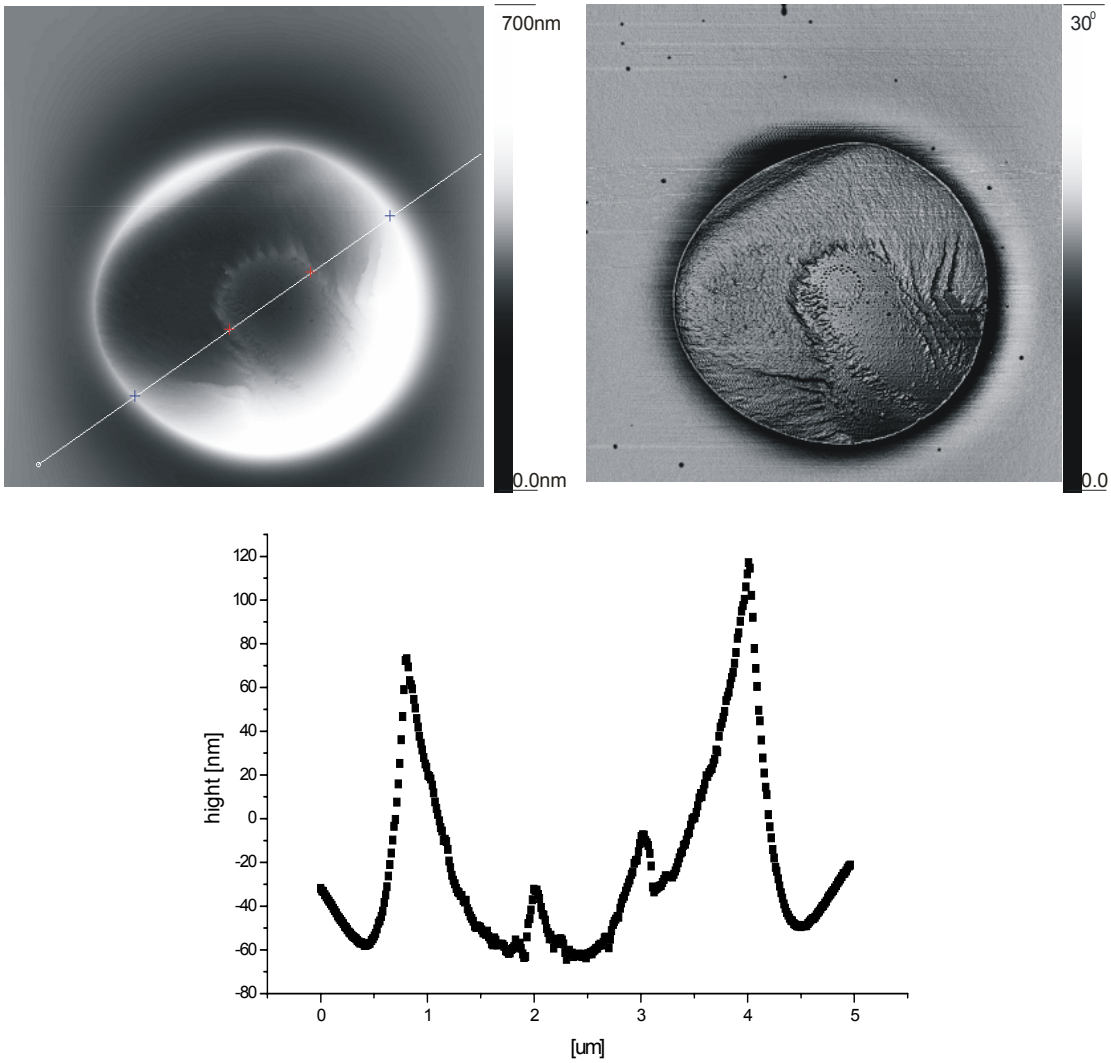

Fig. 6.10: Height (upper left) and phase (upper right) images of the meniscus formed from a 5 µm particle on the surface after 15 min annealing. The smaller homocentric meniscus is clearly depicted and regarded as the effective contact area. Scan size 5 µm. Below the cross-section with the secondary meniscus of approximately 1µm diameter depicted.

When zooming in on the centre of the meniscus spot, one could recognise that the particles were definitely in contact with a very thin polymer layer and did not yet touch the quartz electrode surface. This is demonstrated for the inner smaller meniscus of Fig. 6.10 which is shown in more detail in Fig. 6.11. This layer has a significantly higher roughness than the original polymer surface, which appears to be qualitatively similar to the roughness of the particle surface. Hence, it could be suggested that the observed surface of the secondary meniscus is a direct imprint of the particle.

The images in Fig. 6.9 and 6.10 can be explained in the following way: The effective particle-surface contact is the secondary meniscus of the small diameter of approx. 1µm diameter. The larger meniscus of a diameter 4-6 µm stabilizes the particle during oscillation and keeps it in position. This smaller meniscus would be the case of a weak particle-surface coupling, while for strong-coupling the particle would be expected to have a "full meniscus" contact area with the film.

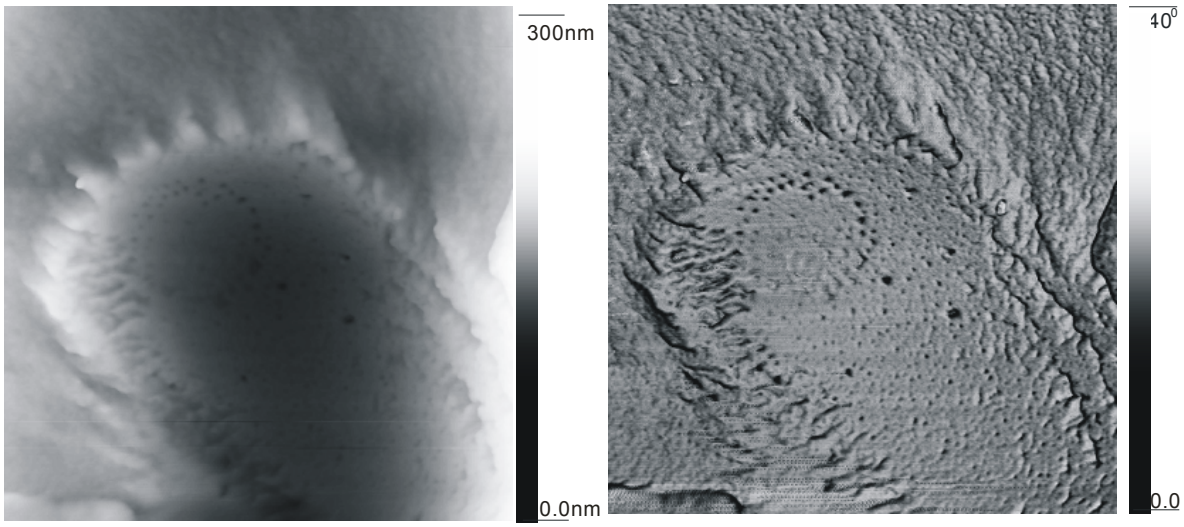

Fig. 6.11: Height (left) and phase (right) zoom in on the centre of Fig. 6.10: Secondary meniscus after annealing of 15 µm particle for 15 min, height and phase image, scan size 1.7 µm.

Additionally, the influence of annealing time on the meniscus formation was studied. From AFM images for samples after different annealing durations, it was determined that 2 min is adequate to fully form the structure. The structure remains unchanged under further annealing, specifically at typically 15 to 60 min. If however, the annealing takes place for over than ~100 min the film is degraded and "dissolves" close to the meniscus, in other words a dewetting of the film takes place, which is significantly affected and reduced in height. An example of this defect is shown in Fig. 6.12.

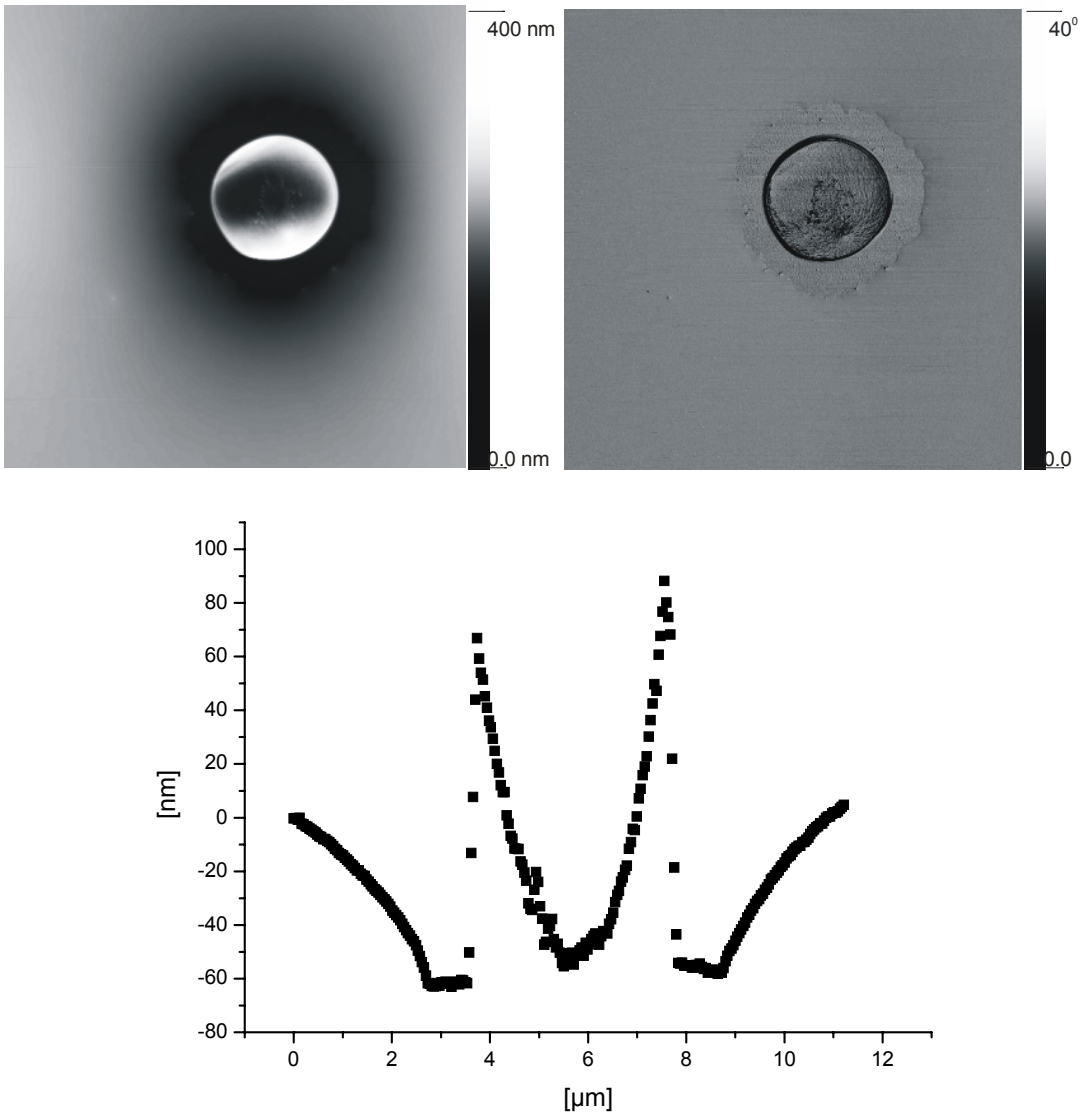

Fig. 6.12: Height (upper left) and phase (upper right) images of the meniscus formed from 20 µm particles after annealing for 120 min. The "dissolution" of the film close to the rim is obvious. Scan size 15 µm. Lower figure: the crossection with an approx. 1µm thick dewetted area of the film around the meniscus.

The AFM imaging helped in detecting three different meniscus types for the contact area between the particles and the polymer film surface, specifically after the QCM vibration and the system annealing. These types are the "full contact", the "asymmetrical" and the third including a "homocentric smaller meniscus". The observed frequency shifts are a result of the conformation of the distribution of different contacts and forces of varying intensity between particles and polymer surface. The particles show, as described above, a distribution of

coupling-constants rather than a single precise value, while the system can find itself in the strong- or in the weak-coupling regime.

All three meniscus types can be detected for all 4 particle sizes studied, even within the same sample. They appear after annealing and have reproducible dimensions, in agreement with the contact surface that is assumed for the specific particles on the polymer film. The different bonding intensity, to which the meniscus forms are attributed, could explain the deviation between number of particles per surface area measured by imaging and the values provided by the QCM via the frequency shift analysis. One assumption could be that, the asymmetric and the homocentric contact types are responsible for the positive frequency shifts observed for the 3 measured overtones, in other words for the weak-coupling regime in which the system appears to be. The particles with this binding intensity would change their position faster and would not necessarily follow the QCM movement. Thus, they would not effectively contribute to the mass increase of the quartz. The latter case is quantified by the negative frequency shift, $\Delta f < 0$ and can be the outcome of a "full contact" between particle and polymer film surface.

7. Summary and conclusions

The particle-surface contact is important for a wide range of industrial applications and governed by micromechanics. Within this work, a new methodology is developed for measuring adhesion forces, which utilizes the quartz crystal microbalance, QCM, and implements it for studying particle-polymer film interactions. The potential of this technique in measuring forces in this type of systems is evaluated by carrying out experiments with particles of different diameters, under different conditions. Furthermore, imaging and atomic force microscopy, AFM, is additionally utilized in order to validate the results and analyse how QCM experiments reflect the state of adhesion.

The quartz crystal microbalance is a very sensitive method developed to measure the mass per unit area of homogeneous thin films. Within this work, it is extended to study the contact between glass particles and a polymer, i.e. polystyrene, surface. The experimental setup consists of the QCM with the polymer film deposited onto the quartz surface. The imaging is performed by an optical microscope in order to get a combined monitoring of the phenomena taking place during the vibration. With this setup it is possible to monitor the particle motion under oscillation, while attached to the surface. The resonance frequency shift recorded is reproducible and used to quantify the stiffness of the polymer-particle contact. This interaction is found to be governed by the interplay between inertia and contact forces. The induced frequency shift is found to decrease or increase, depending on the type of particle-surface coupling and the amplitude and frequency overtone of the oscillation.

For a deeper understanding of the observed phenomena, four general models are taken into consideration, i.e. the Hertz, Johnson-Kendall-Roberts, Derjaguin-Müller-Toporov and the Mindlin theory of partial slip. The latter is utilized in order to qualitatively interpret the resulting frequency shifts and the estimated adhesion forces and particle velocities.

Considering the above theories and the resulting frequency shifts of the 3rd overtone in the QCM, one can describe the interaction between the particles and the surface. For strong coupling with the QCM surface, the particles appear to move with the vibrations and simply act as added effective mass. This leads to a decrease of the resonance frequency, in agreement with the Sauerbrey equation (calculation of added mass on QCM). However, when the system enters a regime of weak coupling between surface and particles, the latter are not able to follow the fast movement of the QCM surface. Hence, they effectively act as adding a

"spring" with an additional coupling constant and increase the resonance frequency. This positive frequency shift was consistently observed and was qualitatively reproducible.

When the QCM vibrations exceed specific critical amplitude, they may even lead to particle detachment. This critical amplitude was determined for the system using amplitude sweeps. During this set of experiments, three different behaviours were observed: no movement of particles at very low amplitudes, lateral motion at intermediate amplitudes and finally detachment, above the critical value. In experiments probing the particle – surface coupling, only amplitudes well below the critical one were applied in order to avoid frequency changes due to mass loss, as described by the Sauerbrey theory.

Furthermore, the higher overtones, specifically the 5^{th} and the 7^{th} were utilized in order to derive, if possible, additional information about the interactions taking place. In general, for small particles, i.e. < 15μm, the shift for specific overtones can increase after annealing. For large particle diameters annealing causes a negative frequency shift at all three higher overtones. For specific higher frequencies, one observes a break-down of the contact and even very strong and stable particle-surface coupling can be destroyed. The shifts at the lower overtones describe a generally strong-coupling regime for the system. For the highest overtone however, 7^{th}, a break-down of the contact was observed, indicated by positive frequency shifts for most of the studied particles.

The applicability of the QCM method for quantifying particle-surface interactions and directly measuring adhesion forces is investigated. In the analysis, one has to take into account that the particles show a distribution of coupling constants rather than a single, precisely defined value. When this distribution is convoluted with the model-predicted frequency shift Δf, three regimes can be distinguished: (1) For low mean coupling constants $\bar{k}$, the frequency increases with increasing $\bar{k}$ until it reaches a maximum. (2) After the maximum Δf decreases and turns negative to reach a minimum. (3) Further increasing $\bar{k}$ leads to a gradual increase of Δf until it has reached a value in which the mass increase dominates. It is found that, solely from standard QCM experiments, a quantitative determination of interaction forces of particles with surfaces does not seem to be possible. One reason is that the frequency shift is not a unique function of the coupling constant. Therefore, the value of adhesion force cannot be deduced from the frequency shift measured by the QCM system.

Finally, the AFM method is introduced and used as a complementary method for direct force measurements. AFM is further applied in order to study the surface of the polymer film after the system excitation and removement of the particles. The AFM imaging helped in

detecting three different meniscus types for the contact area between the particles and the polymer film surface, specifically after the QCM vibration and the system annealing. These types are the “full contact”, the “asymmetrical” and the third including a “homocentric smaller meniscus”. The observed frequency shifts are a result of the conformation of the distribution of different contacts and forces of varying intensity between particles and polymer surface. All three types of surface structures can be detected for all 4 particle sizes studied, even within the same sample under investigation. The different bonding intensity, to which the meniscus forms are attributed, could explain the deviation between number of particles per surface area measured by imaging and the values provided by the QCM via the frequency shift analysis. The asymmetric and the homocentric contact types are suggested to be responsible for the positive frequency shifts observed for the 3 measured overtones, in other words for the weak-coupling regime in which the system appears to be. The particles with this binding intensity would change their position faster and would not necessarily follow the QCM movement. Thus, they would not effectively contribute to the mass increase of the quartz. The latter case is quantified by the negative frequency shift, $\Delta f < 0$ and can be the outcome of a “full contact” between particle and polymer film-surface.

The AFM provides is utilized here to study the surface effects and more importantly to quantify the forces between particles and surface, while QCM gives qualitative information on the contact type and interaction intensity.

References

[1] J. N. Israelachvili, *Intermolecular and Surface Forces*, 2 ed. (Academic Press, London, 1992).

[2] M. A. Felicetti, G. R. Salazar-Banda, J. R. Coury, and M. L. Aguiar, Industrial & Engineering Chemistry Research **48,** 877-887 (2009).

[3] G. R. Salazar-Banda, M. A. Felicetti, J. A. S. Goncalves, J. R. Coury, and M. L. Aguiar, Powder Technology **173,** 107-117 (2007).

[4] R. Polke, Bull. Soc. Special Chim. France **A3241,** 51-54 (1969).

[5] R. Polke, Chemie Ingenieur Technik **40,** 1057-& (1968).

[6] S. W. Booth and J. M. Newton, Journal Of Pharmacy And Pharmacology **39,** 679-684 (1987).

[7] K. K. Lam and J. M. Newton, Powder Technology **65,** 167-175 (1991).

[8] K. K. Lam and J. M. Newton, Powder Technology **73,** 117-125 (1992).

[9] K. K. Lam and J. M. Newton, Powder Technology **76,** 149-154 (1993).

[10] S. H. Kim, D. B. Asay, and M. T. Dugger, Nano Today **2,** 22-29 (2007).

[11] G. Behme and T. Hesjedal, J. Appl. Phys. **89,** 4850-4856 (2001).

[12] T. Oiwa, Rev. Sci. Instru. **77,** 016107 (2006).

[13] A. Socoliuc, E. Gnecco, S. Maier, O. Pfeiffer, A. Baratoff, R. Bennewitz, and E. Meyer, Science **313,** 207-210 (2006).

[14] S. Herminghaus, Advances in Physics **54,** 221-261 (2005).

[15] J. Tomas, Chem. Eng. Sci. **62,** 1997-2010 (2007).

[16] H. Krupp, Adv. Colloid Interface Sci. **1,** 111-239 (1967).

[17] H. Schubert, H. Sommer, and H. Rumpf, Chem.-Ing.-Techol. **48,** 716 (1976).

[18] R. Polke, H. Krupp, and H. Rumpf, in *Chemie, physikalische Chemie und Anwendungstechnik der grenzflächenaktiven Stoffe*, edited by V. I. K. f. g. Stoffe (Carl Hanser Verlag, München, 1973).

[19] F. Podczeck, J. M. Newton, and M. B. James, Powder Technol. **83,** 201-209 (1995).

[20] L. Heim, S. Ecke, M. Preuss, and H.-J. Butt, J. Adh. Sci. Technol. **16,** 829-843 (2002).

[21] L. O. Heim, J. Blum, M. Preuss, and H.-J. Butt, Phys. Rev. Lett. **83,** 3328-3331 (1999).

[22] H. Rumpf, Chemie-Ing.-Techn. **46,** 1-11 (1974).

[23] T. C. Halsey and A. J. Levine, Phys. Rev. Lett. **80,** 3141-3145 (1998).

[24] M. Götzinger and W. Peukert, Langmuir **20,** 5298-5303 (2004).

[25] K. Cooper, A. Gupta, and S. Beaudoin, J. Colloid Interface Sci. **234,** 284-292 (2001).
[26] Y. I. Rabinovich, J. J. Adler, A. Ata, and B. M. Moudgil, J. Colloid Interface Sci. **232,** 17-24 (2000).
[27] M. Farshchi, M. Kappl, Y. Cheng, J. S. Gutmann, and H.-J. Butt, Langmuir **22,** 2171-2184 (2006).
[28] G. R. Salazar-Banda, M. A. Felicetti, J. A. S. Goncalves, J. R. Coury, and M. L. Aguiar, Powder Technol. **173,** 107-117 (2007).
[29] H.-J. Butt, B. Cappella, and M. Kappl, Surf. Sci. Rep. **59,** 1-152 (2005).
[30] G. L. Dybwad, J. Appl. Phys. **58,** 2789-2790 (1985).
[31] MtronPTI, www.mtronpti.com.
[32] V. E. Bottom, (1982).
[33] A. Pomorska, D. Shchukin, R. Hammond, M. A. Cooper, G. Grundmeier, and D. Johannsmann, Analytical Chemistry **82,** 2237-2242.
[34] D. Johannsmann, (2001).
[35] G. Sauerbrey, A.E.Ü. **18,** 617-624 (1964).
[36] D. Johannsmann and L. Heim, J. Appl. Phys. **100,** 094505 (2006).
[37] V. M. Mecea, Sensors And Actuators A-Physical **128,** 270-277 (2006).
[38] D. Johannsmann, in *Piezoelectric Sensors*, edited by J. A. Steinem C. (Springer, 2007), p. 49-109.
[39] D. A. Buttry and M. D. Ward, Chemical Reviews **92,** 1355-1379 (1992).
[40] A. Arnau, (2004).
[41] S. Berg, PhD thesis (2003).
[42] A. Sapper, Dissertation (2006).
[43] G. Sauerbrey, Z. Phys.**,** 206-210 (1959).
[44] D. Johannsmann, in *Piezoelectric Sensors*, edited by J. A. Steinem C. (Springer, 2007), p. 151-170.
[45] S. Berg, M. Ruths, and D. Johannsmann, Rev.Sci.Instrum. **74,** 3845-3852 (2003).
[46] D. Johannsmann, PhD thesis (1991).
[47] D. Johannsmann, Macromolecular Chemistry And Physics **200,** 501-516 (1999).
[48] K. K. Kanazawa, Faraday Discussions **107,** 77-90 (1997).
[49] K. K. Kanazawa and O. R. Melroy, Ibm Journal Of Research And Development **37,** 157-171 (1993).
[50] C. E. Reed, K. K. Kanazawa, and J. H. Kaufman, Journal Of Applied Physics **68,** 1993-2001 (1990).
[51] O. Wolff, PhD thesis (1998).
[52] O. Wolff, E. Seydel, and D. Johannsmann, Faraday Discussions **107,** 91-104 (1997).
[53] J. R. Vig and A. Ballato, Ieee Transactions On Ultrasonics Ferroelectrics And Frequency Control **45,** 1123-1124 (1998).
[54] H.-J. Butt and M. Kappl, (2010).
[55] B. Cappella and G. Dietler, Surface Science Reports **34,** 1-+ (1999).
[56] F. Podczeck, J. M. Newton, and M. B. James, J. Appl. Phys. **79,** 1458-1463 (1996).
[57] B. Bhushan, (2004).
[58] H.-J. Butt, K. Graf, and M. Kappl, *Physics and Chemistry of Interfaces* (Wiley-VCH, Berlin, 2003).
[59] P. M. Claesson, T. Ederth, V. Bergeron, and M. W. Rutland, Advances In Colloid And Interface Science **67,** 119-183 (1996).
[60] F. Podczeck and J. M. Newton, J. Pharm. Sci. **84,** 1067-1071 (1995).
[61] H. C. Hamaker, Physica **4,** 1058 (1937).
[62] G. Binnig, C. F. Quate, and C. Gerber, Phys. Rev. Lett. **56,** 930-933 (1986).
[63] C. T. Gibson, G. S. Watson, and S. Myhra, Nanotechnology **7,** 259-262 (1996).

[64] E. Meyer, H. Heinzelmann, P. Grütter, T. Jung, H. R. Hidber, H. Rudin, and H. J. Güntherodt, Thin Solid Films **181,** 527-544 (1989).
[65] A. L. Weisenhorn, P. K. Hansma, T. R. Albrecht, and C. F. Quate, Appl. Phys. Lett. **54,** 2651-2653 (1989).
[66] E. Meyer, Progress In Surface Science **41,** 3-49 (1992).
[67] W. A. Ducker, T. J. Senden, and R. M. Pashley, Nature **353,** 239-241 (1991).
[68] W. A. Ducker, T. J. Senden, and R. M. Pashley, Langmuir **8,** 1831-1836 (1992).
[69] H.-J. Butt, Biophys. J. **60,** 1438-1444 (1991).
[70] H. Mizes, M. Ott, E. Eklund, and D. Hays, Colloids Surfaces A **165,** 11-23 (2000).
[71] M. D. M. Peri and C. Cetinkaya, J. Adh. Sci. Technol. **22,** 507-528 (2008).
[72] R. G. Horn, J. N. Israelachvili, and F. Pribac, Journal Of Colloid And Interface Science **115,** 480-492 (1987).
[73] K. L. Johnson, K. Kendall, and A. D. Roberts, *Proc. R. Soc. Lond. A* **324,** 301-313 (1971).
[74] B. V. Derjaguin, V. M. Muller, and Y. P. Toporov, J. Colloid Interface Sci. **53,** 314-325 (1975).
[75] H. Hertz, J. Reine Angewandte Mathematik **92,** 156-171 (1882).
[76] D. Maugis, J. Colloid Interface Sci. **150,** 243-269 (1992).
[77] R. W. Carpick, D. F. Ogletree, and M. Salmeron, J. Colloid Interface Sci. **211,** 395-400 (1999).
[78] K. L. Johnson and J. A. Greenwood, Journal Of Colloid And Interface Science **192,** 326-333 (1997).
[79] B. Cappella and G. Dietler, Surf. Sci. Reports **34,** 1-104 (1999).
[80] A. Laschitsch and D. Johannsmann, J. Appl. Phys. **85,** 3759-3765 (1999).
[81] C. M. Flanigan, M. Desai, and K. R. Shull, Langmuir **16,** 9825-9829 (2000).
[82] J. A. Forrest, J. Mattsson, and L. Börjesson, Eur. Phys. J. E **8,** 129-136 (2002).
[83] Q. Zhang, R. M. Lec, and K. Pourrezaei, IEEE Trans. Ultrasonics, Ferroelectrics, and Frequency Control **53,** 167-174 (2006).
[84] J. N. D'Amour, J. J. R. Stalgren, K. K. Kanazawa, C. W. Frank, M. Rodahl, and D. Johannsmann, Phys. Rev. Lett. **96,** 058301 (2006).
[85] E. Vittorias, M. Kappl, H. J. Butt, and D. Johannsmann, Powder Technology **203,** 489-502.
[86] D. Johannsmann, in *Piezoeletric Sensors*, edited by A. Langhoff and C. Steinem (Springer, Heidelberg, 2006).
[87] S. J. Martin, H. L. Bandey, R. W. Cernosek, A. R. Hillman, and M. J. Brown, Anal. Chem. **72,** 141-149 (2000).
[88] F. Eggers and T. Funck, J. Physics E - Sci. Instru. **20,** 523-530 (1987).
[89] D. Johannsmann, K. Mathauer, G. Wegner, and W. Knoll, Phys. Rev. B **46,** 7808-7814 (1992).
[90] R. Lucklum, C. Behling, and P. Hauptmann, Anal. Chem. **71,** 2488-2496 (1999).
[91] D. Johannsmann, I. Reviakine, and R. R.P.**,** submitted (2009).
[92] B. Y. Du, A. M. Konig, and D. Johannsmann, New J. Physics **10,** 053014 (2008).
[93] S. Strogatz, *Nonlinear Dynamics and Chaos*, Vol. Chapter 7.6 (Addison-Wesley, 1996).
[94] S. Berg, T. Prellberg, and D. Johannsmann, Rev. Sci. Instrum. **74,** 118-126 (2003).
[95] A. D. Polyanin and A. V. Manzhirov, *Handbook of Integral Equations* (CRC Press, Boca Raton, 1998).
[96] F. J. Giessibl, Appl. Phys. Lett. **78,** 123-125 (2001).
[97] H. Hölscher, W. Allers, U. D. Schwarz, A. Schwarz, and R. Wiesendanger, Phys. Rev. Lett. **83,** 4780-4783 (1999).
[98] J. E. Sader and S. P. Jarvis, Appl. Phys. Lett. **84,** 1801-1803 (2004).

[99] K. L. Johnson, *Contact Mechanics* (Cambridge University Press, Cambridge, 1985).
[100] R. D. Mindlin and H. Deresiewicz, J. Appl. Mech., Trans. ASME **20,** 327-344 (1953).
[101] D. Johannsmann, Phys. Chem. Chem. Phys. **10,** 4516-4534 (2008).
[102] P. Berthoud and T. Baumberger, Proc. Roy. Soc. London A **454,** 1615-1634 (1998).
[103] L. Bureau, C. Caroli, and T. Baumberger, Proc. Roy. Soc. London A **459,** 2787-2805 (2003).
[104] E. Arzt, S. Gorb, and R. Spolenak, Proc. Natl. Acad. Sci. USA **100,** 10603-10606 (2003).
[105] B. N. J. Persson, Euro. Phys. J. E **8,** 385-401 (2002).
[106] C. W. Extrand, Polymer Engineering And Science **34,** 390-394 (1994).
[107] W. J. Daughton and F. L. Givens, Journal Of The Electrochemical Society **129,** 173-179 (1982).
[108] O. Wolff and D. Johannsmann, J. Appl. Phys. **87,** 4182-4188 (2000).
[109] S. Rudenkiy, Thesis, University of Technology, 2007.
[110] S. H. Kim, D. B. Asay, and M. T. Dugger, Nano Today **2,** 22-29 (2007).
[111] M. Janssen, J. Zuidema, and R. J. H. Wanhill, *Fracture Mechanics* (Chapman & Hall, 2004).
[112] A. Laschitsch, PhD thesis (1999).
[113] M. Kappl and H.-J. Butt, Part. Part. Syst. Charact. **19,** 129-143 (2002).
[114] A. Torii, M. Sasaki, K. Hane, and O. Shigeru, Meas. Sci. Technol. **7,** 179-184 (1996).
[115] J. L. Hutter and J. Bechhoefer, Rev. Sci. Instrum. **64,** 1868-1873 (1993).
[116] M. Götzinger and W. Peukert, Powder Technol. **130,** 102-109 (2003).

Acknowledgements